# SOLVING THE INVERSE PROBLEM OF ELECTROCARDIOGRAPHY FOR SPONTANEOUS PVC LOCALIZATION: ANALYSIS OF CLINICAL ELECTROCARDIOGRAPHIC DATA

A THESIS SUBMITTED TO
THE GRADUATE SCHOOL OF APPLIED MATHEMATICS
OF
MIDDLE EAST TECHNICAL UNIVERSITY

BY

NIKA RASOOLZADEH

IN PARTIAL FULFILLMENT OF THE REQUIREMENTS
FOR
THE DEGREE OF MASTER OF SCIENCE
IN
SCIENTIFIC COMPUTING

JANUARY 2023

Approval of the thesis:

**SOLVING THE INVERSE PROBLEM OF ELECTROCARDIOGRAPHY FOR SPONTANEOUS PVC LOCALIZATION: ANALYSIS OF CLINICAL ELECTROCARDIOGRAPHIC DATA**

submitted by **NIKA RASOOLZADEH** in partial fulfillment of the requirements for the degree of **Master of Science in Scientific Computing Department, Middle East Technical University** by,

Prof. Dr. A. Sevtap Selçuk Kestel _____
Dean, Graduate School of **Applied Mathematics**

Assoc. Prof. Dr. Önder Türk _____
Head of Department, **Scientific Computing**

Assoc. Prof. Dr. Yeşim Serinağaoğlu Doğrusöz _____
Supervisor, **Electrical and Electronics Engineering, METU**

**Examining Committee Members:**

Prof. Dr. Osman Eroğul
Biomedical Engineering, TOBB ETU _____

Assoc. Prof. Dr. Yeşim Serinağaoğlu Doğrusöz
Electrical and Electronics Engineering, METU _____

Assoc. Prof. Dr. Hamdullah Yücel
Scientific Computing, METU _____

**Date:** _____

**I hereby declare that all information in this document has been obtained and presented in accordance with academic rules and ethical conduct. I also declare that, as required by these rules and conduct, I have fully cited and referenced all material and results that are not original to this work.**

Name, Last Name: NIKA RASOOLZADEH

Signature :

# ABSTRACT

SOLVING THE INVERSE PROBLEM OF ELECTROCARDIOGRAPHY FOR SPONTANEOUS PVC LOCALIZATION: ANALYSIS OF CLINICAL ELECTROCARDIOGRAPHIC DATA

Rasoolzadeh, Nika
M.S., Department of Scientific Computing
Supervisor : Assoc. Prof. Dr. Yeşim Serinağaoğlu Doğrusöz

January 2023, 95 pages

The inverse problem of electrocardiography refers to the determination of the electrical activity of the heart from the body surface potential measurements (BSPM). Knowledge of this electrical activity can provide valuable insights for the diagnosis of cardiac disorders and aid in the facilitation of the development of appropriate treatments. Consequently, efficient resolution of this problem has the potential to be of significant benefit to clinical practices, making it imperative to continue the research in this field.

This problem is considered ill-posed due to the presence of attenuation and spatial averaging effects within the thorax between the cardiac sources and the body surface. This characteristic can result in highly inaccurate or oscillatory solutions, particularly in the presence of measurement noise or an imprecise mathematical model. Despite significant efforts to address the challenges and limitations, an optimal method for the analysis of clinical data in this problem has yet to be developed.

A relatively limited number of studies have been conducted on the application of the inverse problem of electrocardiography for the localization of spontaneous Premature Ventricular Contraction (PVC). PVC refers to an abnormal cardiac contraction that originates from one of the ventricles.

This study focuses on using the Tikhonov regularization method for the reconstruction of unknown heart potentials with respect to various torso volume and cardiac source models derived from BSPMs of patients who have been indicated for ablation. By estimating Activation Time (AT) sequences, the PVC origin locations are explored for a number of patients. The findings indicate that the implementation of the proposed methods could provide physicians with more accurate localization of spontaneous PVCs.

Keywords: Inverse Electrocardiography, Electrocardiographic Imaging,Tikhonov Regularization, Activation Time, Spontaneous PVC Localization

# ÖZ

ELEKTROKARDİYOGRAFİNİN TERS PROBLEMİNİ SPONTAN VENTRİKÜLER ERKEN VURU KONUMLANDIRILMASINDA ÇÖZMEK: KLİNİK ELEKTROKARDİYOGRAFİK VERİLERİN ANALİZİ

Rasoolzadeh, Nika
Yüksek Lisans, Bilimsel Hesaplama Bölümü
Tez Yöneticisi : Doç. Dr. Yeşim Serinağaoğlu Doğrusöz

Ocak 2023, 95 sayfa

Elektrokardiyografinin ters problemi, vücut yüzey potansiyel ölçümlerinden kalbin elektrik aktivitesinin tahmin edilmesini ifade eder. Kalbin elektrik aktivite durumunun bilinmesi, kalp bozukluklarının tanısı için değerli bilgiler sağlar ve uygun tedavilerin geliştirilmesine yardımcı olur. Bu nedenle, bu problemin etkili bir şekilde çözülmesi klinik uygulamalar için büyük fayda sağlayabilir ve bu nedenle bu alanda araştırmaların sürdürülmesi önemlidir.

Bu problem, gövde içinde kalp kaynakları ve vücut yüzey arasındaki azaltma ve mekansal ortalama etkilerinden dolayı sağlam bir çözüm bulunmasının zorluğu nedeniyle kötü konumlandırılmış olarak kabul edilir. Bu özellik, özellikle ölçüm gürültüsü veya hatalı matematiksel modelin varlığında yüksek oranda yanlış veya osilatif çözümler oluşmasına neden olabilir. Bu zorluklar ve sınırlamaların aşılması için önemli çabalar harcandığı halde, klinik verilerin bu problem için analizi için optimal bir yöntem henüz geliştirilmemiştir.

Spontan Ventriküler Erken Vuru (VEV) lokalizasyonu için elektrokardiyografinin ters problemi uygulamasına ilişkin az sayıda çalışma gerçekleştirilmiştir. VEV, ventriküllerden biriyle başlayan anormal kalp kasılmalarını ifade eder.

Bu çalışma, vücut yüzey potansiyel ölçümlerinden türetilen farklı toraks hacmi ve kalp kaynakı modellerine göre bilinmeyen kalp potansiyellerinin yeniden inşası için Tikhonov düzenleme yöntemini kullanmayı odaklamaktadır. Aktivasyon Zamanı (AZ) dizilerini tahmin ederek, birçok hasta için VEV kaynak lokasyonları araştırılmaktadır. Bulgular, önerilen yöntemlerin uygulanmasının, hekimlere spontan VEVlerin daha doğru lokalizasyonunu sağlayabileceğini göstermektedir.

Anahtar Kelimeler: Tersine Elektrokardiyografi, Elektrokardiyografik Görüntüleme, Tikhonov Normalleştirme, Aktivasyon Zamanı, Ventriküler Erken Vuru Lokalizasyonu

*to my dear father*

# ACKNOWLEDGMENTS

I would like to extend my sincerest gratitude to a number of individuals who have played a crucial role in my journey. Firstly, I am deeply grateful to my supervisor, Assoc. Prof. Yeşim Serinağaoğlu Dogrusöz, for her unwavering support, guidance, and her invaluable contributions to my growth as a professional. I am honored to have had the opportunity to learn from such a brilliant individual. My eternal gratitude goes to her for her constant encouragement, support, and knowledge, without which this endeavor would not have been possible.

My sincere thanks also goes to Dr. Jana Švehlíková and Dr. Beáta Ondrušová from the Institute of Measurement Science at the Slovak Academy of Sciences, for their immense support and contributions.

I would like to thank my friends at METU Heart Research Laboratory Kutay Uğurlu and Furkan Aldemir for their encouragement and contributions all the way through.

Lastly, my eternal gratitude also goes to my parents and dear sister, whose love and support have been a constant source of strength throughout my journey. I am honored to dedicate this study to my dear father. He will always be remembered and his memory will always be in my heart. It is in recognition of his love and for being the best father anyone could ask for, that I dedicate this study to him, may it serve as a testament to his enduring legacy.

This work was supported by TUBITAK (grant no: 120N200).

# TABLE OF CONTENTS

# LIST OF TABLES

# LIST OF FIGURES

# LIST OF ABBREVIATIONS

| | |
|---|---|
| AP | Action Potential |
| AV | Atrioventricular |
| BEM | Boundary Element Method |
| BSP | Body Surface Potential |
| BSPM | Body Surface Potential Measurement |
| CAD | Coronary Artery Diseases |
| CT | Computed Tomography |
| CVD | Cardiovascular Disease |
| ECG | Electrocardiogram |
| ECGI | Electrocardiographic Imaging |
| EGM | Electrogram |
| Epi | Epicardium |
| EpiEndo | Epicardium Endocardium |
| FDM | Finite Difference Method |
| FEM | Finite Element Method |
| GMRES | Generalized Minimal Residual |
| IQR | Interquartile Range |
| PVC | Premature Ventricular Contraction |
| LAT | Local Activation Time |
| LE | Localization Error |
| MINRES | Minimum Residual |
| MRI | Magnetic Resonance Imaging |
| OTVAs | Outflow Tract Ventricular Arrhythmias |
| RVOT | Right Ventricular Outflow Tract |
| SA | Sinoatrial |
| SVD | Singular Value Decomposition |
| TSVD | Truncated Singular Value Decomposition |
| WHO | World Health Organization |

# CHAPTER 1

# INTRODUCTION

Cardiovascular Diseases (CVDs) are among the most common reasons for (sudden) death worldwide. As per the estimations of the World Health Organization (WHO), CVDs result in the deaths of approximately 17.9 million individuals annually, which corresponds to 32% of all deaths globally. A majority of CVDs can be prevented by addressing behavioral risk factors such as tobacco use, unhealthy diet and obesity, physical inactivity, and excessive consumption of alcohol. It is crucial to identify CVDs at an early stage, so that management through counseling and medication can be initiated [66]. In fact, it has been proposed that as much as 90% of CVD cases may be avoided through preventative measures [39, 43].

As technology continues to advance within the medical field, the capability to non-invasively view the heart and its associated blood vessels has also improved. A number of imaging modalities in use to this day include echocardiography, myocardial perfusion imaging through nuclear scintigraphy, magnetic resonance imaging (MRI), and computed tomography (CT), which can be utilized separately or together, depending on the specific diagnostic requirements [50].

Premature Ventricular Contraction (PVC) is a type of arrhythmia in which the heartbeat is initiated by the Purkinje fibers in the ventricles instead of the sinoatrial (SA) node [16]. These contractions result in an irregular heartbeat and may be accompanied by a fluttering or skipped beat sensation in the chest. PVCs are considered benign as long as they occur infrequently. However, if they become very frequent, they may indicate a pathological condition such as cardiac muscle failure. Spontaneous PVC is a naturally occurring phenomenon whereas pacemaker PVC responses

are generated by an algorithm that is dependent on the pacemaker device being used.

PVCs can have non-cardiac underlying causes such as smoking, stress, increased adrenaline due to exercise, alcohol or drug misuse, and cardiac causes like congenital heart disease, coronary artery diseases (CAD), heart failure, and a weakened heart muscle (cardiomyopathy) [38].

A healthcare professional typically uses a stethoscope to listen to the heart in order to diagnose PVCs. Several procedures are available to confirm the diagnosis, namely a 12-lead electrocardiogram (ECG), a Holter monitor which is a portable ECG device for recording the heart's activity during a day or two, an event monitor that is another portable ECG device worn for several days until arrhythmia occurs, cardiac tests to reproduce the arrhythmia due to exercise [1, 38].

Treatments suggested for PVCs vary depending on the symptoms and underlying cause. Lifestyle changes, medications, and Radiofrequency Ablation (RFA) therapy are among the treatment methods. Catheter ablation is a procedure used to eliminate a malfunctioning electrical pathway from specific regions of the heart by burning them with a current induced by radio waves, in individuals who are at risk of developing cardiac arrhythmias.

Recently, noninvasive electrocardiographic imaging (ECGI) has been utilized for the localization of ventricular contractions in clinical research [18, 65, 30]. Given that the location of ablation can be inferred from cardiac activation maps, ECGI has the potential to provide valuable insights for guiding catheter ablation procedures.

## 1.1 Motivation and Scope of the Thesis

In this study, ECGI techniques are employed to address the inverse problem of electrocardiography with respect to different cardiac source models and the level of complexity assumed in the forward model for spontaneous PVC localization. A relatively limited number of studies have been conducted on the application of the inverse problem of electrocardiography specifically to this case.

Cardiac abnormality source localization is possible with activation time-based meth-

ods. However, a major limitation of using activation time as the basis for source configuration in the forward problem of electrocardiography is that it leads to a nonlinear problem, making the calculations highly complex and challenging to solve. In this study, we use heart potentials as the equivalent cardiac source model, and estimate the activation times from these potentials. We aim to enhance PVC origin detection by implementing and evaluating different cardiac and torso volume models for spontaneous PVCs. Obtaining promising results can be of advantage to physicians for better facilitation of the planning and execution of ablation therapies.

## 1.2 Contribution of the Thesis

This study includes a thorough evaluation of PVC origin estimation for five different torso models (homogeneous/inhomogeneous) and two different heart surface representations (epicardial only, and combined epicardial-endocardial). The resulting potential reconstructions are then utilized to estimate the activation times, and spontaneous PVC origins are localized as the earliest activated site on the heart surface. A spatiotemporal activation time method successfully regularizes minimum derivative-based solutions, consequently resulting in more robust PVC origin estimation.

These methods have been evaluated previously using animal and human data with artificially paced hearts. This study contributes to the literature by presenting in-depth evaluations of the localization of naturally occurring (spontaneous) PVCs in clinical (human) data.

This work has resulted in the following publication and presentation:

- Rasoolzadeh, N., Svehlikova, J., Ondrusova, B. and Serinagaoglu Dogrusoz, Y., *Variability of Premature Ventricular Contraction Localization with respect to Source and Forward Model Variation in Clinical Data* , Computing in Cardiology, Tampere, Finland, Sep.4-7, 2022.

## 1.3 Organization of the Thesis

First, a brief background is given for heart anatomy, cardiac electrophysiology, and forward and inverse problems of electrocardiography in chapter 2. Subsequently, the clinical data in hand is introduced along with the problem definition in chapter 3. Next, the proposed methods for heart potential reconstruction and PVC localization are discussed in the same chapter. Finally, the obtained outcomes are presented with their evaluations based on the evaluation criteria defined in chapter 4. Lastly, A number of further improvements and research topics are suggested in chapter 5.

# CHAPTER 2

# BACKGROUND

In this chapter, a brief background is given on heart anatomy, cardiac electrophysiology, forward and inverse problems of electrocardiography, and information about the datasets used in this study.

## 2.1 Heart Anatomy

The heart is a muscular organ located within the central portion of the chest between the lungs in charge of pumping blood to the body. The blood delivers oxygen and nutrients to the body and carries away metabolic wastes, such as carbon dioxide to be eliminated from the body through the lungs [21]. An adult heart weighs about 250-350 grams with a shape that often resembles a fist with dimensions of approximately 12 cm in length, 8 cm in width, and 6 cm in thickness. However, athletes may have larger hearts, for exercise causes the heart muscle to adapt and become stronger, similar to the way it affects skeletal muscles in the body [8]. There are four layers in the heart wall: the pericardium, the epicardium, the myocardium, and the endocardium as shown in Fig. 2.1.

- The heart is enclosed in a double-membrane sac called the pericardium, which also contains a small amount of fluid that helps the heart move smoothly during contraction and relaxation [8]. This layer protects the heart from infection and keeps its position within the chest stable [60].

- Epicardium is the layer under the pericardium in touch with the heart surface.

During the ventricular contraction, the electrical activity spreads across the heart in a wave-like manner from the endocardium to the epicardium. Both pericardium and epicardium are responsible for lubricating the heart and preventing friction during contraction and relaxation.

- Myocardium or the middle layer of the heart is the cardiac muscle responsible for heart contraction. It has different characteristics from the other two main types of muscle, skeletal and smooth muscles. The cyclical activity of contraction and relaxation are the two main features of the cardiac muscle through which it maintains stable blood pressure despite large variations in the blood flow. Skeletal myocytes (muscle) are made up of individual cells that are separately controlled by nerves, while cardiac myocytes are electrically connected and work together as a single unit called a cardiac syncytium [13].

- The inner lining of the heart is called the endocardium. It consists of connective tissues and protects the valves and heart chambers.

Human and mammal hearts have four chambers: left and right atria at the top, and left and right ventricles at the bottom as shown in Fig. 2.2. The heart pumps blood in a rhythmic pattern that is controlled by a group of pacemaker cells. These cells, which are located in the SA node, produce an electrical current that causes the heart muscle to contract. This current travels through the atrioventricular (AV) node and along the heart's conduction system, which is a network of specialized cells and tissues that help coordinate and regulate the heart's contractions. The current flow can be seen in Fig. 2.2.

The right atrium and ventricle are commonly referred to as the right heart, while the left atrium and ventricle are referred to as the left heart. There are two blood circulation circuits: pulmonary and systemic. In the first circuit, the right heart receives oxygen-depleted blood from the rest of the body and pumps it to the lungs to be oxygenated. Then, in the systematic circuit, the left heart receives oxygen-rich blood from the lungs and pumps it to the rest of the body as shown in Fig. 2.3. In both circuits, the atria receive blood as it enters the heart, while the ventricles, which have thicker walls, pump blood out of the heart [14].

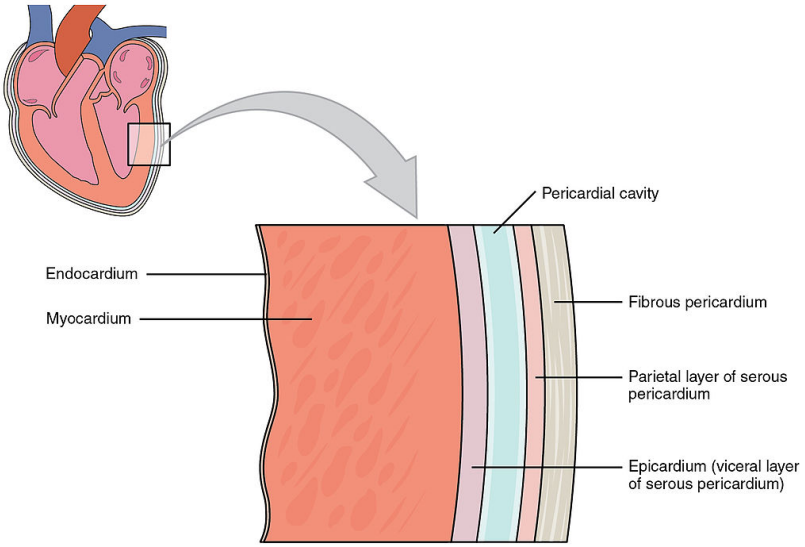

Figure 2.1: Heart wall layers [8]

The four heart valves that regulate the blood flow through the heart are the mitral, tricuspid, pulmonary, and aortic valves. Each valve acts as a gate to the heart chambers. The blood flow direction through each of them is also evident in Fig. 2.2. If the valves do not open and close correctly, the blood flow through pulmonary and systemic circulations gets disrupted.

## 2.2 Cardiac Electrophysiology

Cardiac cells are excitable cells that can generate electrical signals in response to a proper stimulus, or on their own like SA node pacemaker cells, by changing their membrane permeability to certain ions. The ionic concentration difference between the inner and outer sides of every cell membrane causes a potential difference across it. When a cardiac cell is excited, there is a rapid change in the electrical potential difference across its cell membrane, known as the transmembrane potential defined as:

$$V_m = V_i - V_e, \tag{2.1}$$

where $V_i$ and $V_e$ are the intracellular and extracellular potentials, respectively. If the stimulus is insufficient to reach the threshold value, the transmembrane potential will quickly return to its resting state once the stimulus ends. However, if the stimulus is above the threshold, the cell membrane will depolarize and the transmembrane

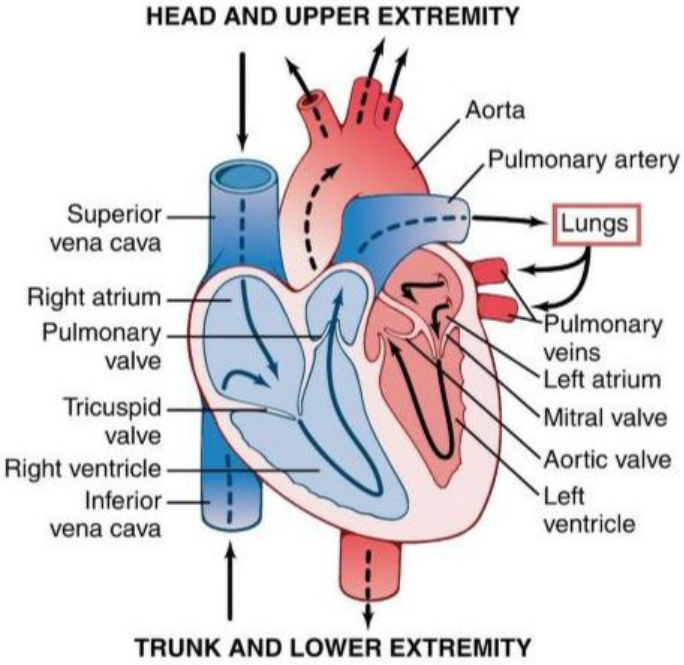


Figure 2.2: Heart anatomy diagram with blood flow through chambers and valves [21]

potential will increase from its negative resting value to a value near or above zero. It will remain at this value for a certain period of time before returning to the resting value as the membrane repolarizes. This event is known as an Action Potential (AP) [13].

There are five phases of AP as illustrated in Fig. 2.4. It represents various stages of activation and deactivation of different ion channel types, which leads to ionic currents and membrane potentials [64]:

- Phase 4 or Resting Phase: It is when the membrane potential is at the resting state without any electrical stimulation.
- Phase 0 or Depolarization Phase: It is the rapid rise of AP dependent on a fast $Na^+$ current $(I_{Na})$. This current is classified as fast due to its extremely rapid activation and deactivation kinetics when compared to other currents. As a result, in the majority of activations, the channel remains open for a duration of less than 1 ms.
- Phase 1 or Early Repolarization Phase: It is $Na^+$ channel inactivation and an

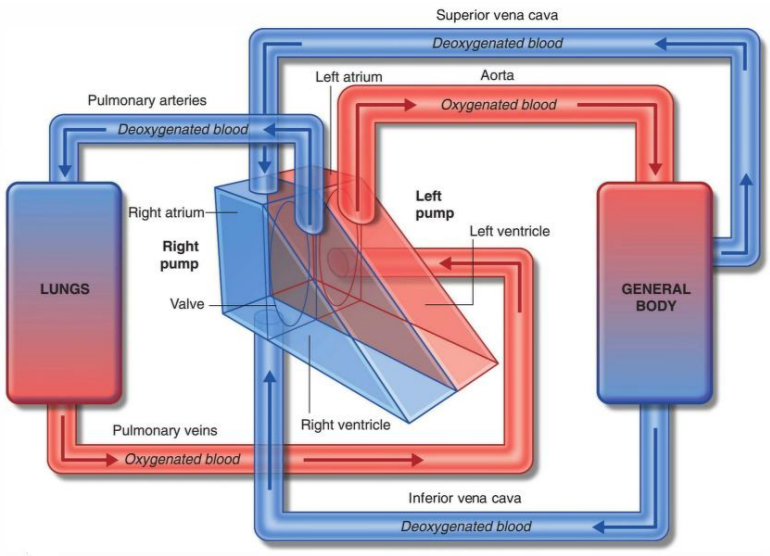

Figure 2.3: Heart pump diagram [14]

increase in the outward current of potassium ions ($K^+$), leading to a small, transient depolarization.

- Phase 2 or Plateau Phase: The membrane potential in this phase remains relatively constant. The plateau is caused by the influx of calcium ions $Ca^{2+}$ and the outflow of potassium ions $K^+$.
- Phase 3 or Repolarization Phase: It is the decrease in inward $I_{Ca}$ due to the inactivation of $Ca^{2+}$ channels and the increase in the outward $K^+$ currents ($I_K$) leading the cell back to its resting state.

The conduction system of the heart, shown in Fig. 2.5, which regulates the rhythm and pace of heartbeats, comprises the following components [11]:

- SA node: It is responsible for initiating the electrical signals that trigger the contraction of the heart.
- AV node: It is responsible for conducting electrical signals from the upper chambers of the heart, the atria, to the lower chambers, the ventricles.
- Left bundle branch: It transmits electrical impulses to the left ventricle.
- Right bundle branch: It transmits electrical impulses to the right ventricle.
- Bundle of His: It sends impulses from the AV node to the Purkinje fibers.

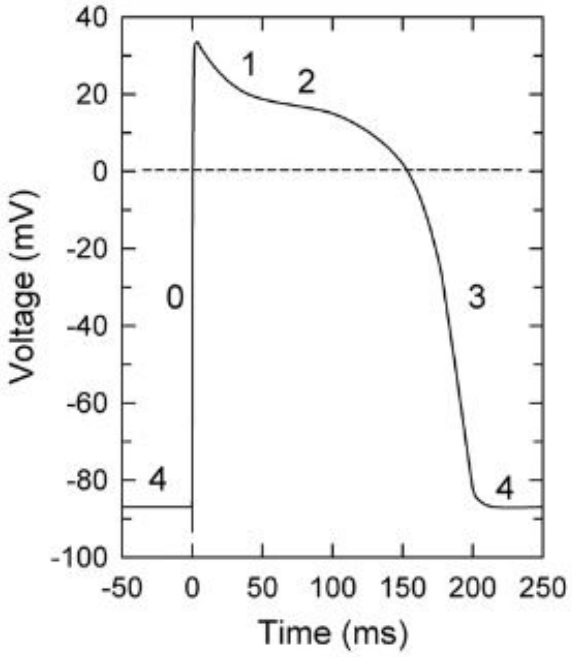


Figure 2.4: Ventricular action potential with the five phases labeled (0-4) [64]

- Purkinje fibers: They are responsible for triggering the contraction of the ventricles, which results in the pumping of blood to the entire body.

Following the initiation of electrical activation in the heart at the sinus node, it propagates through the atrial walls. Once depolarization has traveled through the atrial walls, it eventually reaches the AV node. The propagation through the AV node is delayed, during which the ventricular filling is completed. The activation continues to propagate along the Purkinje fibers until it reaches the inner walls of the ventricles [37]. This electrical activity can be measured on the body surface by using electrodes. The electrodes are positioned such that they accurately represent the spatiotemporal changes occurring in the cardiac electrical field. By using the voltage differences between the electrodes an ECG recording can be obtained. The recording in Fig. 2.6 shows a signal for the electrical activity propagation originated from the SA node and is called a normal sinus rhythm [58].

A normal ECG signal consists of several wave intervals as illustrated in Fig. 2.7, which correspond to a particular segment of the cardiac cycle. The P wave represents the sequential activation (depolarization) of the right and left atria. QRS complex shows the depolarization of the ventricles which normally occurs simultaneously,

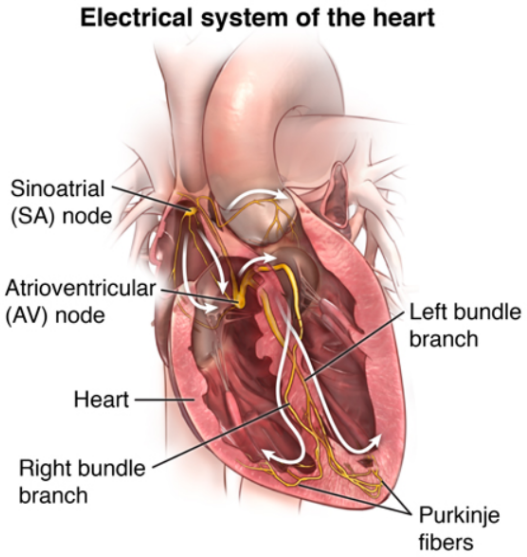


Figure 2.5: Schematic of the electrical conduction system of the heart [31]

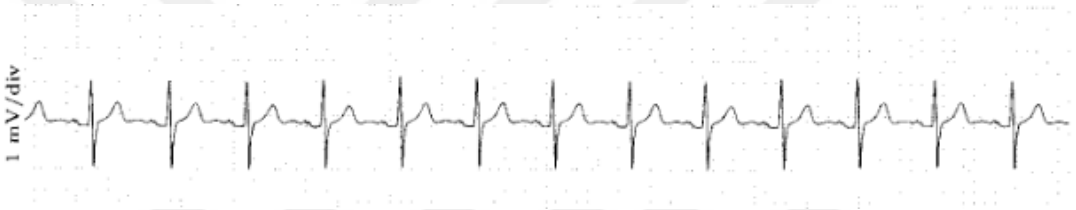


Figure 2.6: Normal sinus rhythm [58]

while the T wave shows ventricular repolarization. The PR interval is the time interval from the onset of atrial depolarization to the onset of ventricular depolarization. QT interval corresponds to the duration of ventricular depolarization and repolarization [68].

PVCs occur when an action potential in the ventricular muscle is generated prematurely, without being stimulated by the normal conductive mechanism of the heart, resulting in an early contraction of the ventricles [58]. Distinguishing PVCs from normal heartbeats is possible by monitoring the electrical activity of the heart through an ECG. An example recording for a single impulse activation from the right ventricle can be observed in Fig. 2.8. It depicts the multiplication of the time interval between R peaks when PVC occurs.

PVCs with benign characteristics and no underlying cardiac pathology do not require treatment, particularly if the individual experiences limited symptoms [1]. For patients who experience severe symptoms and have not responded to medical manage-

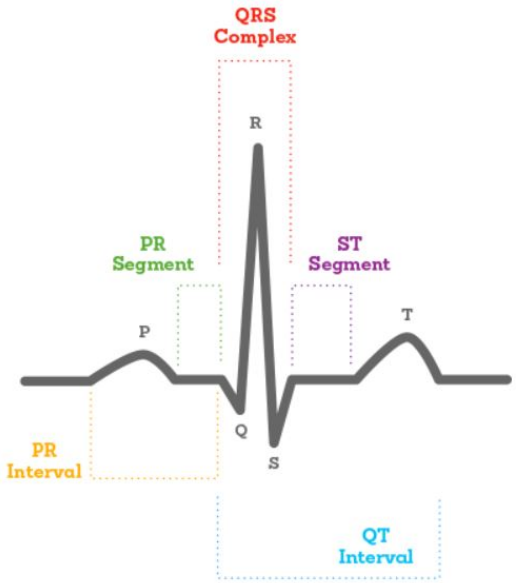


Figure 2.7: Normal ECG [2]

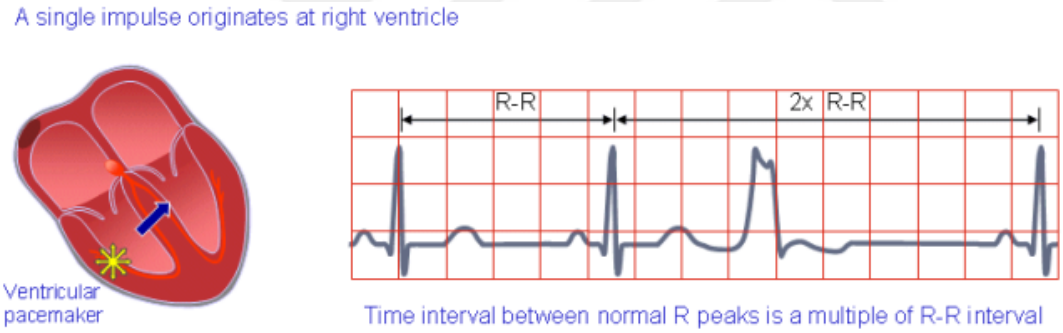


Figure 2.8: Premature ventricular contraction ECG [37]

ment, that is medications, lifestyle changes, and other non-invasive therapies, radio frequency catheter ablation (RFA) as a treatment option may be appropriate.

Accurate identification of PVC origin location is crucial for the success of ablation therapy. ECG analysis techniques are efficient in identifying abnormal cardiac behavior, however, they provide limited insight into the specific spatial properties of these abnormalities [12]. This is where techniques such as ECGI can be utilized to provide valuable information.

## 2.3 Standard 12-Lead ECG

In clinical practice, the standard 12-lead ECG is usually used to noninvasively measure the electrical activity of the heart. In the conventional 12-lead ECG, ten electrodes are placed on the patient's limbs and on the surface of the chest. The overall magnitude of the heart's electrical potential is then measured from twelve different views or leads and recorded over a specified period of time, typically ten seconds. This allows for the capture of the overall magnitude and direction of the heart's electrical depolarization during each moment of the cardiac cycle.

Despite its utilization, this technique still falls short in terms of providing exact information on the localization of regional electrical activity within the heart, such as PVC origin localization, as well as the activation time sequence during arrhythmias [28]. Studies has shown that additional ECG leads can enhance the precision of diagnosis and, as a result, the forecast for specific cases [63]. Therefore, body surface mapping was introduced for two reasons. First, to enable a thorough exploration of the spread of excitation throughout the thorax. This made it possible to analyze the typical patterns and make inferences about when the activation first occurred in the right and left ventricles. Second, to quantitatively evaluate the electrical information available, with the possibility of subsequently connecting it through an inverse model to epicardial excitation and other related factors [36].

## 2.4 Electrocardiographic Imaging

ECGI is an imaging modality for cardiac electrophysiology and arrhythmias, which noninvasively reconstructs the epicardial potentials with high resolution from body surface potential measurements with the use of patient-specific cardiac MR and CT images [47, 29]. It has been gaining increasing attention from researchers in academia and industry as it overcomes the limitations of the conventional 12-lead ECG.

ECGI studies are based on addressing two key challenges in imaging the electrical activity of the heart, namely the forward and inverse problems in electrocardiography. The forward problem aims to predict the body surface potentials from the known

electrical activity of the heart, while the inverse problem attempts to infer the electrical activity of the heart from noninvasive measurements of the body surface potential (BSP).

## 2.5 Forward Problem of Electrocardiography

A forward problem is a process of calculating the output of a model for given input values. It consists of two steps: first, to resolve the system state using the described physical parameters i.e. to find a **forward operator**, and second, to apply the forward operator to predict the behavior of the system at the given values. The term *forward problem of electrocardiography* refers to the computation of the electric potential field within and on the torso surface resulting from the cardiac electrical activity. The internal structure between the heart and torso surface affects this electric field significantly. The organs like lungs, bones, skeletal muscles, liver, kidneys, fat, and blood are the inhomogeneities in the thorax whose size, location, and properties are important factors in the resulting body surface potentials [40]. This problem can be formulated as a simplified version of Maxwell's equations, known as the quasi-static approximation. This results in Laplace's equation with a boundary condition of [27]:

$$\nabla \cdot \sigma \nabla \phi(r) = 0, \quad r \in B; \tag{2.2}$$

$$\nabla \phi(r) \cdot n_B = 0, \quad r \in S_B, \tag{2.3}$$

where $r$ is the spatial coordinate, $B$ is an isotropic torso volume with its scalar conductivity $\sigma$, $\phi(r)$ is the extracellular potential at the point $r = (x, y, z)$, and $S_B$ is the torso surface. Therefore, to solve either the forward or the inverse problem of electrocardiography first a geometric model needs to be considered; then a proper numerical method is to be utilized respectively.

There are multiple approaches that can be used to solve this problem, which depend on the specific volume conductor (torso) model and the configuration of the cardiac model. The heart can be represented using discrete source models, such as a single dipole [55], multiple dipoles [45], multipoles [17], or cardiac surface potential models [20, 36]. The core idea behind the discrete source models is that the electrical behavior of the heart can be accurately represented by a simple current source, par-

ticularly when viewed from a distance such as the surface of the body. This offers an advantage in that it reduces the number of parameters needed to describe the sources, which in turn simplifies both the forward and inverse problems associated with the modeling process. However, the absence of uniqueness in the inverse problem of electrocardiography greatly restricts the application of these models [51].

The underlying notion of surface potential models is that the potentials measured on any closed surface that fully encloses all active cardiac sources provide a fully equivalent representation of the actual cardiac sources. For the sake of ease and accuracy in determining source parameters, it is typical to choose the epicardium (or pericardium) as the enclosing surface. The difficulty then lies in creating a mathematical model that can predict potentials throughout the thorax, including the body surface, based on this source [36]. In the mid-1970s, Barr and his team successfully solved this problem using the boundary element method (BEM), which also offers a straightforward numerical solution [4, 5]. BEM relies on a grid of boundaries encircling a region, such as the surfaces that envelop the heart, torso, and internal organs with varying electrical conductivity. It is better suited to homogeneous/inhomogeneous but isotropic tissues than regions with anisotropy.

Other common approaches for solving this problem are volume methods, like the finite difference method (FDM) and the finite element method (FEM). In the former, the torso geometry is represented by a three-dimensional grid of discrete nodes. Resistive elements are specifically chosen to reflect the resistance of the torso and are situated between the nodes. For every node, Kirchhoff's current law is employed, resulting in a number of equations that describe the potential between adjacent nodes [20]. On the other hand, FEM uses a set of volume elements of tetrahedra or hexahedra shapes to estimate the torso geometry.

The advantages of FEM and related volume methods are their capability to account for various types of tissue conductivity, and the availability of efficient computational tools that enable effective implementation. An advantage of using BEM is that it involves a smaller number of nodes or degrees of freedom in the computation process in comparison to FEM. This is because BEM only employs surface nodes as opposed to volume nodes, reducing the number of computations required [20].

The solution of the forward problem can be represented as the forward operator $A$ in the equation:

$$y = Ax, \tag{2.4}$$

where $A \in \mathbb{R}^{MxN}$, $x \in \mathbb{R}^{Nx1}$ is the heart potential vector and $y \in \mathbb{R}^{Mx1}$ is the resulting body surface potential vector.

The discussed multiscale nature of the ECG forward problem makes the accurate calculation of the body surface potentials challenging. The larger the number of inhomogeneities and their properties considered, the greater will be the computational complexity of the problem. Computer memory and computational capacity limitations prompt simpler mathematical modeling and formulation of the problem such that a trade-off between accuracy and complexity is found. The reliability of solving the inverse problem in electrocardiography heavily relies on the precision of the forward problem formulation [7].

## 2.6 Inverse Problem of Electrocardiography

The primary objective of the inverse problem of electrocardiography is typically to assess the condition of the heart based on body surface measurements. It is important to note that forward solutions only describe potential paths for source-measurement relationships, and do not demonstrate causality by themselves. It is conceivable that different parameters or models in forward solutions could lead to comparable measurement predictions. To prove causality and ensure uniqueness or to quantify the uncertainty in the forward predictions, an inverse solution is required. This inverse problem is ill-posed, meaning that small variations in the data, such as measurement noise or geometric errors that are practically unavoidable, can result in large and unbounded errors in the solution.

There are various deterministic techniques that can be used to address the ill-posed nature of this problem such as Tikhonov regularization [59], minimum residual method (MINRES) [22], generalized minimal residual (GMRES) [47], truncated singular value decomposition (TSVD) [23], and conjugate gradient methods [22]. To improve the generalization performance, regularization techniques impose constraints

on the solution. The spatial and temporal characteristics of the cardiac sources, allow regularization to be applied in both domains for increased accuracy. Tikhonov regularization is a commonly used technique for inverse problems to avoid instability [9], that can be used in ECGI [47].

Understanding the normal cardiac excitation is crucial for understanding and treating arrhythmias. Epicardial breakthroughs happen when the activation wavefront reaches the epicardium and penetrates its surface. The timing and position of these occurrences supply crucial data regarding the sequence of ventricular activation. In the distant past, the lack of a non-invasive imaging technique for evaluating cardiac electrical function prevented the examination of normal cardiac excitation in healthy individuals under typical physiological conditions. However, with the development of ECGI, it has been presented as a research tool in physiological studies both to investigate the normal human cardiac activation and repolarization of healthy adults [48]. Detection and quantification of ventricular and atrial arrhythmia in patients have also been studied in the past decades [70, 19, 54, 26].

A limited number of ECGI studies for the localization of spontaneous PVCs have been conducted to date. The existing studies have concentrated on specific PVC types like idiopathic PVCs, idiopathic Outflow Tract Ventricular Arrhythmias (OTVAs) [67, 71] or patient cohorts [42] with the use of 12-lead ECGs. According to Yamada [67] twelve-lead surface ECG algorithms are highly accurate in pinpointing the origin site of idiopathic PVCs. However, the precision of these algorithms may be constrained by various factors such as the patient's physical characteristics, heart rotation, specific conduction properties, the presence of structural heart disease, and other similar aspects. Zhou $etal.$'s article [71] demonstrated that ECGI has greater accuracy in differentiating the right ventricular outflow tract (RVOT) from the left ventricular outflow tract (LVOT) and the septum from the free wall in the RVOT, which enables precise prediction of the origin of OTVAs. This capability of ECGI surpasses that of traditional 12-lead ECGs.

The fastest route algorithm has been used for PVC localization on patient-specific models and myocardial activation with 12-lead ECG by first converting activation isochrones into ECG waveforms and then comparing every millisecond of the simu-

lated ECG with the measured ECG [62]. Another study with 12-lead ECGs for paced PVC localizations [34] shows the sensitivity of activation time mapping is influenced by variations in both the geometrical model and the placement of time markers, although it is comparatively less affected by changes in the body position.

Recently, learning-based methods have been used for PVC identification [69], PVC detection [35], arrhythmia classification [61], and PVC monitoring in portable devices [10] using the ECG recordings. The aforementioned studies have exclusively relied on the MIT-BIH database [41] as their source of training data, and they do not solve the inverse ECG problem. The effectiveness of their proposed techniques cannot be extrapolated to alternative datasets. However, they present promising results for state-of-the-art learning-based ECGI.

There is a lack of spontaneous PVC data for research. The previous studies have mostly used the pacing data available in EDGAR data repository [3] for PVC origin prediction [25], analyzing the geometrical constraint [56], and creating a simulated dataset for paced data [53].

## 2.7 Limitations of Current Approaches

There are some limitations linked to the utilization of the 12-lead ECG algorithms. For instance, accurate measurement of various ECG parameters is essential for several algorithms, which can lead to inconsistencies and heterogeneities between assessors. This is particularly true in situations involving wandering baselines, lead noise, and the absence of electronic calipers [71]. The main constraint of ECGI is the smoothing effect that inner organs have on the projection of cardiac potentials into the body surface, which leads to the loss of sharp morphologies and sudden transients [26].

Another limitation is that the current state of available clinical data is inadequate to conduct a thorough investigation into spontaneous PVCs, and the existing studies have relied heavily on a limited range of datasets, resulting in insufficient generalization. In order to comprehensively investigate the localization of PVCs in clinical settings, it is imperative that future research incorporates a wider range of datasets with preferably known PVC origin sites.

The present study holds considerable significance due to its exploration of spontaneous PVC localization utilizing a novel dataset that has not previously been examined. Furthermore, the utilization of relatively simple techniques, such as Tikhonov regularization, has yielded satisfactory outcomes, further adding to the study's significance.

# CHAPTER 3

# METHODS

In this chapter, we introduce the clinical data and the problem definition and explicate the relationship between the electrical activity of the heart and the corresponding activity on the surface of the body. We will then delve into the various solution algorithms used to address the inverse problem in detail. Finally, we discuss the evaluation metrics employed to assess the results.

## 3.1 Clinical Data

The clinical data used in this study contains the body surface potential measurements of 10 patients with spontaneous PVC that were indicated for RFA. The measurements were obtained by ProCardio measuring system [33] with 128 electrodes, organized in 16 strips with 8 electrodes around the chest. This data has been provided by the Institute of Measurement Science, Slovak Academy of Sciences (SAS) as part of the project "ClinECGI: Performance Evaluation of Noninvasive Electrocardiographic Imaging for the Localization of Premature Ventricular Contractions from Clinical Data" jointly supported by Scientific and Technological Research Council of Turkey (TUBITAK, grant no 120N200). Computed Tomography (CT) scan of each patient was procured while the electrodes were affixed to the torso. A patient-specific torso model was created by segmentation of these CT scans, an example of the geometries can be observed in Fig. 3.1 and 3.2.

The invasive heart mapping of patients was generated during the RFA procedure and presented for assessment by a physician. The estimated ablated region information

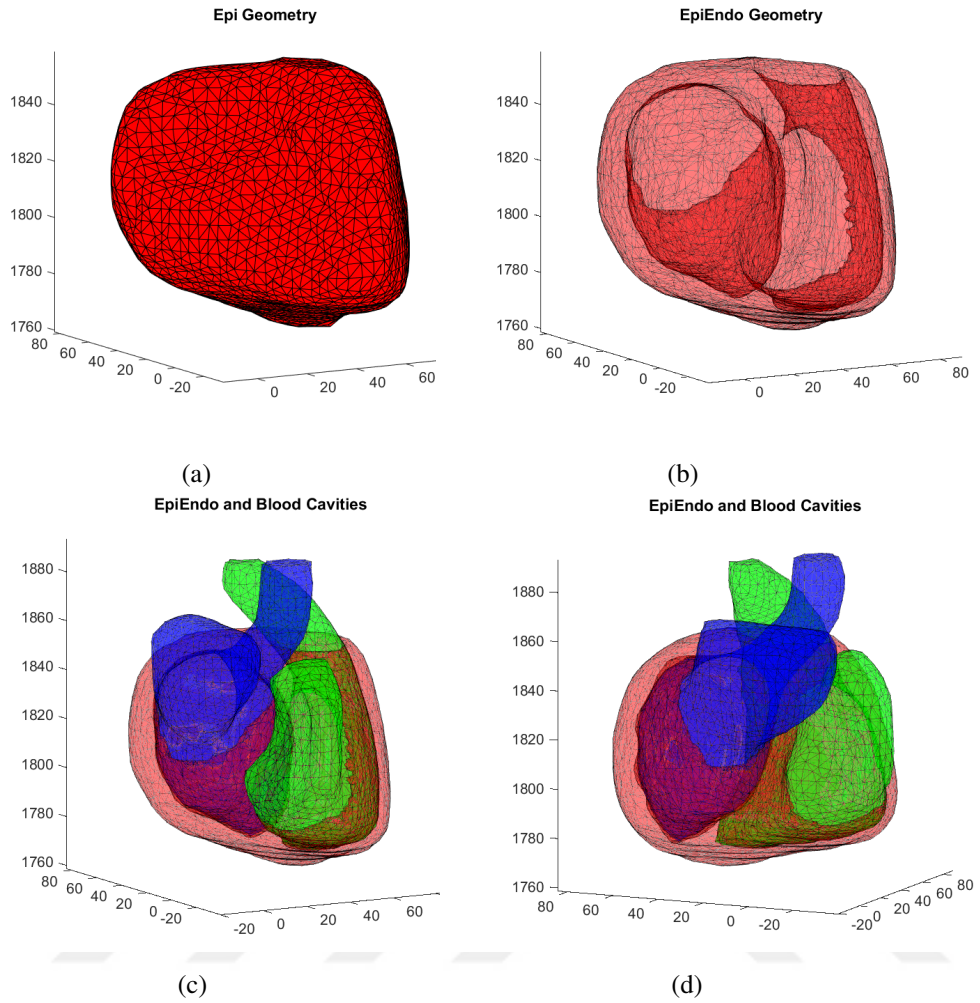


Figure 3.1: Heart geometries all from the same view angle: a) Epicardium surface, b) Epicardium-Endocardium surface, c) and d) Epicardium-Endocardium surface with blood cavities blue as left ventricle cavity green as right ventricle cavity respectively from two different view angles.

was then recorded. In table 3.1 a brief description of each patient's procedure and diagnosis are listed along with their age and the mapping system used for cardiac mapping. There are a total of 12 patients with irrelevant patient numbers in PXXX format. Due to inaccurate mesh generation in the geometries of patients P024 and P027, they have been excluded from our analysis with HBLT models explained in the further sections.

The measurement duration is subject to variation, with a range extending from a minimum of 5 minutes to a maximum of 20 minutes. The measured signals are processed using a high pass filter with a finite impulse response designed by the windowing

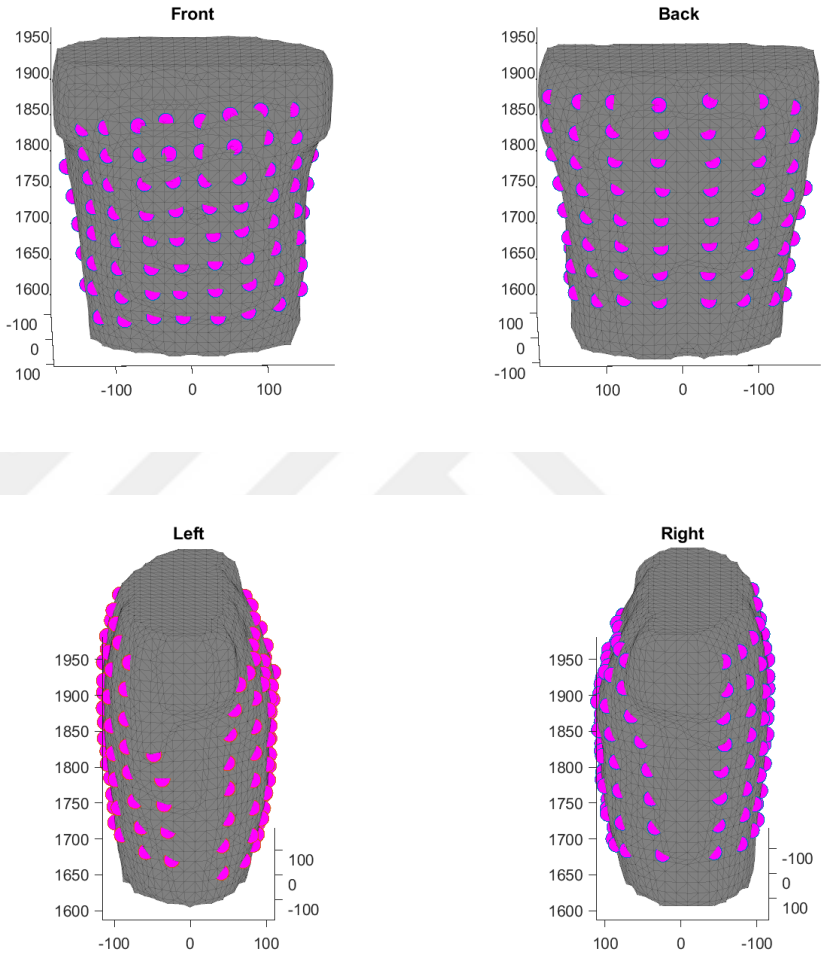


Figure 3.2: A sample of patient torso geometry and the electrodes positioned on it from the front, back, left, and right views.

Table 3.1: Patient Information

| Patient # | Age | Description | Meas-RFA Interval (days) |
|---|---|---|---|
| P001 | 17 | Ablation in LVOT. The focus was on the septum near the atrioventricular node The earliest signal was detected in the left ventricle, at the septum, towards the back. | 180 |
| P002 | 63 | Ablation in the anteroseptal part of the RVOT. | 282 |
| P004 | 72 | Ablation in RVOT, anterolateral on a free wall. | 5 |
| P008 | 46 | Focus in RVOT, upper part, laterally. | 2 |
| P010 | 59 | The focus is in the septum at the LVOT level, more backwards. The earliest signal was detected near his bundle and thus the patient did not undergo ablation. | 330 |
| P020 | 37 | Ablation in right ventricle. | 42 |
| P021 | 33 | The earliest signal was detected near to the his bundle, ablation in the left ventricle. | 2 |
| P023 | 38 | Ablation in septum. | 380 |
| P024 | 79 | Ablation under the aortic valve, at the interface of the right and left coronary cusp. | 8 |
| P027 | 57 | Ablation in RVOT, under the pulmonary valve. | 425 |
| P029 | 64 | Patient with anterior infarction. Ablation in RVOT, under pulmonary valve, anterior free wall. | 0 |
| P036 | 61 | Ablation at the interface of the right and left coronary cusp. The earliest signal was detected in the aorta. | 150 |

method using the Blackman-Harris window with a cut-off frequency of 0.5 Hz. In the chosen signal, R-peaks were found for all cardiac cycles and the cycles are clustered according to their morphology. Then the signals in clusters for PVC beats are aver-

aged. Finally, the starting time instant is estimated for the PVC beat and all signals were corrected by a constant value in such a way that at this instant the BSP value was zero. This signal averaged PVC beat is used for ECGI [57].

Electrodes that exhibit excessive levels of noise or have ambiguous placement in CT scans have been designated as bad leads and removed from the analysis. A sample of averaged and corrected BSPs of a patient (P001), with a total of 128 leads, is demonstrated in Fig. 3.3.

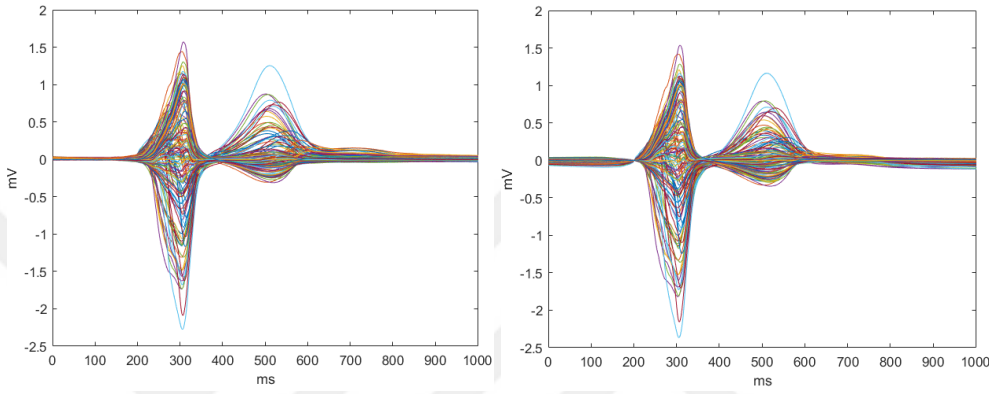


(a) Averaged BSPMs before correction (b) Averaged BSPMs after correction

Figure 3.3: The average signals recorded from all leads for a patient's body surface potentials, (a) before correction of the PVC beat starting point to zero and (b) after correction

## 3.2 Problem Definitions

In order to obtain a feasible solution for the inverse problem of electrocardiography, the temporal and spatial aspects of it needs to be formulated. First, the mathematical model is obtained by solving the forward problem. Then, the inverse problem can be solved based on the chosen cardiac source model.

### 3.2.1 Potential-Based Problem

Here, two source models for heart potentials are used: Epi (i.e., epicardial electrograms) and EpiEndo (i.e., epicardial-endocardial electrograms). Given the BSPMs,

Epi, and EpiEndo potentials are estimated using the following linear equation:

$$\mathbf{y}(k) = \mathbf{A}\mathbf{x}(k) + \mathbf{v}(k),\ k = 1, 2, \ldots, K, \tag{3.1}$$

where $\mathbf{x}(k) \in \mathbb{R}^{N\times 1}$ are the heart surface potentials and $\mathbf{y}(k) \in \mathbb{R}^{M\times 1}$ are the corresponding BSPs at time instant $k$. $\mathbf{A} \in \mathbb{R}^{M\times N}$ is the forward transfer matrix and $\mathbf{v}(k) \in \mathbb{R}^{Mx1}$ represents noise in the measurements. Depending on the source model, $\mathbf{x}(k)$ corresponds to either the epicardial surface or the combined epicardial-endocardial surface potentials with $N$ as the number of nodes on the heart, $M$ as the number of ECG electrodes, and $K$ is the number of time samples.

Given the heart, torso, and lung geometries, the forward matrix A is computed with the BEM based on [4] using five geometrical models: one homogeneous and inhomogeneous torso medium with an epicardial surface and one homogeneous and inhomogeneous volume conductor with epicardium-endocardium surface. The conductivity values are chosen as body conductivity equal to 0.2 $S/m$, lung conductivity equal to 0.05 $S/m$, and blood cavity conductivity equal to 0.67 $S/m$.

### 3.3 Inverse Problem of Electrocardiography

To solve the inverse problem of electrocardiography, the forward operator must be known. In other words, a mapping describing the relationship between the heart nodes and body surface electrodes must be available. Here, for solving the forward problem, we first derive a set of coefficients to establish a correlation between the potentials on the irregularly shaped inner surface of a volume conductor and those on its outer surface by interpolation. This correlation applies even when the shapes of either surface are not uniform. Notably, this set of coefficients can be utilized to connect the potentials around the heart with those present on the surface of the body.

The inverse problem is ill-posed, meaning that small variations in the data, such as measurement noise or geometric errors that are practically unavoidable, can result in large and unbounded errors in the solution.

The application of constraints in this method necessitates some prior knowledge of the properties of the solutions. Typically, it leads to spatial smoothing of the epicardial

potentials, which can result in a reduction of spatial resolution and loss of diagnostic information. The method also requires accurate determination of a regularization parameter, the value of which controls the degree of constraint applied [47].

There are various methods available to solve the inverse problem of electrocardiography and address the ill-posed nature of this problem. Tikhonov regularization is one such method, in which a trade-off is achieved between a good fit to the measurements and constraints defined on the solutions [59].

### 3.3.1 Tikhonov Regularization

As a regularization technique, Tikhonov regularization stabilizes the solution by utilizing general knowledge about the solution to constrain it [20]. It can be used for various problems; in this study, the Tikhonov regularization method [59] is used to deal with the ill-posed nature of the inverse electrocardiography problem of 3.1 and the heart potentials were found for each time instant separately such that the cost function below is minimized:

$$\hat{x} = argmin_x(\|Ax - y\|_2^2 + \lambda\|Rx\|_2^2). \tag{3.2}$$

The solution has the form of:

$$\hat{x} = (A^T A + \lambda^2 R^T R)^{-1} A^T y. \tag{3.3}$$

Here, $R \in \mathbb{R}^{NxN}$ is a regularization matrix and $\lambda$ is the regularization parameter for balancing the trade-off between a fidelity term, which measures the accuracy of the data approximation, and the regularization term, that limits the spread of inaccuracies in the data into the calculated approximate solution.

This is only feasible if $A$ is an over-determined matrix. When the number of measurement locations is insufficient compared to the number of parameters that need to be estimated, leading to an under-determined forward transfer matrix $A$, a unique solution cannot be obtained [46].

The regularization matrix $R$ can be chosen based on the desired smoothness of the solution, it can be either an identity matrix or a first or second-order derivative operator. To begin, we utilized the zero-order Tikhonov regularization method, in which

the regularization matrix is the identity matrix, in order to facilitate computations and have a reference point for comparison should we decide to explore more advanced optimization methods in the future. As it is widely acknowledged that an appropriate regularization matrix can produce higher quality solutions than zero-order Tikhonov solutions [44].

The value of $\lambda > 0$ is also critical to the quality of the computed solution: a too-large parameter will result in an over-smoothed solution that lacks important details, while a too-small value will yield a computed solution that is unnecessarily affected by errors that have been propagated [44]. If the heart surface potentials, $x$ are already known, as is the case with simulation or experimental studies, $\lambda$ can be defined as the value that minimizes the relative error (RE), as outlined in the following equation:

$$RE = \frac{\|\hat{x} - x\|_2}{\|x\|_2}. \tag{3.4}$$

However, in clinical tests on humans, epicardial potentials are not known. Therefore, some other method must be used for finding an optimal $\lambda$ value [20]. In this study, we utilized the L-curve method, as described in [32] to determine the optimal value of $\lambda$ at each time instant. This was achieved by selecting the corner point of the L-shaped plot produced by the L-curve method, which plots in log-log scale $\|Ax - y\|_2$ vs $\|x\|_2$ in the zero-order Tikhonov regularization. It is at this point that the minimum norm solution and minimum error properties are jointly satisfied [24]. Then, median of those values was selected as the regularization parameter for all time instants in the inverse problem solution.

For $R = I$, we can use singular value decomposition to find the unknown heart surface potentials as follows:

$$A = U\Sigma V^T \tag{3.5}$$

with

$$U = [u_1, u_2, ...u_m], V = [v_1, v_2, ...v_n]. \tag{3.6}$$

$$\Sigma = diag(\sigma_1, ..., \sigma_n), where \quad \sigma_1 \geq \sigma_2 \geq ... \geq \sigma_n. \tag{3.7}$$

The heart potentials can be estimated by:

$$\hat{x} = \sum_{i=1}^{n} \frac{\sigma_i^2}{\sigma_i^2 + \lambda} \frac{u_i^T y}{\sigma_i} v_i. \tag{3.8}$$

Hence, Tikhonov regularization dampens the impact of division by small singular values as $\frac{\sigma_i^2}{\sigma_i^2+\lambda}$ will go to zero for small singular values, but large singular values still have an effect on the computed solution as $\frac{\sigma_i^2}{\sigma_i^2+\lambda}$ will go to 1 in Equation 3.8.

The application of constraints in this method necessitates some prior knowledge of the properties of the solutions. Typically, it leads to spatial smoothing of the epicardial potentials, which can result in a reduction of spatial resolution and loss of diagnostic information. The method also requires accurate determination of a regularization parameter, the value of which controls the degree of constraint applied [47].

### 3.3.2 AT estimation and PVC Localization

Activation time is the time instant at which the heart cell/tissue depolarizes (in the cell, it is when the TMP is at phase 0, shown in Fig. 2.4). Estimating cardiac activation times can be difficult due to various sources of noise [52]. In such cases, AT maps may appear falsely homogeneous or show artificial lines of block due to over-smoothing or ambiguities in the inverse problem.

In the conventional approach, the local activation time is determined by analyzing the electrograms (EGM) and identifying the timepoint of the steepest downslope in the QRS complex, which represents the onset of electrical activation at that specific location within the heart. This corresponds to the time instant at which the negative of the first derivative of the EGM signal is maximum (or when the first derivative is minimum). When using ECGI, the EGMs may be overly smoothed or have non-standard waveshapes with multiple peaks ("W-shaped") [6]. As a result, accurately determining local activation and recovery times from EGMs is a challenging task. Prefiltering the EGM can remedy this issue to some extent [49].

In order to locate PVCs with precision, it is necessary to have a high degree of accuracy when determining the cardiac depolarization sequence or activation time. To achieve this, a low-pass Butterworth filter with a cut-off frequency of 30 Hz was applied to the reconstructed EGM prior to estimating the activation times, as the accuracy of the activation times is dependent on the accuracy of the heart potential estimations.

Sudden changes in LATs can occur due to signal inaccuracies, to avoid these fluctuations a spatiotemporal method [15] was utilized to regularize AT sequences such that they are smoothed over space. This method involves the use of an adjacency matrix on a graph defined over the geometry to compute partial derivatives of first and second order for the canonical basis of functions on the said geometry. In other words, it calculates the partial derivatives for all possible combinations of setting one node to 1 and the rest to 0 within the given geometry. Then, by using the Hessian approximation of the found matrix, a forward operator is estimated to be used in a regularization method. In this study, we used Tikhonov regularization to obtain a better AT estimation from minimum derivative-based AT. However, alternative methods may also be employed.

For both the derivative-based temporal AT method (from LATs) and the spatiotemporal AT method, the earliest activated node is identified as the PVC origin.

### 3.4 Evaluation Metrics

As ground truth heart potentials are not available, we cannot evaluate the accuracy of our heart potential reconstructions. However, we can evaluate the performance of the proposed AT methods in localizing the PVC origin, by comparing them with the physician-identified ablation points. These points were manually marked on the EpiEndo heart geometry as the true PVC origins for all patients by the physician who applied the RFA procedure. However, the localization errors found for Epi models are calculated with respect to those same ablation points which can be sometimes located inside the Epi geometry. If there are more than one ground truth PVC origins, LE is taken as the average over all LE values for each ground truth annotation.

The position of the successful RFA intervention was estimated additionally as a vertex/vertices of the triangles of the EpiEndo heart model surface by the physician according to the documents from the procedure. Therefore, the accuracy of such estimation can be influenced by a model error. If only one ablation point was assigned, then this error for the EpiEndo surface is zero. Apparently, this error is larger for the epicardial surface, mainly for the patients with ablation points near the septum.

Finally, some errors can be acquired by the personal opinion of the evaluator.

Two forms of assessments are used in the next chapter for three patients as representations of good, bad, and inconsistent cases in the methods behaved. First, a qualitative assessment of heart potential maps, AT maps, and PVC localization on the AT maps is provided for the defined four geometrical models. Then, the effect of an extra inhomogeneity in the model is discussed. Finally, a quantitative assessment is presented by the calculated Localization Errors (LE) in millimeters with respect to the ablation points.

# CHAPTER 4

# RESULTS

In this chapter, we delve into the examination of the efficacy of the methods put forth in the context of utilizing clinical data. This encompasses an appraisal of the calculated heart potentials, as well as an analysis of the activation time sequences, with the ultimate goal of accurately determining the origin of PVCs.

## 4.1 Torso Volume Conductor Models

As explained in Section 3.1, triangulated closed surface geometries of the torso, Epicardium (Epi), Epicardium-Endocardium (EpiEndo), lungs, and left and right blood cavities of each patient are provided. As anticipated, the shapes of the organs for each patient vary. However, the mesh format for each is consistent and closely resembles the geometries depicted in Fig. 3.1 and 3.2, with the latter showing the placement of 128 electrodes on the torso geometry.

We use these geometries to construct five torso volume models, two for each heart geometry, one being homogeneous and the other being inhomogeneous with an additional inhomogeneous model for EpiEndo geometry:

- HT Epi: Homogeneous torso model with Epi geometry as the heart surface.
- HLT Epi: Inhomogeneous torso model with lungs, and Epi geometry as the heart surface.
- HT EpiEndo: Homogeneous torso model with EpiEndo geometry as the heart surface.

- HLT EpiEndo: Inhomogeneous torso model with lungs, and EpiEndo geometry as the heart surface.

- HBLT EpiEndo: Inhomogeneous torso model with lungs and blood cavities, and EpiEndo geometry as the heart surface.

We calculate the results in the subsequent sections using the first four of the aforementioned models, wherein the lungs are considered as the sole inhomogeneity. Subsequently, in Section 4.5, we present the results of the fifth model and explore the impact of incorporating an additional inhomogeneity, such as blood cavities, into the torso model on the inverse solutions.

Given that the true heart potentials are not available, it is not possible to directly evaluate the accuracy of the forward matrix $A$ in 3.1. However, an assessment of the matrix may be performed by evaluating its impact on the solutions to the inverse problem.

## 4.2 Quantitative Evaluation of PVC Localization

In this section, we explore the quantitative performance of our PVC localization by evaluating the Euclidean localization errors found for each model with respect to the specified ablation points in the dataset. For half of the patients, the error values across all five models are rather clustered and are not significantly distant from each other, illustrated in Fig. 4.1, showing the stability of the method over different torso volume conductor models. The total mean and standard deviation results listed in Table 4.1 also confirm the stability of the used method for various models across the dataset. Some inconsistencies between the errors of individual patient models can be observed from the median values. However, the median error values across the models for half of the patients are less than 30 $mm$ and for the other half is around 45 $mm$, illustrated in Fig. 4.1. The total interquartile range (IQR) of each model shows the distribution of the errors is around 30 $mm$, except for HLT Epi and HBLT EpiEndo models that is around 20 $mm$ in Table 4.1.

In this chapter, only a subset of the patient results is presented due to the size of the

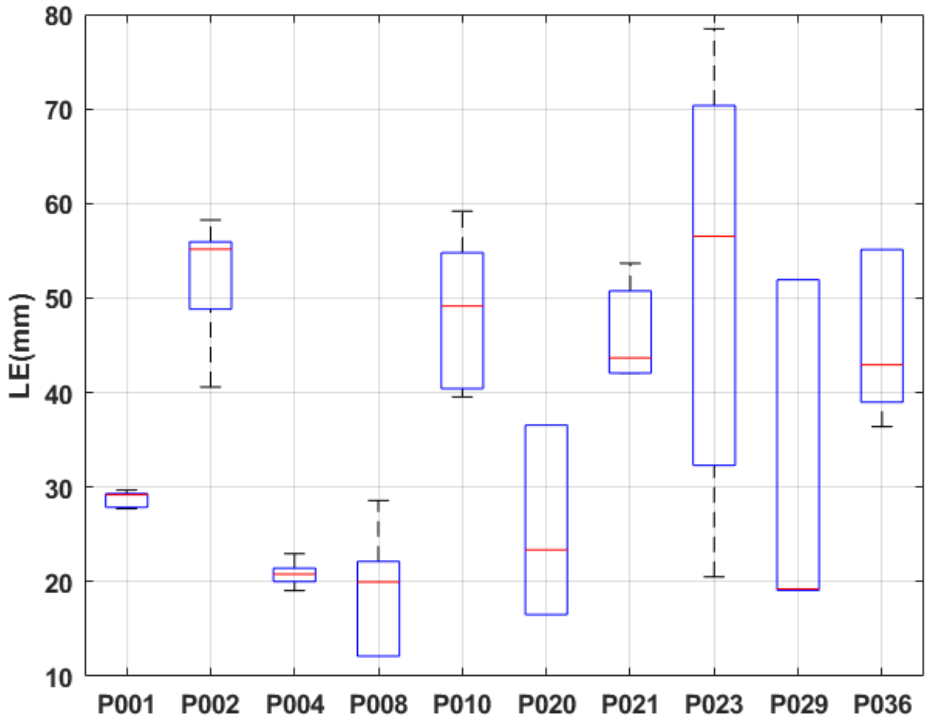


Figure 4.1: PVC origin localization error plot of all five models for each patient, with the red line showing the median of the five model

Table 4.1: Localization errors (mm) of the five models with their mean, standard deviation, median, and IQR values

| Patient # | HT Epi | HLT Epi | HT EpiEndo | HLT EpiEndo | HBLT EpiEndo | mean | std |
|---|---|---|---|---|---|---|---|
| P001 | 27.9 | 27.7 | 29.2 | 29.7 | 29.2 | 28.8 | 0.9 |
| P002 | 58.2 | 51.6 | 55.2 | 55.2 | 40.6 | 52.1 | 6.9 |
| P004 | 20.4 | 20.8 | 23.0 | 20.9 | 19.1 | 20.8 | 1.4 |
| P008 | 20.0 | 20.0 | 12.1 | 12.1 | 28.6 | 18.6 | 6.8 |
| P010 | 59.2 | 40.7 | 49.15 | 53.3 | 39.6 | 48.4 | 8.3 |
| P020 | 16.5 | 16.5 | 23.3 | 25.6 | 23.4 | 21.1 | 4.2 |
| P021 | 42.1 | 42.0 | 53.7 | 43.7 | 49.8 | 46.2 | 5.2 |
| P023 | 36.2 | 78.5 | 56.5 | 67.6 | 20.5 | 51.9 | 23.5 |
| P029 | 51.9 | 51.9 | 19.1 | 19.1 | 19.2 | 32.3 | 18.0 |
| P036 | 39.9 | 36.4 | 55.1 | 55.1 | 42.9 | 43.6 | 8.8 |
| mean±std | 36.1±16.7 | 36.7±17.7 | 36.4±18.8 | 37.8 ± 17.5 | 31.3±11.1 | | |
| med (IQR) | 38.0 (30.0) | 32.1 (19.1) | 39.2 (32.0) | 35.9 (29.4) | 28.9 (19.1) | | |

dataset, with a particular emphasis on the three distinct behaviors exhibited by the methods based on the mean error values in Table 4.1. As an example for good localization performance, the results of patient P008 with a mean error value of 18.6 $mm$

are discussed in the following sections, whereas for a bad performance example, patient P002's results with a mean LE of 52.1 $mm$ are presented. Finally, the consistent performance of the method over different models is discussed in the results of patient P029.

As shown in Table 4.2, homogeneous and inhomogeneous EpiEndo models of P008 and P029 have resulted in smaller LEs, indicating EpiEndo geometry can provide a better representation of the electrical heart activity. The existence of lung inhomogeneity in the models of these three patients does not affect the localization of the sources (LEs) when compared to homogeneous models, and neither does it changes the earliest time detected by the model in Table 4.3. According to this table, the time ranges detected for the potential-based models are slightly larger than the ones of the dipole-based models. Potential-based PVC localization performance is nearly two times more accurate than dipole-based solution for P008, see Table 4.2. In the same table, the mean LEs for P029 are almost the same, however, this is due to the undesirable LEs found by Epi models in the potential-based method. In fact, the potential-based EpiEndo models indicate better estimates for PVC origin of P029 than the dipole-based ones.

Table 4.2: Localization errors (mm) of potential based models with their means and mean LE of dipole based models

| Patient # | Potential-based | | | | | Dipole-based |
|---|---|---|---|---|---|---|
| | HT Epi | HLT Epi | HT EpiEndo | HLT EpiEndo | mean | mean |
| P008 | 20.0 | 20.0 | 12.1 | 12.1 | 16.1 | 32.2 |
| P002 | 58.2 | 51.6 | 55.2 | 55.2 | 55.0 | 36.0 |
| P029 | 51.9 | 51.9 | 19.1 | 19.1 | 35.5 | 31.0 |

Although the mean LE of dipole based PVC origins is in range of 30 milimeters for P002, they are still a much accurate estimate than potential based PVC origin estimates, given Table 4.2.

We are also provided with dipole-based PVC origins and their LEs by the IMS-SAS group in order to gain a more comprehensive understanding of the outcomes, illustrated in Fig. 4.2, 4.3, and 4.4. The potential-based PVC localizations are displayed with square markers. The dipole-based ones are displayed with triangle markers, and

Table 4.3: The earliest time detected for potential based models and dipole based model in miliseconds for each model and the time range detected for both methods

| Patient # | HT Epi | HLT Epi | HT EpiEndo | HLT EpiEndo |
|---|---|---|---|---|
| P008 | 40.84 | 40.96 | 40.97 | 37.82 |
| P002 | 13.8 | 15.46 | 15.1 | 15.34 |
| P029 | 34.05 | 34.46 | 41.57 | 39.72 |

the ablation points are marked with black circles.

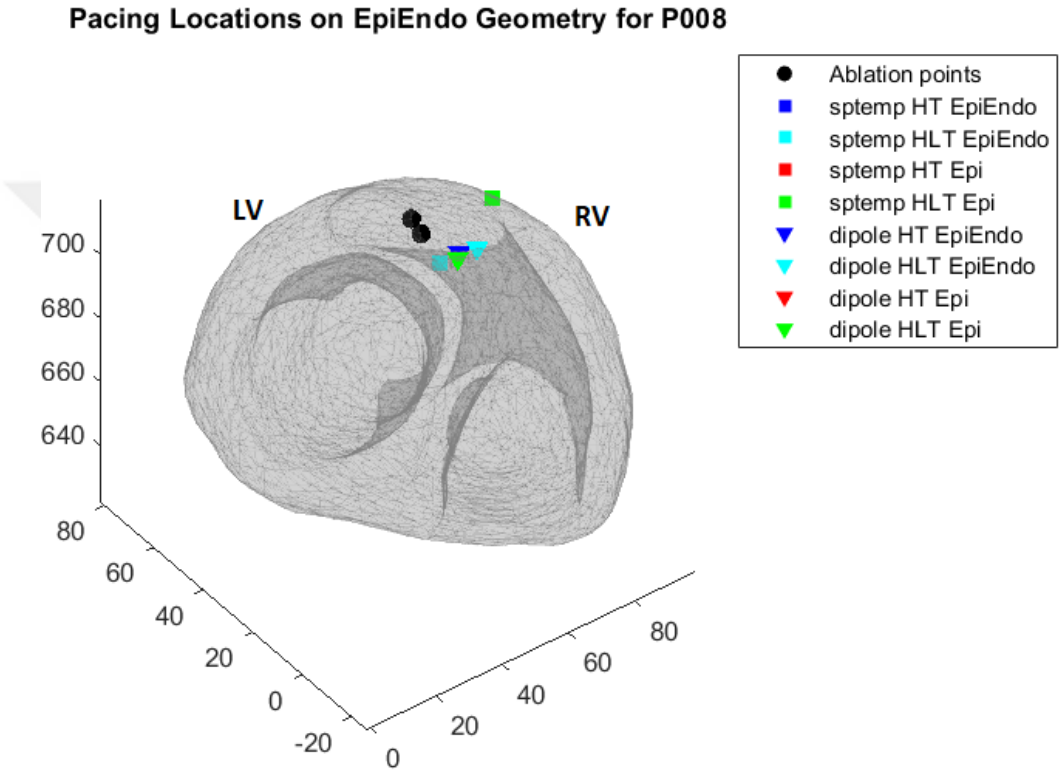


Figure 4.2: Dipole based vs potential based PVC estimates with the physician identified ablation points of P008

The bad and inconsistent examples of the method performance can be seen in the scattered PVC origin estimations in figures 4.3, 4.3, and 4.4. The dipole based PVC origins for P002 look significantly closer to the ground truth than the potential based ones.

However, a similar poor performance for P029 is observed in Fig. 4.4, for dipole based method as the potential based method, suggesting the inconsistency may not be solely due to the method, but rather due to the existence of other factors like noisy

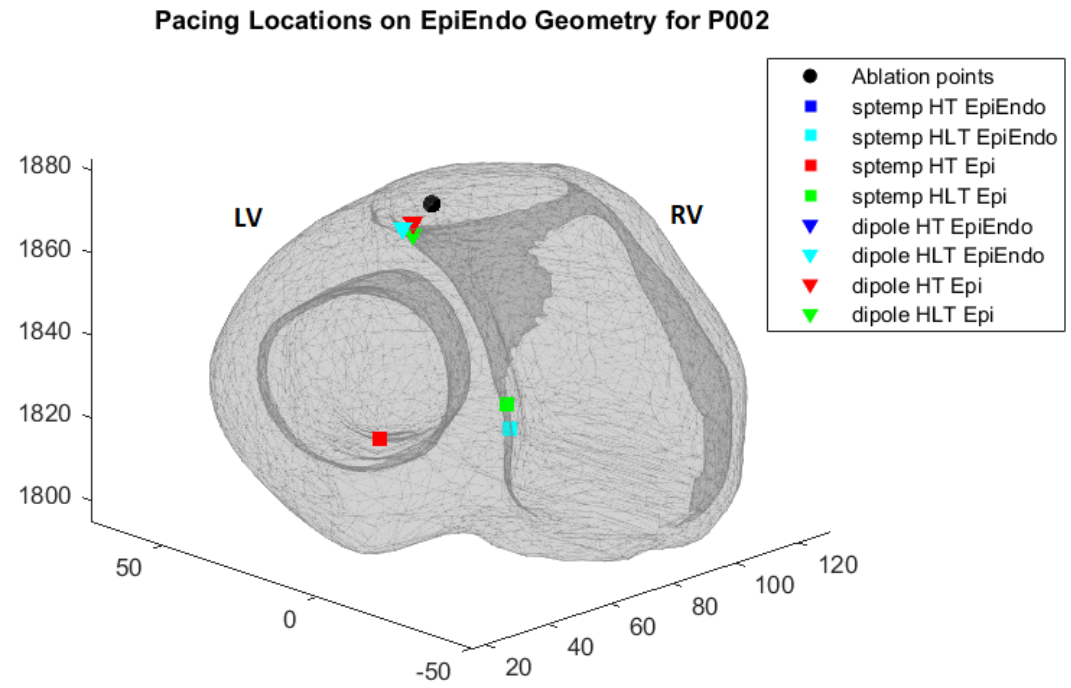


Figure 4.3: Dipole based vs potential based PVC estimates with the physician identified ablation points of P002

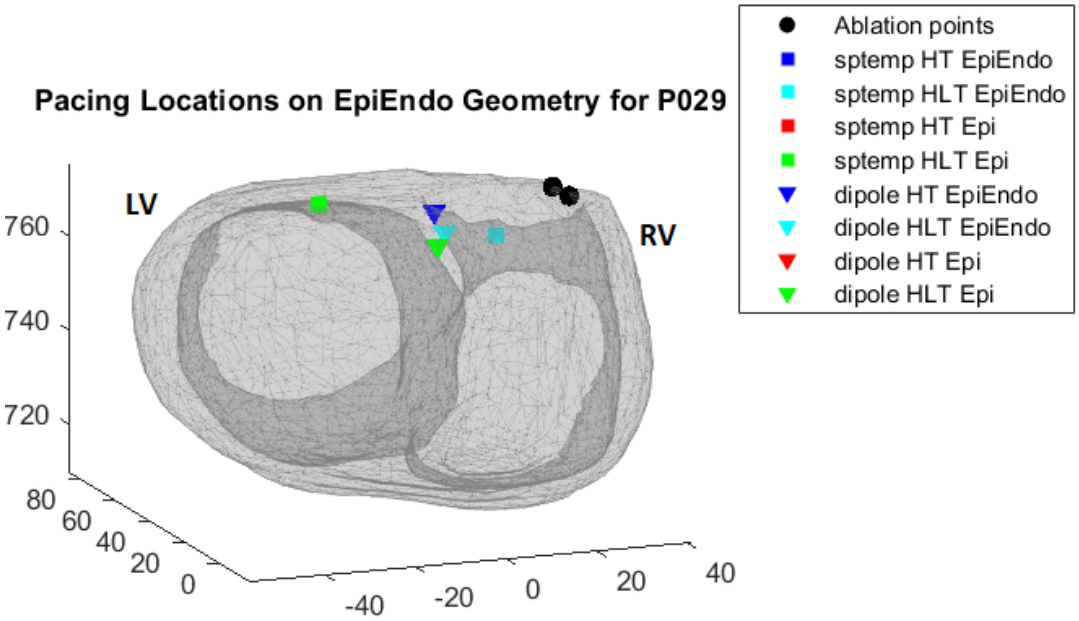


Figure 4.4: Dipole based vs potential based PVC estimates with the physician identified ablation points of P029

measurement, complicated cardiac issues, age, etc.

## 4.3 Heart Potential Reconstruction

The electrocardiograms of all patients are determined through the application of Tikhonov regularization and are subsequently analyzed across various time intervals. The purpose of this analysis is to evaluate the consistency and pertinence of the outcomes with respect to the patients' clinical profiles.

### 4.3.1 Qualitative Evaluation of ECGI

The three evaluation cases of good, bad, and inconsistent performances are explored through the results of patients P008, P002, and P029, respectively. The heart potential distributions of the four torso models for each patient are mapped in Fig. 4.5, 4.6, and 4.8 for three time frames after the QRS starts in each row. In these figures, the red regions highlight higher potential values, or regions of activation. The blue points or regions show small potential values. The propagation can be observed from the variation of potential values in a particular region, in other words, by the color change from blue to red.

The heart potential distributions for the four distinct torso models of patient P008 demonstrate compatibility with the observation that the point of origin for propagation is located in the upper region of the RVOT, see Fig. 4.5. The angle views are identical and the left and right ventricles have been labeled in both the Epi and EpiEndo models for better comprehension. We can see the consistency of the results across the four models with one another. The minimal variations in the potentials between the Epi and EpiEndo models can be attributed to the compactness of the Epi geometry. The EpiEndo geometry, however, provides a more accurate representation of the heart's structure.

Patient P002 underwent ablation in the anteroseptal region of the RVOT, indicating that the focus was situated anterior to the interventricular septum. However, the reconstructed potentials indicate the origin of propagation to be elsewhere, specifically in the posterior of the RVOT and the inferior region of the right ventricle, as depicted in the encircled area of Fig. 4.6. Despite the fact that the results do not align with the patient's clinical description, the reconstructed electrograms across all four models

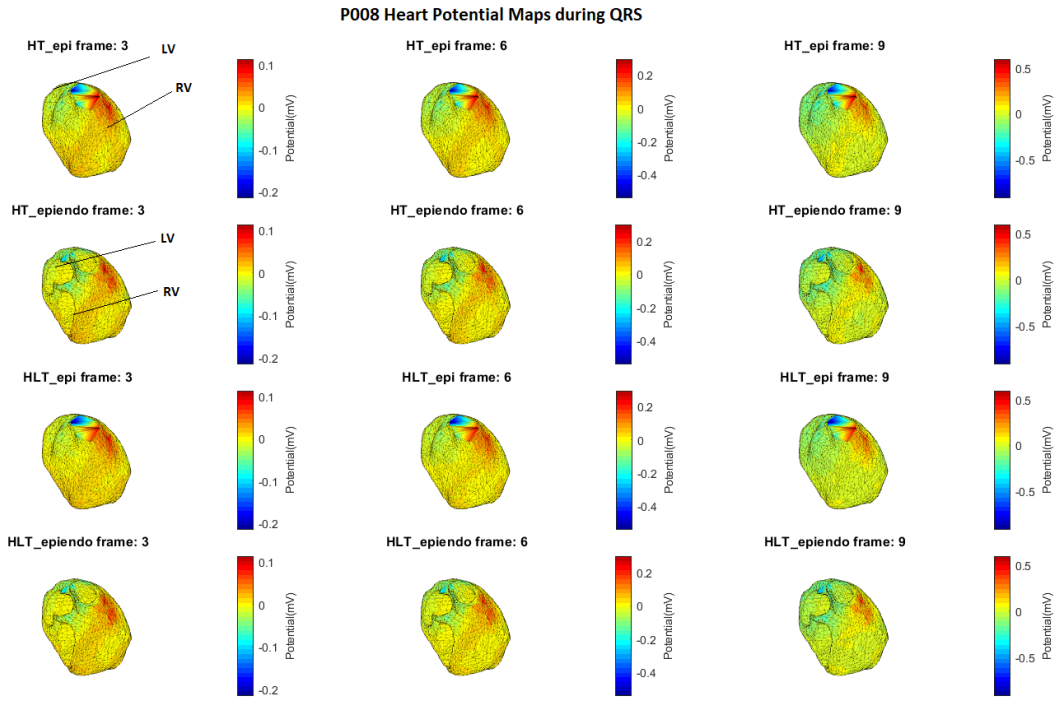


Figure 4.5: Heart potential distribution of patient P008 during the first 9 seconds of QRS

are consistent with each other, showing the stability of the used method. The incompatibility of the results with the ground truth may be due to the long time interval between the measurement and the ablation, given in Table 3.1.

The variation in the compatibility of the results obtained from P002 and P008 with the clinical descriptions may be attributed to the characteristics of BSP signals, illustrated in Fig. 4.7, and the dependency of the reconstructed heart potentials on them. The QRS region for P002 is from 206 to 381 $ms$ and for P008 is from 196 to 341 $ms$.

Lastly, P029 has suffered from an infarction in the anterior region and undergone an ablation procedure in RVOT, located beneath the pulmonary valve and on the anterior free wall. The reconstructed heart potentials show activation origin from the anterior free wall during the 15 seconds of QRS in Fig. 4.8. The left and right ventricles are marked in the figure. The view angle is slightly elevated, and the right and left ventricles can be differentiated by the cavity observed in the EpiEndo models.

As depicted in Fig. 4.9, the body surface potentials of P029 appear to be less distorted in comparison to the previous two patients, with the QRS region spanning from 216

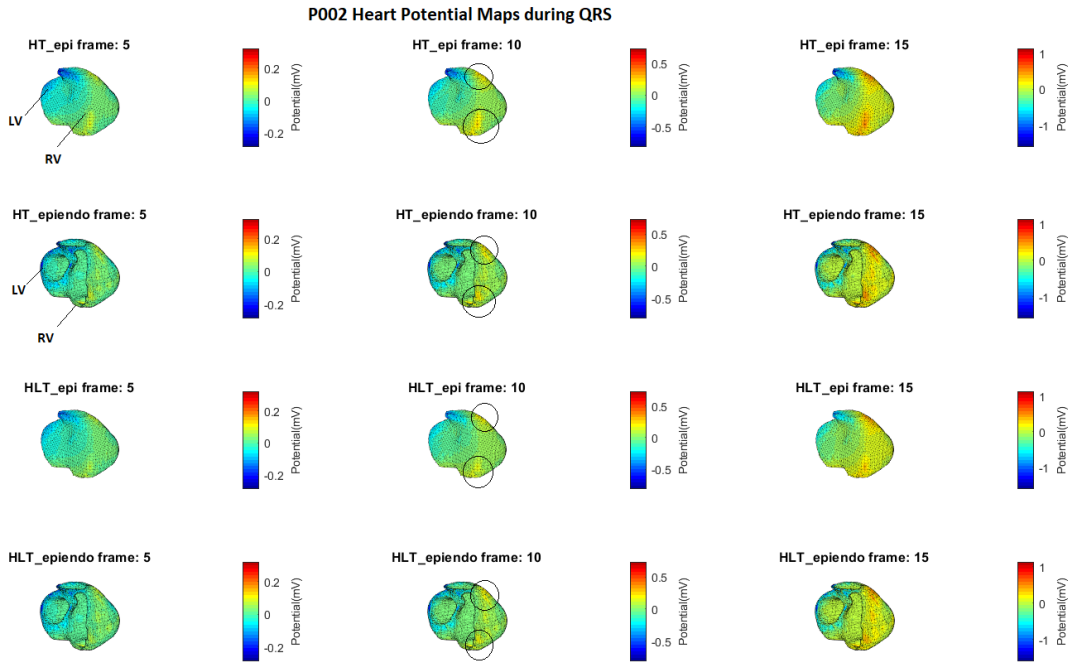


Figure 4.6: Heart potential distribution of patient P002 during the first 15 seconds of QRS

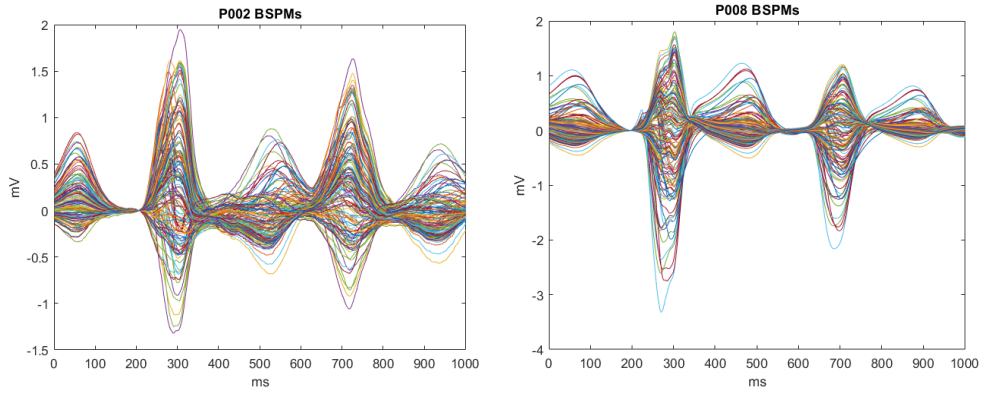


(a) P002 BSPM (b) P008 BSPM

Figure 4.7: The 128 lead body surface potential signals of P002 and P008

to 421 milliseconds. The reconstructed heart potentials are again consistent across all models. The performance inconsistency of this patient arises in the activation time calculation which we will cover in the next section.

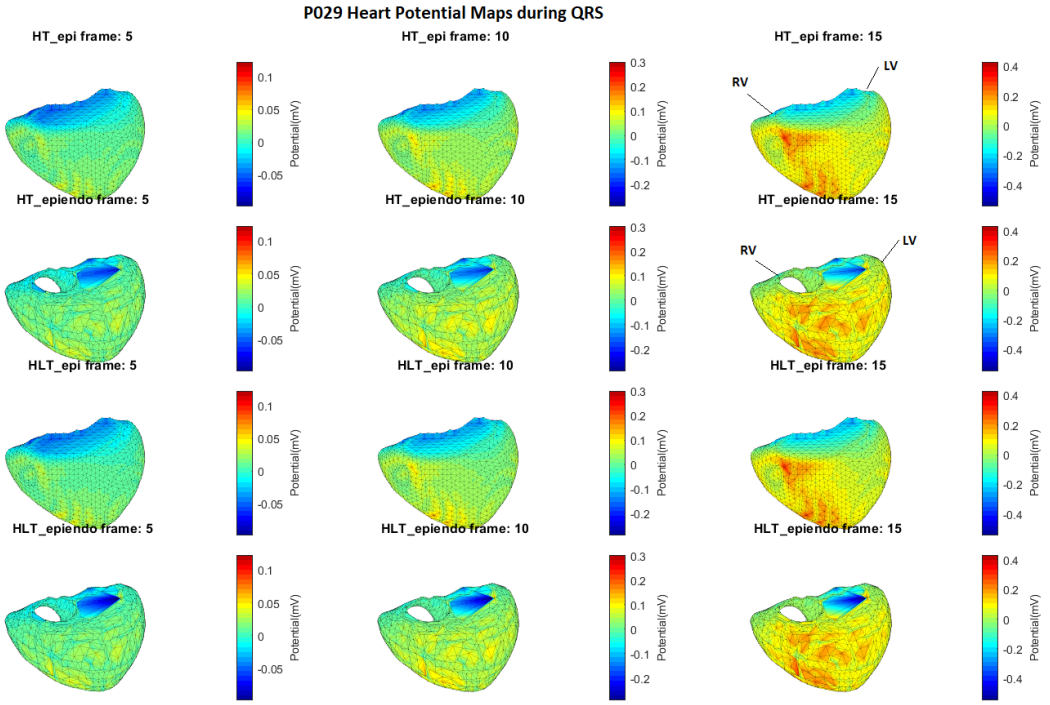


Figure 4.8: Heart potential distribution of patient P029 during the first 15 seconds of QRS.

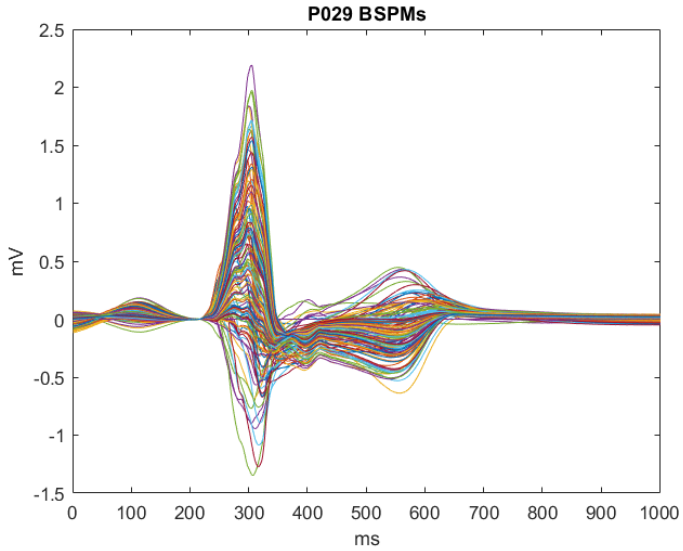


Figure 4.9: The body surface potentials of P029

## 4.4 Activation Time Maps

By utilizing the reconstructed heart potentials of the patients, we are able to estimate the corresponding activation time sequences to eventually localize PVC origin. In order to provide a better understanding of the variations between the methods, the

AT maps obtained through the minimum derivative method and the spatiotemporal method for all four models are illustrated in two columns in Fig. 4.10, 4.11, and 4.12.

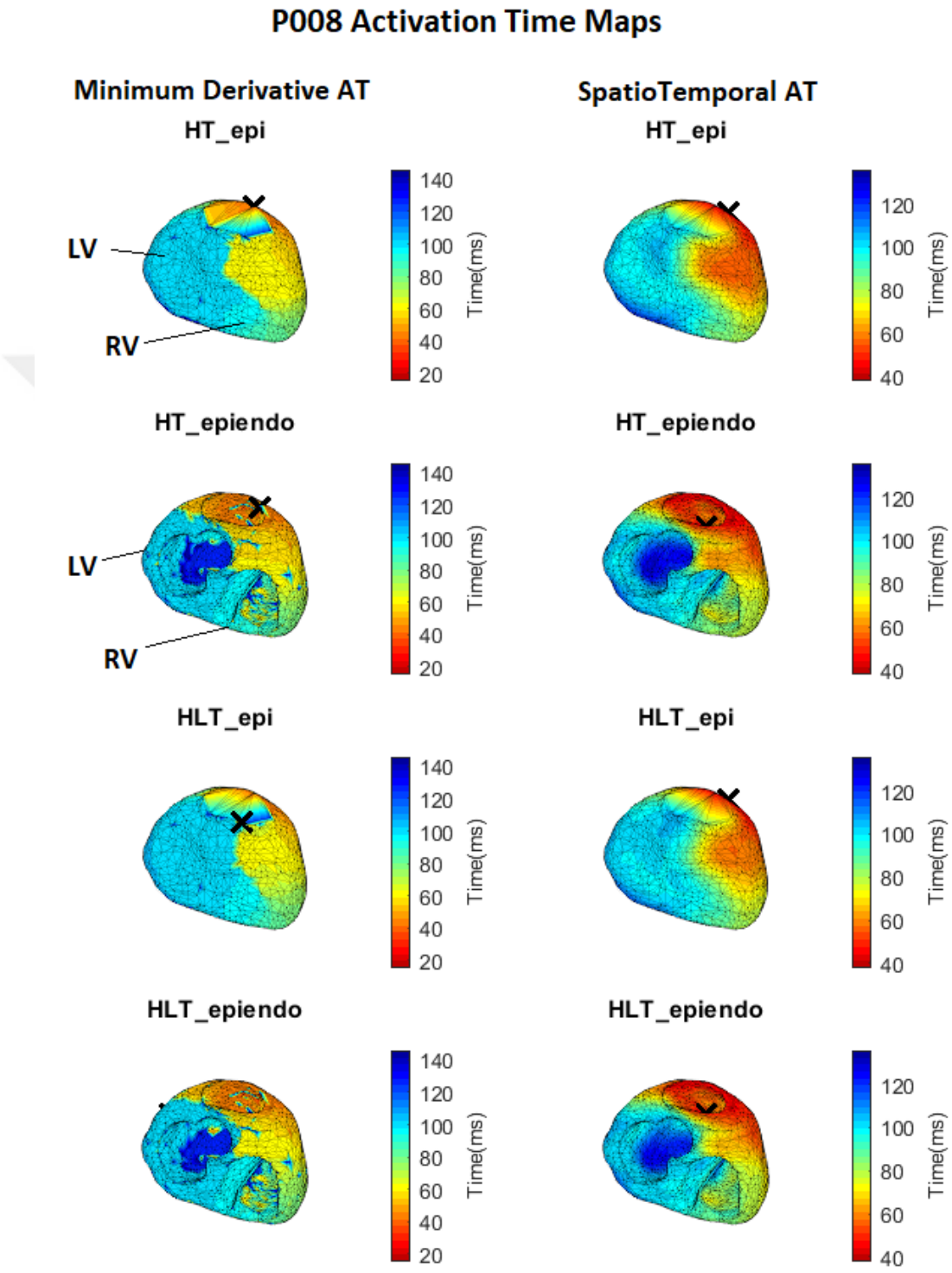


Figure 4.10: The activation time maps of P008 found by minimum derivative and spatiotemporal methods with the cross showing the pacing location.

The left-hand side of the illustrations show maps of activation time based on the minimum derivatives for the first four torso volume conductor models. On the right-hand side, there are spatiotemporal activation time distributions of the same models.

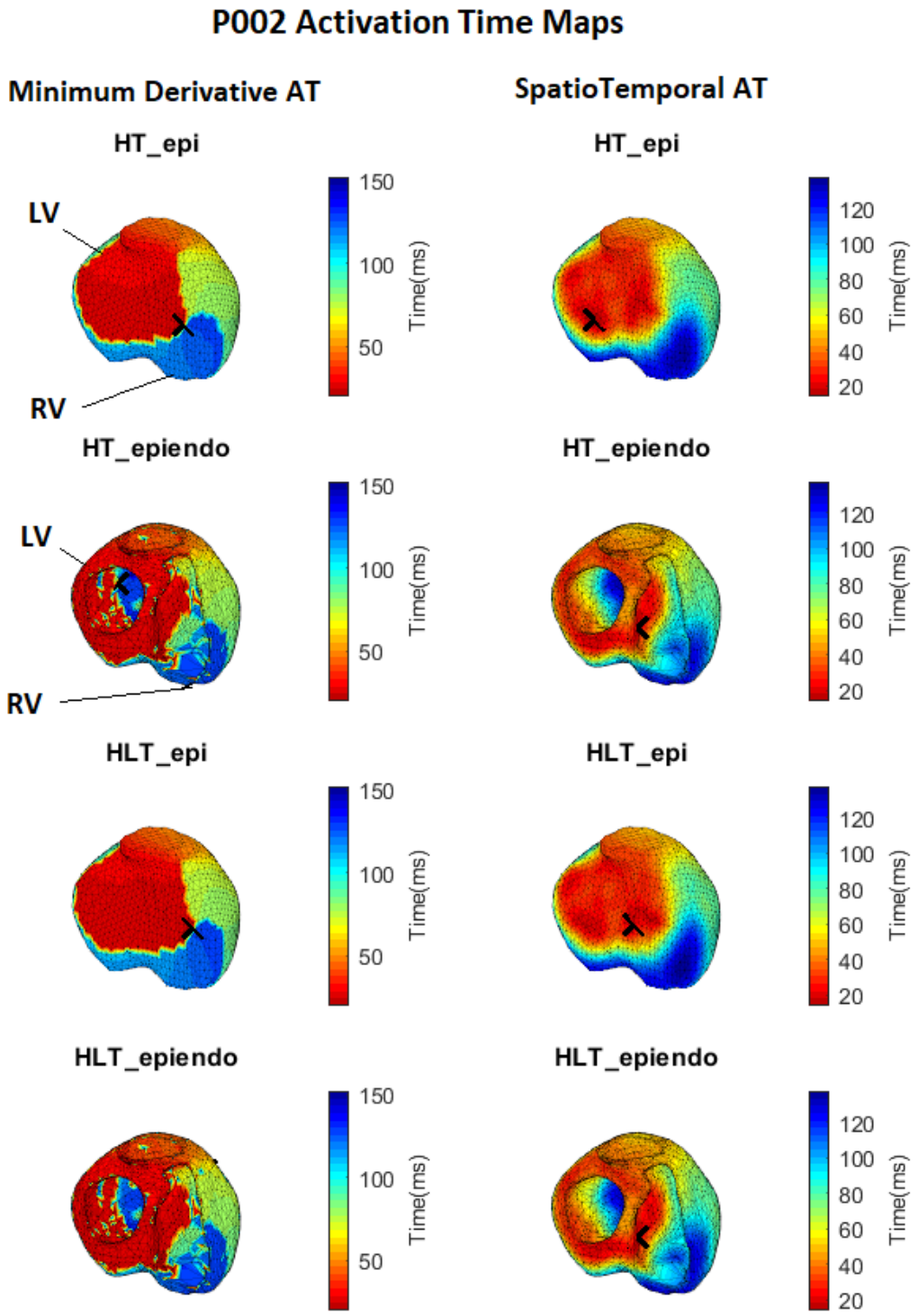


Figure 4.11: The activation time maps of P002 found by minimum derivative and spatiotemporal methods with the cross showing the pacing location

An examination of both sides of the figures for all three patients indicates that using the spatiotemporal method improves the robustness of activation sequences by reducing abrupt changes caused by signal inaccuracies in LATs.

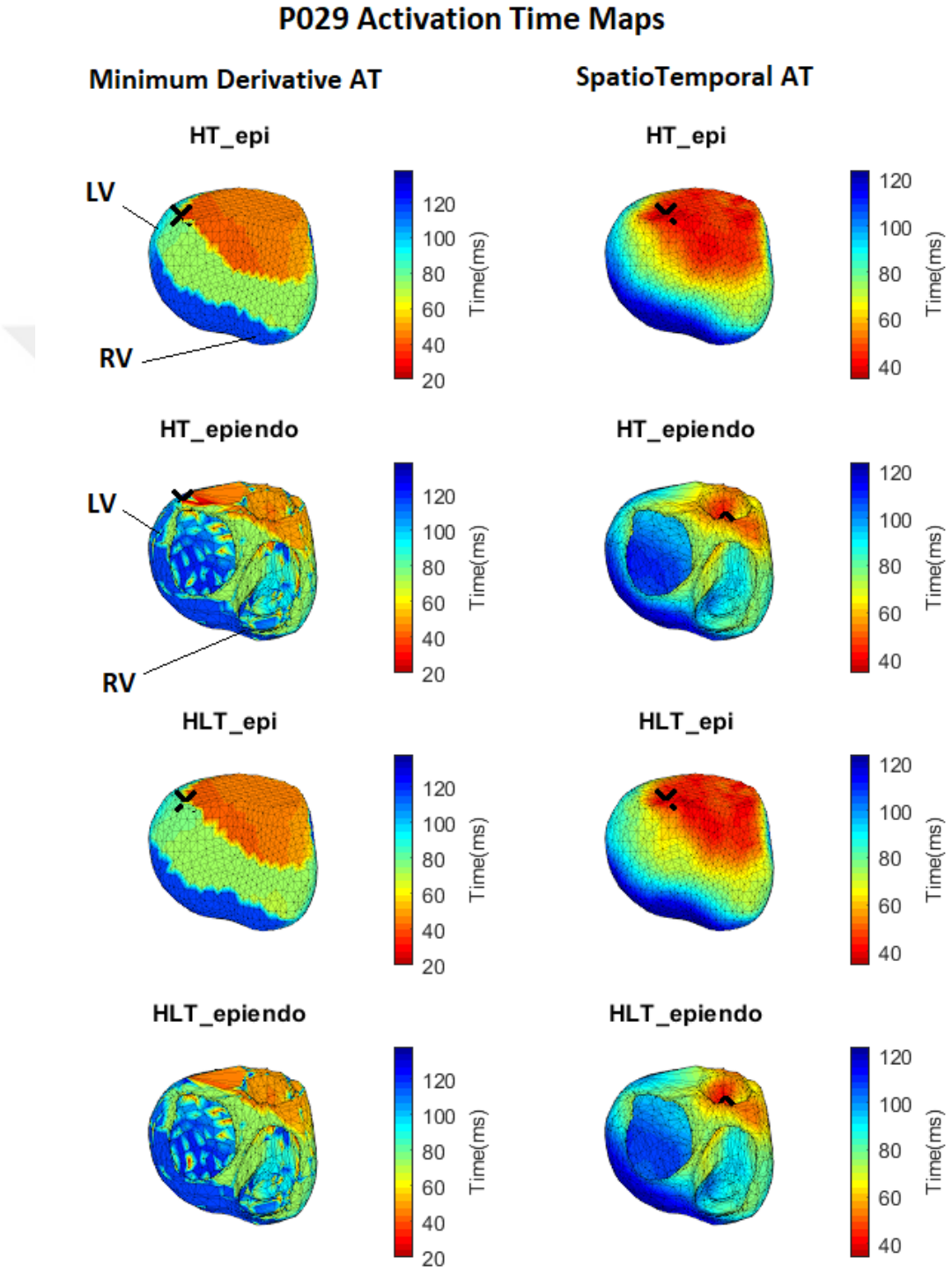


Figure 4.12: The activation time maps of P029 found by minimum derivative and spatiotemporal methods with the cross showing the pacing location

This demonstrates the greater stability of the spatiotemporal AT method. As a result, we choose to use the spatiotemporal AT-based PVC origin localizations as our final estimates, and refer to spatiotemporal AT maps as AT maps.

In the case of P002, we can see in Fig. 4.11 there is a greater discrepancy between the results obtained by the minimum derivative method and the spatiotemporal method, particularly in the EpiEndo models. It is apparent that the spatiotemporal method enhances the activation time sequence obtained through the minimum derivative method. In the illustrated AT map of Fig. 4.13, certain regions are observed to have substantially distinct values in the AT sequence in comparison to their adjacent nodes. The smoothing effect of the spatiotemporal method improves the AT estimation for such regions. Thus, the results obtained through the spatiotemporal method are more stable.

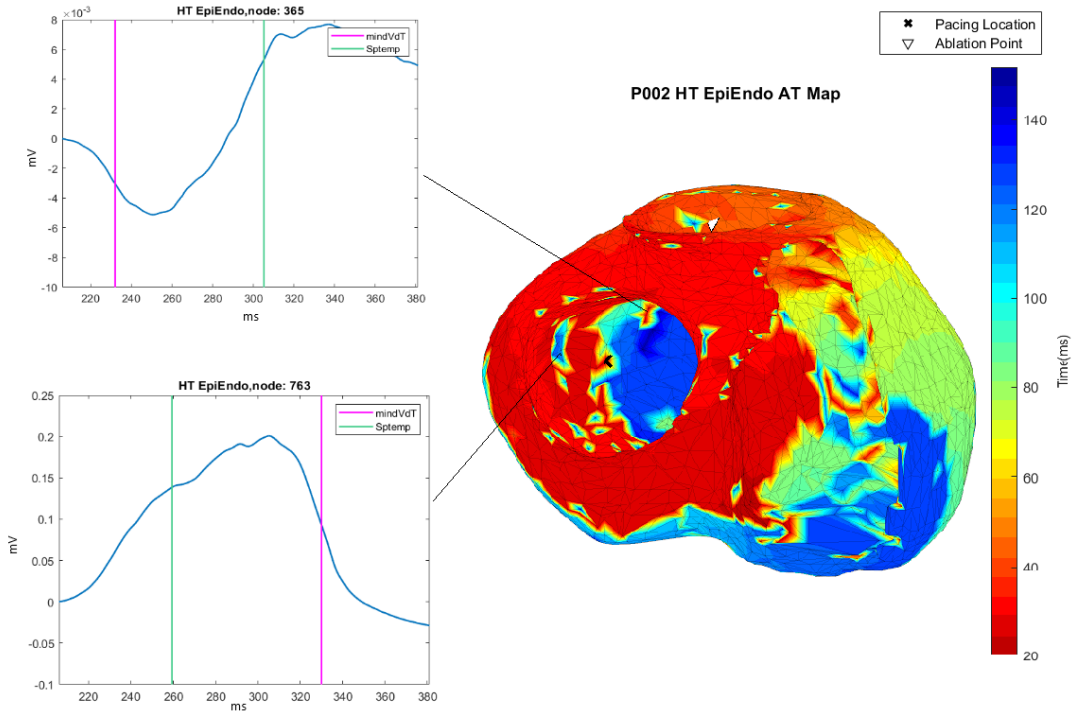


Figure 4.13: The activation time map of P002 HT EpiEndo model found by minimum derivative method and the reconstructed heart potential at node 365 and 763: pink vertical line shows AT found with minimum derivative method and green vertical line shows AT found with spatiotemporal method at these nodes

A comparison of the estimated AT maps of P008 reveals minor discrepancies in both the distribution and the identified PVC origins. The consistency of the AT maps

and PVC origins across both homogeneous and inhomogeneous models of heart geometries with one another and their compatibility with the clinical description of the patient is indicative of the good performance of the methods for this case, illustrated in Fig. 4.14.

The AT maps for all four models of P002 are found to be consistent with one another. However, we can observe in Fig. 4.15, the activation time distributions highlight the left ventricle and do not fully align with the patient's clinical description, which points to the ablation being in the anteroseptal part of the RVOT. One possible explanation for this discrepancy may be the large time interval between the measurements and the ablation procedure, which is approximately 282 days as noted in Table 3.1. In the case of patient P029, a slight variation can be observed between the AT maps of Epi and EpiEndo models in Fig. 4.16. The Epi models highlight a broader activation origin area on the right ventricle side extending to the left ventricle, while the activation distribution in the EpiEndo models is more concentrated around the RVOT, which is consistent with the clinical description.

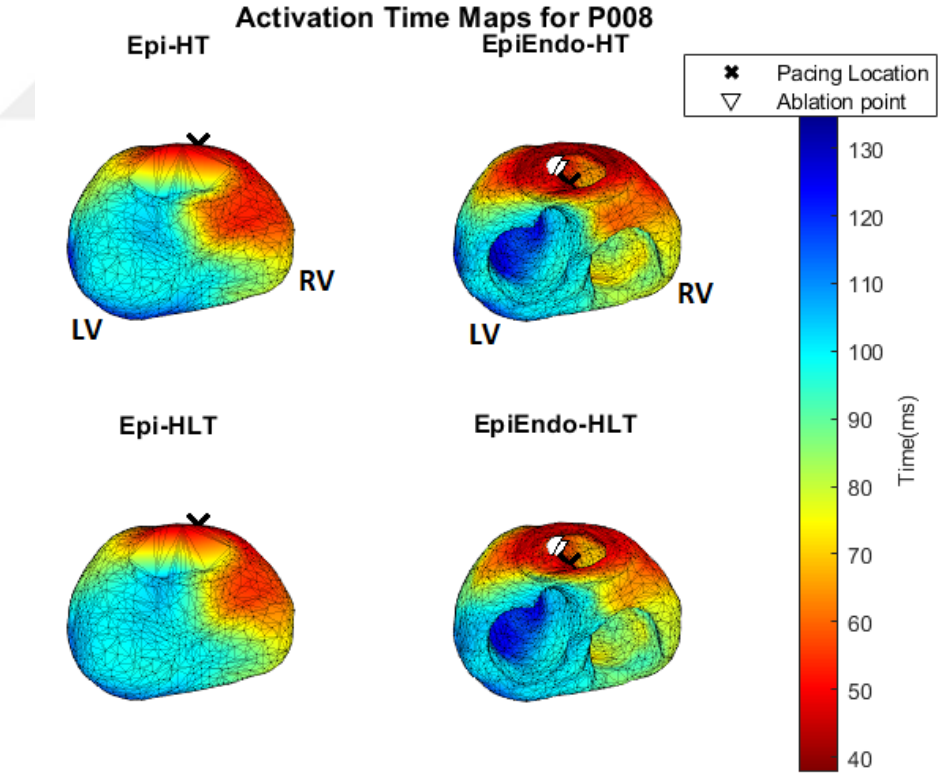


Figure 4.14: The spatiotemporal activation time maps of P008 with ablation points identified by the physician. The ablation points are located inside the Epi models, making them invisible in this figure

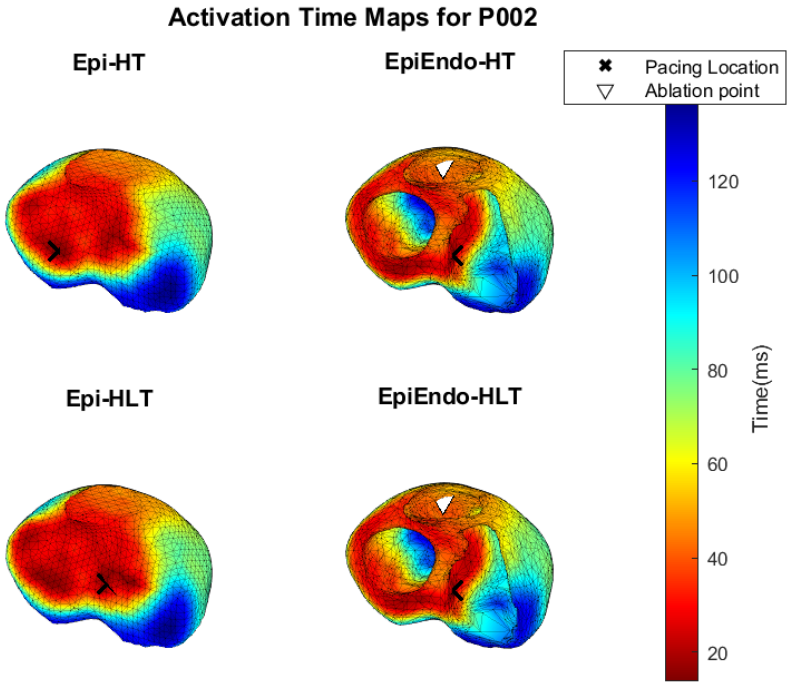


Figure 4.15: The spatiotemporal activation time maps of P002 with ablation points identified by the physician. The ablation points are located inside the Epi models, making them invisible in this figure

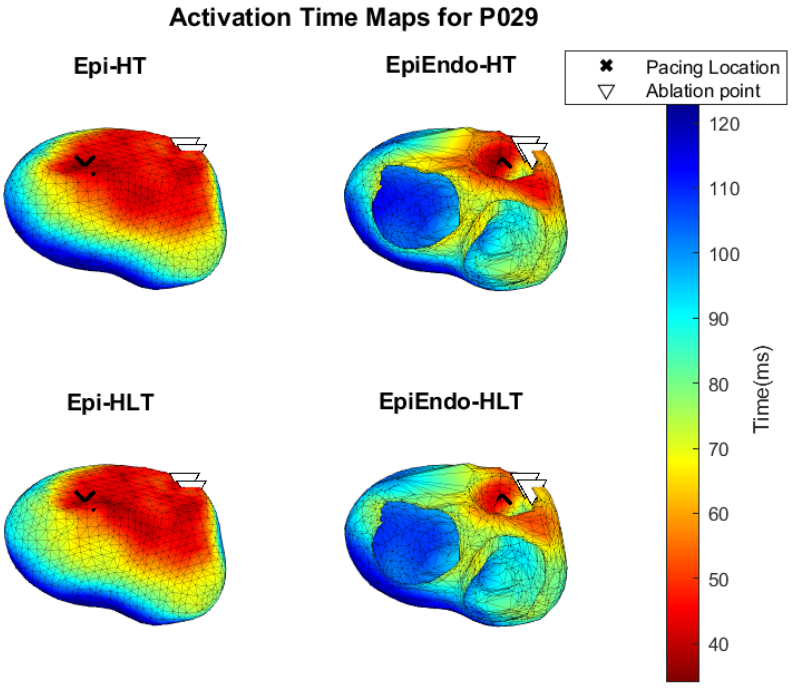


Figure 4.16: The spatiotemporal activation time maps of P029 with ablation points identified by the physician.

## 4.5 Blood Cavity Inhomogeneity Effect

In this section, we investigate the impact of adding an extra inhomogeneity layer to the torso volume condutor model. The activation time distributions are consistent with the previous inhomogeneous models for all the three patients. The activation time distributions for all three model seem to have been improved, showing a more compact activated region and compatibility with the clinical descriptions for the three patients, illustrated in Fig. 4.17,4.18, and 4.19.

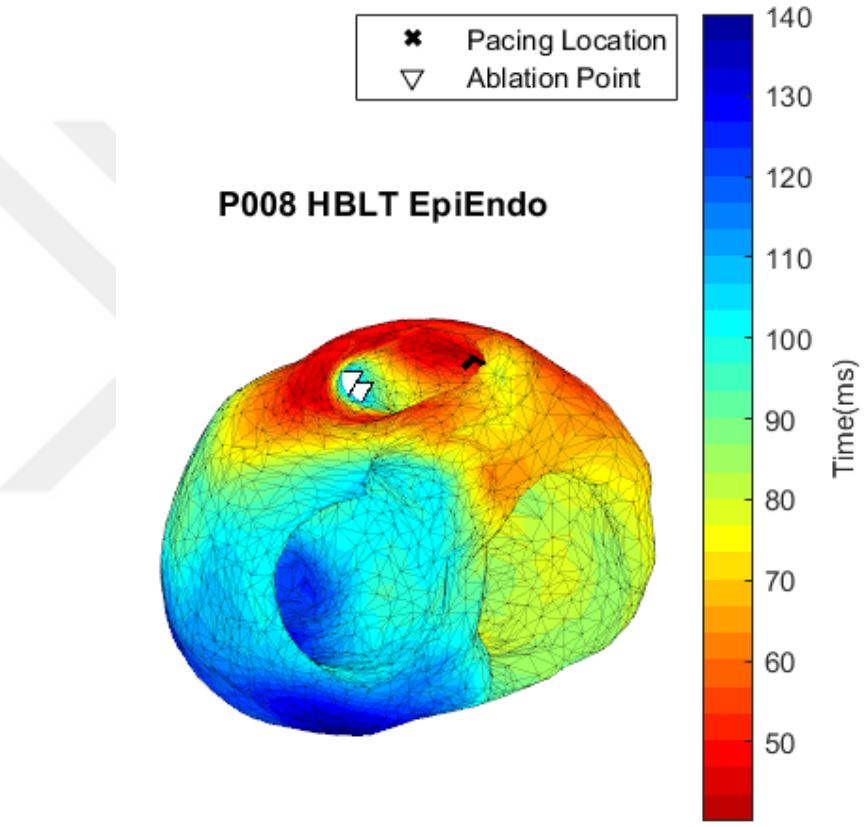


Figure 4.17: Spatiotemporal AT map for models with additional inhomogeneity of blood cavities of patients P008 (The left chamber seen in all three figures is the left ventricle and the chamber located at the right side of the figures is the right ventricle)

The identified source of PVC in P008 is slightly deviated, despite the activation sequences appearing to be correct. This discrepancy may be attributed to the use of a single point estimation method chosen in the study. Although the estimation of the origin of PVC in P002 is not entirely accurate, it has undergone a 5.3% improvement, see Table 4.4, resulting in a location that is much closer to the ablation point,

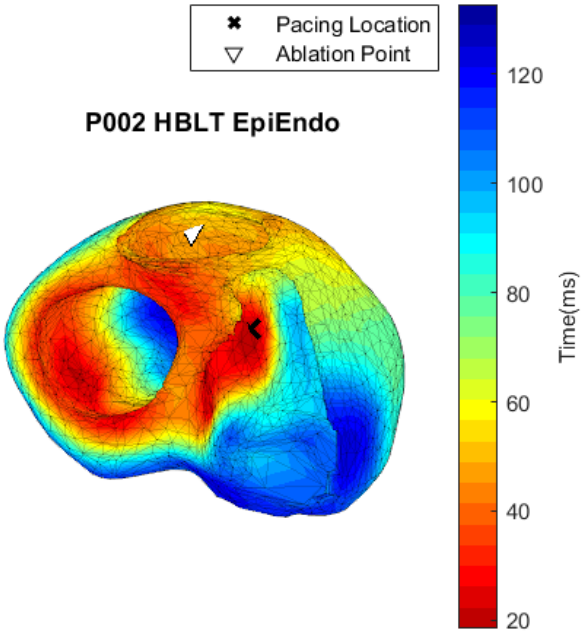


Figure 4.18: Spatiotemporal AT maps for models with additional inhomogeneity of blood cavities of patients P002 (The left chamber seen in all three figures is the left ventricle and the chamber located at the right side of the figures is the right ventricle)

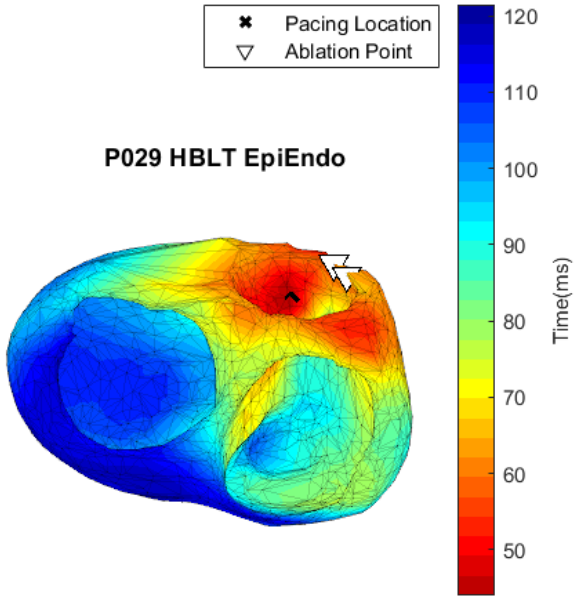


Figure 4.19: Spatiotemporal AT maps for models with additional inhomogeneity of blood cavities of patients P029 (The left chamber seen in all three figures is the left ventricle and the chamber located at the right side of the figures is the right ventricle)

illustrated in Fig. 4.18. Lastly, although the PVC origin of P029 for this model is almost the same as the ones found for both homogenous and inhomogeneous EpiEndo

models, a 9.2% improvement in the total mean LE of the patient is obtained, given in Table 4.4.

Table 4.4: The EpiEndo model with inhomogeneous blood cavity localization error, the total mean LE improvement percentage, and estimated PVC origin along the true origin side

| Patient # | HBLT EpiEndo | | | |
|---|---|---|---|---|
| | LE(mm) | improvement percentage | predicted side | ablation side |
| P008 | 28.6 | -15.6 | RV | RV |
| P002 | 40.6 | 5.3 | RV | RV |
| P029 | 19.2 | 9.2 | RV | RV |

# CHAPTER 5

# CONCLUSION AND FUTURE WORKS

In this study, the variation of spontaneous PVC localization based on various cardiac source and forward models have been examined on clinical data of 10 patients. The following methods are utilized for ECGI in this work:

- Tikhonov regularization for reconstruction of heart potentials
- Minimum derivative and spatiotemporal methods for estimation of activation time sequences.

The performance of the presented method are evaluated for the following five models:

- HT Epi: Homogeneous torso model with Epi geometry as the heart surface,
- HLT Epi: Inhomogeneous torso model with lungs and Epi geometry as the heart surface,
- HT EpiEndo: Homogeneous torso model with EpiEndo geometry as the heart surface,
- HLT EpiEndo: Inhomogeneous torso model with lungs and EpiEndo geometry as the heart surface,
- HBLT EpiEndo: Inhomogeneous torso model with lungs and blood cavities with EpiEndo geometry as the heart surface.

The evaluation of the forward matrices for all these models are not feasible as the true heart potentials are unknown. Therefore the results are evaluated in two ways: qual-

itatively based on the patient's profile, and quantitatively in relation to the ablation point positions identified by the physician. The results of the patients in three performance categories of good, bad, and inconsistent are presented based on the mean localization error value of all five models for each patient. Then, the performance comparison of potential and dipole based methods is discussed with respect to the PVC origin estimates.

Even though Tikhonov regularization generally resulted in smooth EGMs, the measurement artifacts and geometrical errors can cause the activation time calculation to be inaccurate for some nodes. Prefiltering the signals temporally improved the minimum derivative results and hence the spatiotemporal activation times to some extent, however, the final localization of PVC is still prone to AT performance. The spatiotemporal method smoothed the abrupt changes due to signal inaccuracies in LATs, resulting in more robust activation sequences.

The statistical information like mean and standard devations show the stability of the AT method employed across various models in the dataset. While there are some inconsistencies in the error values of individual patient models based on the median values, the median error values across all models are below 30 $mm$ for half of the patients and around 45 $mm$ for the other half. The IQR of each model reveals that the errors are not significantly distributed, indicating that the method is reliable and consistent with different models in the dataset.

Although the use of more complex models may present challenges in terms of computational complexity, it is demonstrated to yield improvements in the estimation of activation times for certain patients, thus resulting in a more precise localization of PVC. The spatiotemporal AT method produced stable results compared to minimum derivative method for both homogeneous and inhomogeneous models for each heart geometry. In some cases, EpiEndo models proved to result in a more precise PVC localization.

To sum up, this study investigates a novel spontaneous PVC dataset for PVC origin localization in human patients with the use of straighforward and computationally efficient Tikhonov and spatiotemporal regularization methods. The outcomes show the AT maps are often quite consistent in all five models, however, variations has

been observed in PVC origin estimates. Therefore, rather than relying on a single point PVC origin estimate, comparing potential and dipole based pacing locations these maps can guide the physicians for more accurate PVC localizations in ablation therapies.

## 5.1 Future Works

There are a lot of factors affecting the solution of this problem. Therefore, a wide range of studies can be done for improvement of performance. To mention a few, other regularization techniques can be investigated over this clinical data, other orders of Tikhonov regularization performance may be evaluated, optimization of the regularization parameter for spontaneous PVCs, and improvements in mathematical modelling of the heart and torso volume are among popular research topics which may be pursued.

In our future work, we aim to achieve a more robust AT estimation method to improve PVC localization performance by using Bayesian estimation and deep learning methods after doing data registration and creating a proper dataset for training.

# REFERENCES


[1] B. Akdemir, H. Yarmohammadi, M. C. Alraies, and W. O. Adkisson, Premature ventricular contractions: Reassure or refer?, Cleveland Clinic Journal of Medicine, 83(7), pp. 524–530, 2016, ISSN 0891-1150.

[2] ALIVECOR, What is an ecg?, https://www.alivecor.com/education/ecg.html, accessed on: 20.01.2023.

[3] K. Aras, W. Good, J. Tate, B. Burton, D. Brooks, J. Coll Font, O. Doessel, W. Schulze, D. Potyagaylo, L. Wang, P. van Dam, and R. MacLeod, Experimental data and geometric analysis repository—edgar, Journal of Electrocardiology, 48(6), pp. 975–981, 2015, ISSN 0022-0736.

[4] R. C. Barr, M. Ramsey, and M. S. Spach, Relating epicardial to body surface potential distributions by means of transfer coefficients based on geometry measurements, IEEE Transactions on Biomedical Engineering, BME-24(1), pp. 1–11, 1977.

[5] R. C. Barr and M. S. Spach, Inverse calculation of qrs-t epicardial potentials from body surface potential distributions for normal and ectopic beats in the intact dog., Circulation Research, 42(5), pp. 661–675, 1978.

[6] L. R. Bear, O. Bouhamama, M. Cluitmans, J. Duchateau, R. D. Walton, E. Abell, C. Belterman, M. Haissaguerre, O. Bernus, R. Coronel, and R. Dubois, Advantages and pitfalls of noninvasive electrocardiographic imaging, Journal of Electrocardiology, 57, pp. S15–S20, 2019, ISSN 0022-0736.

[7] L. R. Bear, L. K. Cheng, I. J. LeGrice, G. B. Sands, N. A. Lever, D. J. Paterson, and B. H. Smaill, Forward problem of electrocardiography: is it solved?, Circulation Arrhythmia and electrophysiology, 8(3), pp. 677—-684, 2015.

[8] J. G. Betts, *Anatomy & Physiology*, 2013, ISBN ISBN 978-1-938168-13-0.

[9] D. Calvetti, S. Morigi, L. Reichel, and F. Sgallari, Tikhonov regularization and the l-curve for large discrete ill-posed problems, Journal of Computational and Applied Mathematics, 123(1), pp. 423–446, 2000, ISSN 0377-0427, numerical Analysis 2000. Vol. III: Linear Algebra.

[10] B. S. Chandra, C. S. Sastry, L. Anumandla, and S. Jana, Dictionary-based monitoring of premature ventricular contractions: An ultra-low-cost point-of-care service, 2017.

[11] Cleveland-Clinic, Heart, https://my.clevelandclinic.org/health/body/21704-heart, accessed on: 20.01.2023.

[12] J. Coll Font, *Model based approaches to incorporate recordings of multiple heartbeats into the inverse problem of electrocardiography*, Ph.D. thesis, Northeastern University, 2016.

[13] P. Colli Franzone, L. F. Pavarino, and S. Scacchi, *Mathematical Cardiac Electrophysiology*, volume 13, Springer International Publishing, 2014, ISBN 978-3-319-04800-0.

[14] R. Drake, A. W. Vogl, and A. W. M. Mitchell, *Gray's Anatomy for Students*, Elsevier, Philadelphia, PA, 3 edition, 2014.

[15] B. Erem, J. Coll Font, R. M. Orellana, P. Št´ovíček, and D. H. Brooks, Using transmural regularization and dynamic modeling for noninvasive cardiac potential imaging of endocardial pacing with imprecise thoracic geometry, IEEE Transactions on Medical Imaging, 33(3), pp. 726–738, 2014.

[16] K. Farzam and J. Richards, *Premature Ventricular Contraction*, Treasure Island (FL): StatPearls Publishing, https://www.ncbi.nlm.nih.gov/books/NBK532991/, 2022.

[17] D. B. Geselowitz, Multipole representation for an equivalent cardiac generator, Proceedings of the IRE, 48, pp. 75–79, 1960.

[18] S. Ghosh, J. N. Avari, E. K. Rhee, P. K. Woodard, and Y. Rudy, Noninvasive electrocardiographic imaging (ecgi) of epicardial activation before and after catheter ablation of the accessory pathway in a patient with ebstein anomaly, Heart Rhythm, 5(6), pp. 857–860, 2008.

[19] M. S. GUILLEM, A. M. CLIMENT, J. MILLET, P. BERNE, R. RAMOS, J. BRUGADA, and R. BRUGADA, Spatiotemporal characteristics of qrs complexes enable the diagnosis of brugada syndrome regardless of the appearance of a type 1 ecg, Journal of Cardiovascular Electrophysiology, 27(5), pp. 563–570, 2016.

[20] R. Gulrajani, The forward and inverse problems of electrocardiography, IEEE Engineering in Medicine and Biology Magazine, 17(5), pp. 84–101, 1998.

[21] A. C. Guyton and J. E. Hall, *Textbook of medical physiology*, Saunders/Elsevier, 2011.

[22] M. Hanke, Conjugate gradient type methods for ill-posed problems, 1995.

[23] P. C. Hansen, Truncated singular value decomposition solutions to discrete ill-posed problems with ill-determined numerical rank, SIAM Journal on Scientific and Statistical Computing, 11(3), pp. 503–518, 1990.

[24] P. C. Hansen, Analysis of discrete ill-posed problems by means of the l-curve, SIAM Review, 34(4), pp. 561–580, 1992.

[25] K. He, J. Sun, Y. Wang, G. Zhong, and C. Yang, A novel model based on spatial and morphological domains to predict the origin of premature ventricular contraction, Frontiers in Physiology, 12, 2021, ISSN 1664-042X.

[26] I. Hernández-Romero, R. Molero, C. Fambuena-Santos, C. Herrero-Martín, A. M. Climent, and M. S. Guillem, Electrocardiographic imaging in the atria, Medical & Biological Engineering & Computing, 61(4), pp. 879–896, 2023, ISSN 1741-0444.

[27] B. HoráčekabJohn and J. C. Clements, The inverse problem of electrocardiography: A solution in terms of single- and double-layer sources on the epicardial surface, Mathematical Biosciences, 144(2), pp. 119–154, 1997, ISSN 0025-5564.

[28] A. Intini, R. N. Goldstein, P. Jia, C. Ramanathan, K. Ryu, B. Giannattasio, R. Gilkeson, B. S. Stambler, P. Brugada, W. G. Stevenson, Y. Rudy, and A. L. Waldo, Electrocardiographic imaging (ecgi), a novel diagnostic modality used for mapping of focal left ventricular tachycardia in a young athlete, Heart Rhythm, 2(11), pp. 1250–1252, 2005, ISSN 1547-5271.

[29] A. Intini, R. N. Goldstein, P. Jia, C. Ramanathan, K. Ryu, B. Giannattasio, R. Gilkeson, B. S. Stambler, P. Brugada, W. G. Stevenson, Y. Rudy, and A. L. Waldo, Electrocardiographic imaging (ecgi), a novel diagnostic modality used for mapping of focal left ventricular tachycardia in a young athlete, Heart rhythm, 2(11), p. 1250–1252, 2005.

[30] A. J. Graham, M. Orini, E. Zacur, G. Dhillon, H. Daw, N. T. Srinivasan, C. Martin, J. Lane, J. S. Mansell, A. Cambridge, J. Garcia, F. Pugliese, O. Segal, S. Ahsan, M. Lowe, M. Finlay, M. J. Earley, A. Chow, S. Sporton, M. Dhinoja, R. J. Hunter, R. J. Schilling, and P. D. Lambiase, Evaluation of ecg imaging to map hemodynamically stable and unstable ventricular arrhythmias, Circulation: Arrhythmia and Electrophysiology, 13(2), 2020.

[31] JohnHopkinsMedicine, Anatomy and function of the heart's electrical system, https://www.hopkinsmedicine.org/health/conditions-and-diseases/anatomy-and-function-of-the-hearts-electrical-system, accessed on: 01.11.2022.

[32] P. Johnston and R. Gulrajani, Selecting the corner in the l-curve approach to tikhonov regularization, IEEE Transactions on Biomedical Engineering, 47(9), pp. 1293–1296, 2000.

[33] J. Kadanec, J. Zelinka, G. Bukor, and M. Tysler, Procardio 8 - system for high resolution ecg mapping, in *Meas. 2017, Proc. 11th Int. Conf*, pp. 263–266, Smolenice, Slovakia, 2017.

[34] K. Lesina, T. Szili-Torok, E. Peters, A. de Wit, S. A. Wijchers, R. E. Bhagwandien, S.-C. Yap, A. Hirsch, and M. G. Hoogendijk, Performance and robustness testing of a non-invasive mapping system for ventricular arrhythmias, Frontiers in Physiology, 13, 2022, ISSN 1664-042X.

[35] J. Li, Detection of premature ventricular contractions using densely connected deep convolutional neural network with spatial pyramid pooling layer, CoRR, abs/1806.04564, 2018.

[36] P. W. Macfarlane, *Lead Systems*, Springer London, London, 2010, ISBN 978-1-84882-046-3.

[37] J. Malmivuo and R. Plonsey, *Bioelectromagnetism - Principles and Applications of Bioelectric and Biomagnetic Fields*, Oxford University Press, 1995.

[38] MayoClinic, Premature ventricular contractions (pvcs), https://www.mayoclinic.org/diseases-conditions/premature-ventricular-contractions/symptoms-causes/syc-20376757, accessed on: 01.11.2022.

[39] H. C. McGill, C. McMahan, and S. S. Gidding, Preventing heart disease in the 21st century: implications of the pathobiological determinants of atherosclerosis in youth (pday) study, Circulation, 117(9), pp. 1216–1227, 2008.

[40] C. G. Mohan and S. Devi, Forward problem in electrocardiogram: A review of certain approaches, pp. 21–24, 08 2013.

[41] G. Moody and R. Mark, The impact of the mit-bih arrhythmia database, IEEE Engineering in Medicine and Biology Magazine, 20(3), pp. 45–50, 2001.

[42] D. Nguyen, J. Jeudy, A. Jimenez Restrepo, and T. M. Dickfeld, A novel use of noninvasive registered electrocardiographic imaging map for localization of vt and pvc, JACC: Case Reports, 3(4), pp. 591–593, 2021, ISSN 2666-0849.

[43] M. J. O'Donnell, S. L. Chin, S. Rangarajan, D. Xavier, L. Liu, H. Zhang, P. Rao-Melacini, X. Zhang, P. Pais, S. Agapay, P. Lopez-Jaramillo, A. Damasceno, P. Langhorne, M. J. McQueen, A. Rosengren, M. Dehghan, G. J. Hankey, A. L. Dans, A. Elsayed, A. Avezum, C. Mondo, H.-C. Diener, D. Ryglewicz, A. Czlonkowska, N. Pogosova, C. Weimar, R. Iqbal, R. Diaz, K. Yusoff, A. Yusufali, A. Oguz, X. Wang, E. Penaherrera, F. Lanas, O. S. Ogah, A. Ogunniyi, H. K. Iversen, G. Malaga, Z. Rumboldt, S. Oveisgharan, F. Al Hussain, D. Magazi, Y. Nilanont, J. Ferguson, G. Pare, and S. Yusuf, Global and regional effects of potentially modifiable risk factors associated with acute stroke in 32 countries (interstroke): a case-control study, The Lancet, 388(10046), pp. 761–775, 2016, ISSN 0140-6736.

[44] Y. Park, L. Reichel, G. Rodriguez, and X. Yu, Parameter determination for tikhonov regularization problems in general form, Journal of Computational and Applied Mathematics, 343, pp. 12–25, 2018, ISSN 0377-0427.

[45] C. Penney, J. Clements, M. Gardner, L. Sterns, and B. Horácek, The inverse problem of electrocardiography: Appli- ˇ cation to localization of wolff-parkinson-white pre-excitation sites, in *IEEE Engineering in Medicine and Biology Society 17th Annual International Conference*, pp. 215–216, IEEE Press, New York, 1995.

[46] A. J. Pullan, L. K. Cheng, M. P. Nash, A. Ghodrati, R. MacLeod, and D. H. Brooks, *The Inverse Problem of Electrocardiography*, pp. 299–344, Springer London, London, 2010, ISBN 978-1-84882-046-3.

[47] C. Ramanathan, P. Jia, R. Ghanem, D. Calvetti, and Y. Rudy, Noninvasive electrocardiographic imaging (ecgi): Application of the generalized minimal residual (gmres) method, Annals of biomedical engineering, 31(8), p. 981–994, 2003.

[48] C. Ramanathan, P. Jia, R. N. Ghanem, K. Ryu, and Y. Rudy, Activation and repolarization of the normal human heart under complete physiological conditions., Proceedings of the National Academy of Sciences of the United States of America, 103 16, pp. 6309–14, 2006.

[49] N. Rasoolzadeh, J. Svehlikova, B. Ondrusova, and Y. S. Dogrusoz, Variability of premature ventricular contraction localization with respect to source and forward model variation in clinical data, in *Proceedings of the Computing in Cardiology Conference*, Tampere, Finland, 2022.

[50] R. Rehman, V. Yelamanchili, and A. Makaryus, *Cardiac Imaging*, Treasure Island (FL): StatPearls Publishing, 2022.

[51] P. Robert, Limitations on the equivalent cardiac generator, Biophysical Journal, 6(2), pp. 163–173, 1966, ISSN 0006-3495.

[52] M. Schaufelberger, S. Schuler, L. Bear, M. Cluitmans, J. Coll Font, O. N. Onak, O. Dossel, and D. Brooks, Comparison of activation times estimation for potential-based ecg imaging, Computing in cardiology, 46, p. 10.22489/cinc.2019.379, 2019.

[53] W. H. W. Schulze, D. Potyagaylo, R. Schimpf, T. Papavassiliu, E. Tülümen, B. Rudic, V. Liebe, C. Doesch, J. Traechtler, M. Borggrefe, and O. Dössel, A simulation dataset for ecg imaging of paced beats with models for transmural, endo-and epicardial and pericardial source imaging, 03 2015.

[54] A. J. Shah, M. Hocini, O. Xhaet, P. Pascale, L. Roten, S. B. Wilton, N. Linton, D. Scherr, S. Miyazaki, A. S. Jadidi, X. Liu, A. Forclaz, I. Nault, L. Rivard, M. E. Pedersen, N. Derval, F. Sacher, S. Knecht, P. Jais, R. Dubois, S. Eliautou, R. Bokan, M. Strom, C. Ramanathan, C. Ivan, J. Sahadevan, B. Lindsay, A. L. Waldo, and M. Haissaguerre, Validation of novel 3-dimensional electrocardiographic mapping of atrial tachycardias by invasive mapping and ablation: A

multicenter study, Journal of the American College of Cardiology, 62(10), pp. 889–897, 2013, ISSN 0735-1097.

[55] E. Simonson, O. H. Schmitt, R. B. Levine, and J. Dahl, Electrocardiographic mirror pattern studies. iii, American Heart Journal, 45(5), pp. 655–664, 1953, ISSN 0002-8703.

[56] J. Svehlikova, M. Teplan, and M. Tysler, Geometrical constraint of sources in noninvasive localization of premature ventricular contractions, Journal of Electrocardiology, 51(3), pp. 370–377, 2018, ISSN 0022-0736.

[57] J. Svehlikova, J. Zelinka, Y. S. Dogrusoz, W. Goood, M. Tysler, and L. Bear, "impact of signal preprocessing on the inverse localization of the origin of ventricular pacing, in *Computing in Cardiology. 45*, pp. 3–6, 2018.

[58] L. Sörnmo and P. Laguna, Chapter 6 - the electrocardiogram—a brief background, in L. Sörnmo and P. Laguna, editors, *Bioelectrical Signal Processing in Cardiac and Neurological Applications*, Biomedical Engineering, pp. 411–452, Academic Press, Burlington, 2005, ISBN 978-0-12-437552-9.

[59] A. N. Tikhonov and V. Y. Arsenin, *Solutions of ill-posed problems*, V. H. Winston & Sons, Washington, D.C.: John Wiley & Sons, New York, 1977, translated from the Russian, Preface by translation editor Fritz John, Scripta Series in Mathematics.

[60] G. J. Tortora and M. T. Nielsen, *Principles of Human Anatomy*, Nielsen, 11th edition, 2009.

[61] A. Ullah, S. M. Anwar, M. Bilal, and R. M. Mehmood, Classification of arrhythmia by using deep learning with 2-d ECG spectral image representation, Remote Sensing, 12(10), p. 1685, may 2020.

[62] P. M. van Dam, R. Tung, K. Shivkumar, and M. Laks, Quantitative localization of premature ventricular contractions using myocardial activation ecgi from the standard 12-lead electrocardiogram, Journal of Electrocardiology, 46(6), pp. 574–579, 2013, ISSN 0022-0736.

[63] I. Vogiatzis, E. Koulouris, A. Ioannidis, E. Sdogkos, M. Pliatsika, P. Roditis, and M. Goumenakis, The importance of the 15-lead versus 12-lead ecg recordings in the diagnosis and treatment of right ventricle and left ventricle posterior and lateral wall acute myocardial infarctions, Acta Informatica Medica, 27, p. 35, 03 2019.

[64] G. M. Wahler, Chapter 43 - cardiac action potentials, in N. Sperelakis, editor, *Cell Physiology Source Book (Fourth Edition)*, pp. 757–769, Academic Press, San Diego, fourth edition edition, 2012, ISBN 978-0-12-387738-3.

[65] Y. Wang, P. S. Cuculich, J. Zhang, K. A. Desouza, R. Vijayakumar, J. Chen, M. N. Faddis, B. D. Lindsay, T. W. Smith, and Y. Rudy, Noninvasive electroanatomic mapping of human ventricular arrhythmias with electrocardiographic imaging, Science translational medicine, 3(98).

[66] WHO, Cardiovascular diseases(cvds), https://www.who.int/en/news-room/fact-sheets/detail/cardiovascular-diseases-(cvds), accessed on: 20.01.2023.

[67] T. Yamada, Twelve-lead electrocardiographic localization of idiopathic premature ventricular contraction origins, Journal of Cardiovascular Electrophysiology, 30(11), pp. 2603–2617, 2019.

[68] F. G. Yanowitz, The standard 12 lead ecg, https://ecg.utah.edu/lesson/1, accessed on: 20.01.2023.

[69] J. Zhang, X. Zhang, L. Jiao, O.-C. Granmo, Y. Qian, and F. Pan, Interpretable tsetlin machine-based premature ventricular contraction identification, 2023.

[70] S. Zhou, J. L. Sapp, P. Šťovíček, and B. M. Horáček, Localization of activation origin on patient-specific endocardial surface by the equivalent double layer (edl) source model with sparse bayesian learning, IEEE Transactions on Biomedical Engineering, 66(8), pp. 2287–2295, 2019.

[71] X. Zhou, L. Fang, Z. Wang, H. Liu, and W. Mao, Comparative analysis of electrocardiographic imaging and ecg in predicting the origin of outflow tract ventricular arrhythmias, Journal of International Medical Research, 48(3), p. 0300060520913132, 2020, pMID: 32228331.

# APPENDIX A

# DIPOLE-BASED PROBLEM

## A.1 Problem Definition

For a dipole in each specific point position BSPs are computed by the linear equation:

$$\mathbf{y}(k) = \mathbf{T}\mathbf{d}_i(k),\ k = 1, 2, \ldots, K, \tag{A.1}$$

where $\mathbf{T}$ is a transfer matrix computed by a boundary element method for a torso model, describing the relation between the dipole $\mathbf{d}_i(k)$ at time instant $k$ in the given position $i$, and $\mathbf{y}(k)$, the potentials at the same time instant on the torso. Then, for the unknown dipole moments, equation (A.1) leads to:

$$\hat{\mathbf{d}}_i(k) = \mathbf{T}^{\dagger}\mathbf{y}(k). \tag{A.2}$$

where $\mathbf{T}^{\dagger}$ is the pseudo-inverse of matrix $\mathbf{T}$, and (A.2) has a unique solution fulfilling the criterion of the minimal least-squares method.

## A.2 Dipole-Based Method

This method has been employed by our project partners in IMS-SAS. However, as a comparison between the results, it has been mentioned. A brief overview of the method will be provided below.

Given that the activated area during the initial 20-30 ms of the PVC interval is limited in scope, it can be approximated by a single dipole. Utilizing this assumption, the PVC origin can be computed by considering every point on the triangulated surface of the ventricles, both on the epicardium and epicardium-endocardium [56].

In each time step for the beginning 20-30 $ms$ of activation, the result of Equation A.1 is computed for each assumed position of the dipole on the ventricular surface. Possible positions of the PVC origin are defined on the whole surface or volume of the heart model ($i = 1, 2, \ldots, N$, where $N$ is the number of nodes/possible dipole locations on the heart). Then the inverse solution is computed for each predefined position $i$ and each time step $k$ starting from the beginning time interval. The quality of each result is evaluated by relative residual error (RRE) between the input measured map $\mathbf{y}(k)$ and the map $\mathbf{y}^i_{comp}(k)$ computed using the resulting dipole as:

$$\mathbf{RRE}^i(k) = \frac{\|\mathbf{y}(k) - \mathbf{y}^i_{comp}(k)\|}{\|\mathbf{y}(k)\|}. \tag{A.3}$$

where $\mathbf{y}^i_{comp}(k) = \mathbf{T}\hat{\mathbf{d}}_i(k)$, and $\|.\|$ means the Euclidean norm. Then the position $i$ of the dipole with the minimal $\mathbf{RRE}^i(k)$ value out of all time steps and all positions on the ventricles is considered as the location of the PVC origin.

# APPENDIX B

# PATIENT RESULTS

## B.1 Reconstructed Heart Potentials

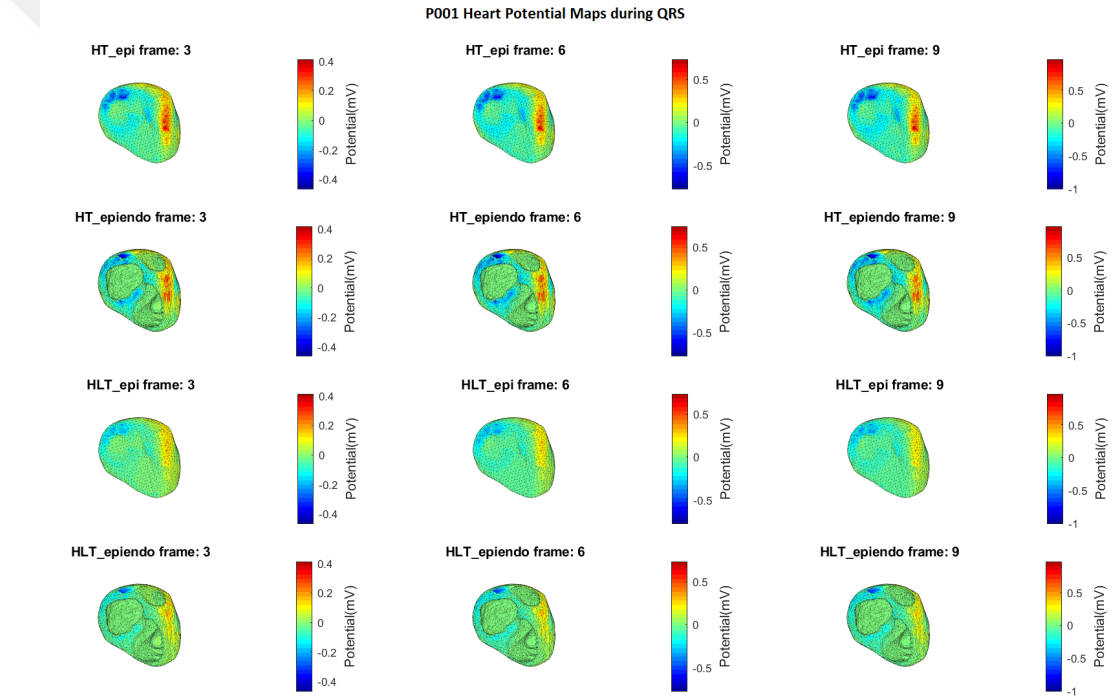


Figure B.1: Heart potential distribution of patient P001 during QRS

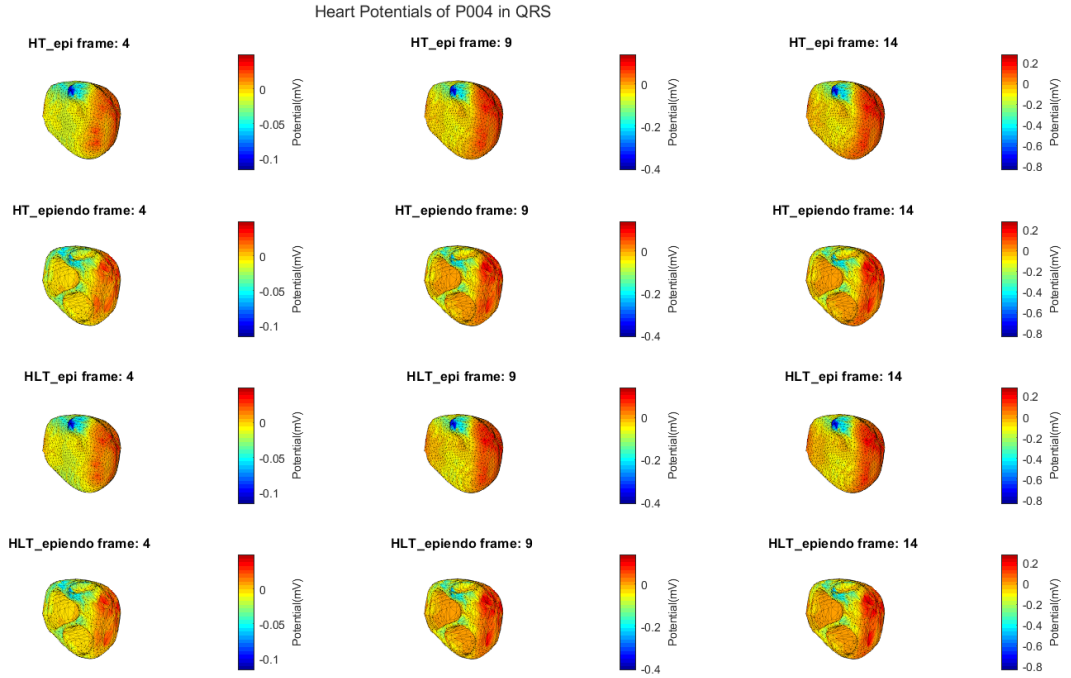


Figure B.2: Heart potential distribution of patient P004 during QRS

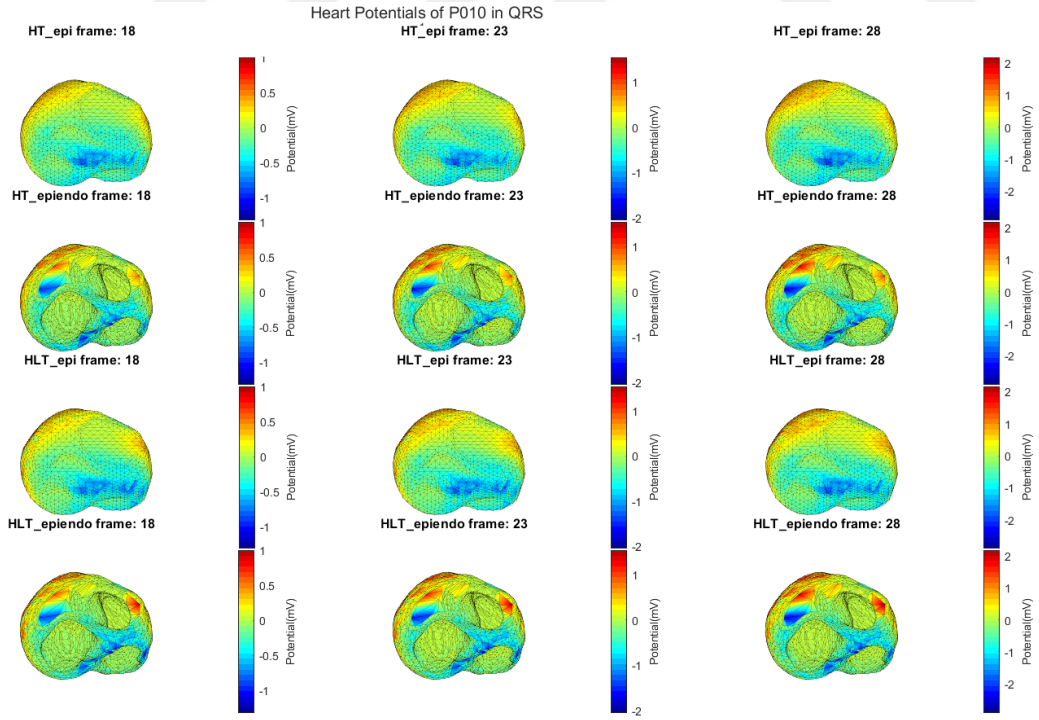


Figure B.3: Heart potential distribution of patient P010 during QRS

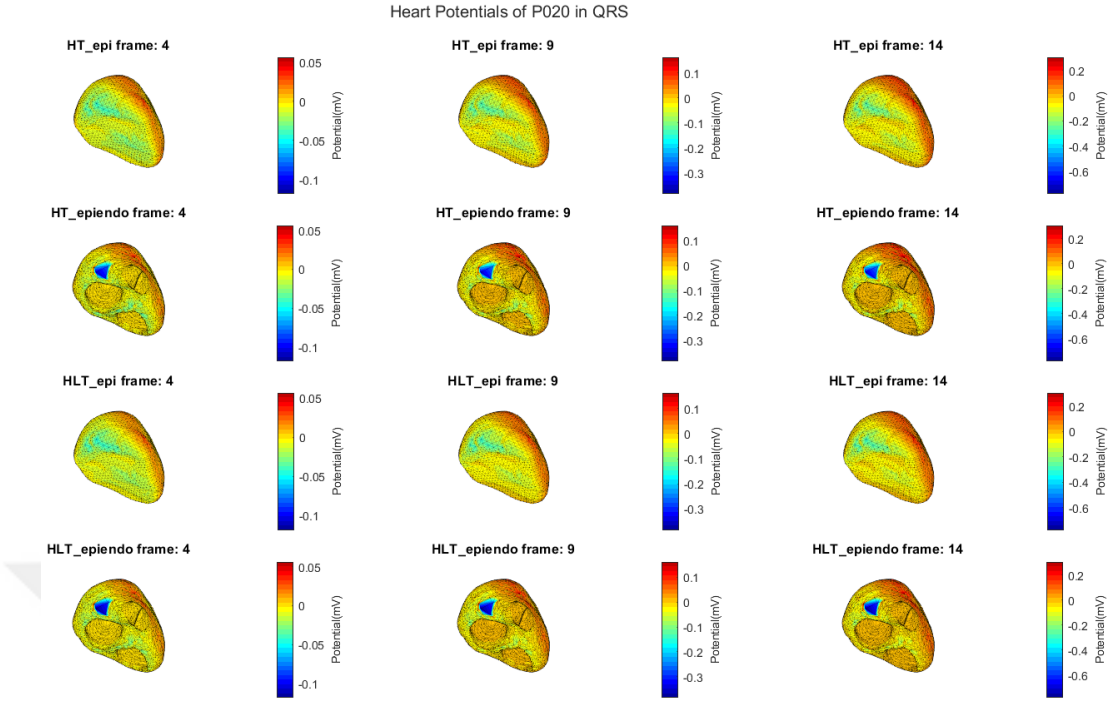


Figure B.4: Heart potential distribution of patient P020 during QRS

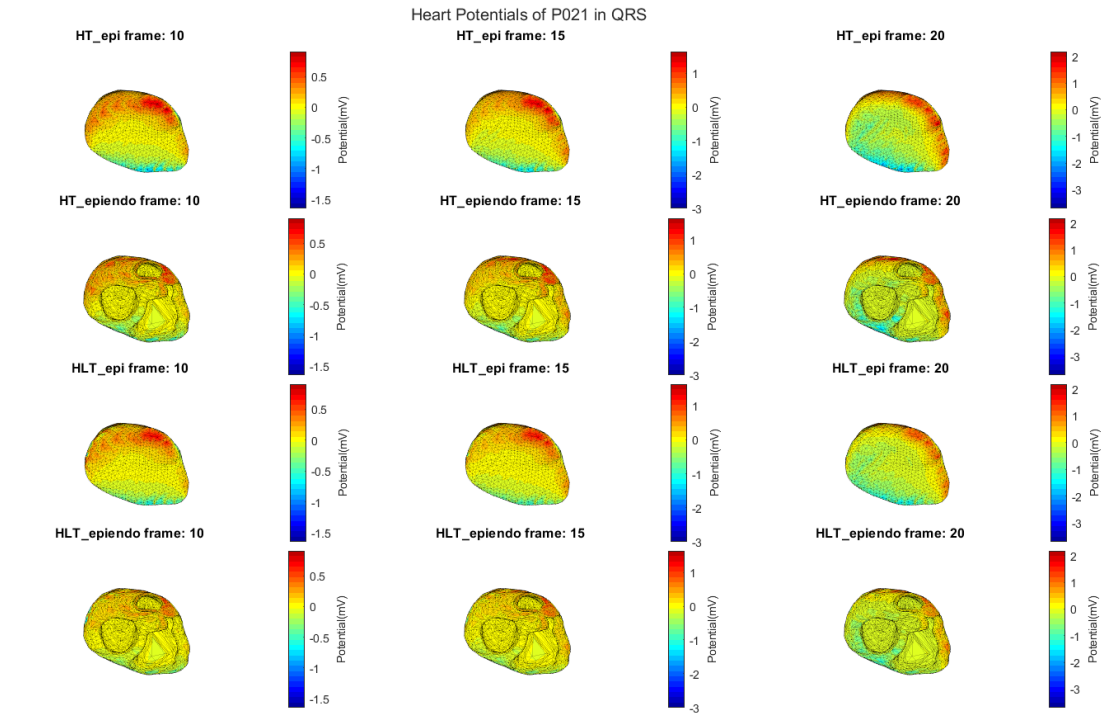


Figure B.5: Heart potential distribution of patient P021 during QRS

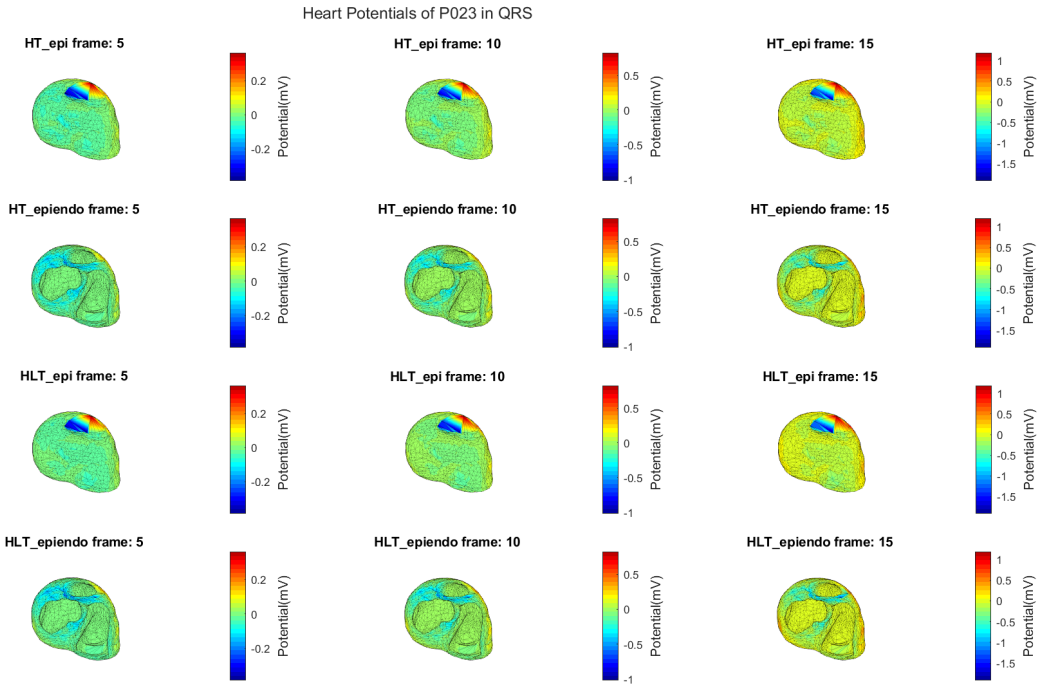


Figure B.6: Heart potential distribution of patient P023 during QRS

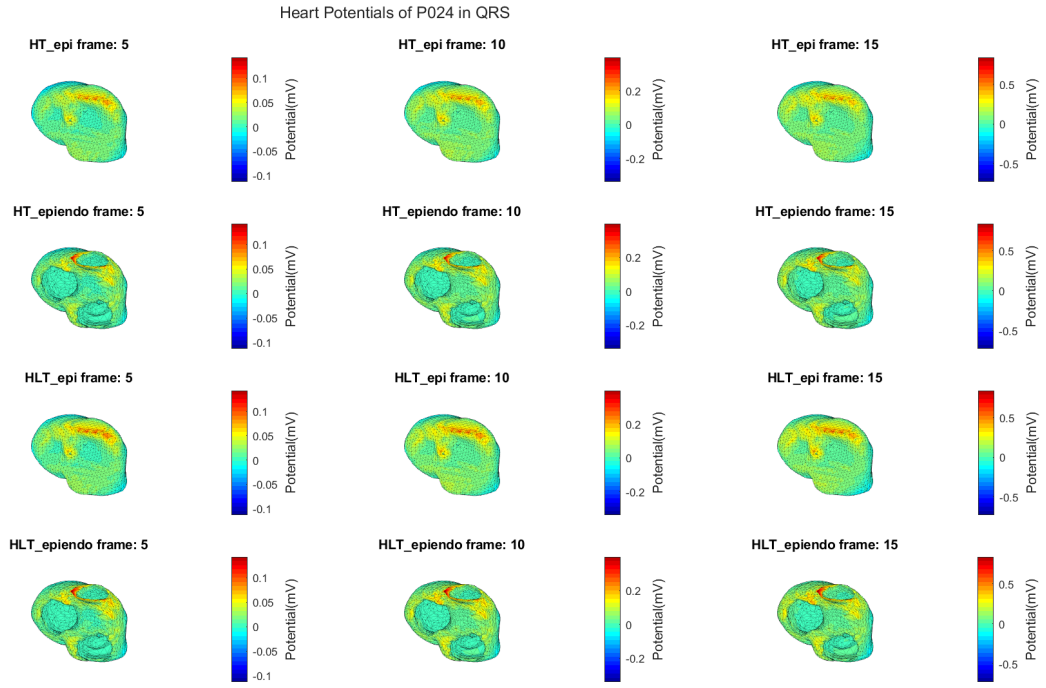


Figure B.7: Heart potential distribution of patient P024 during QRS

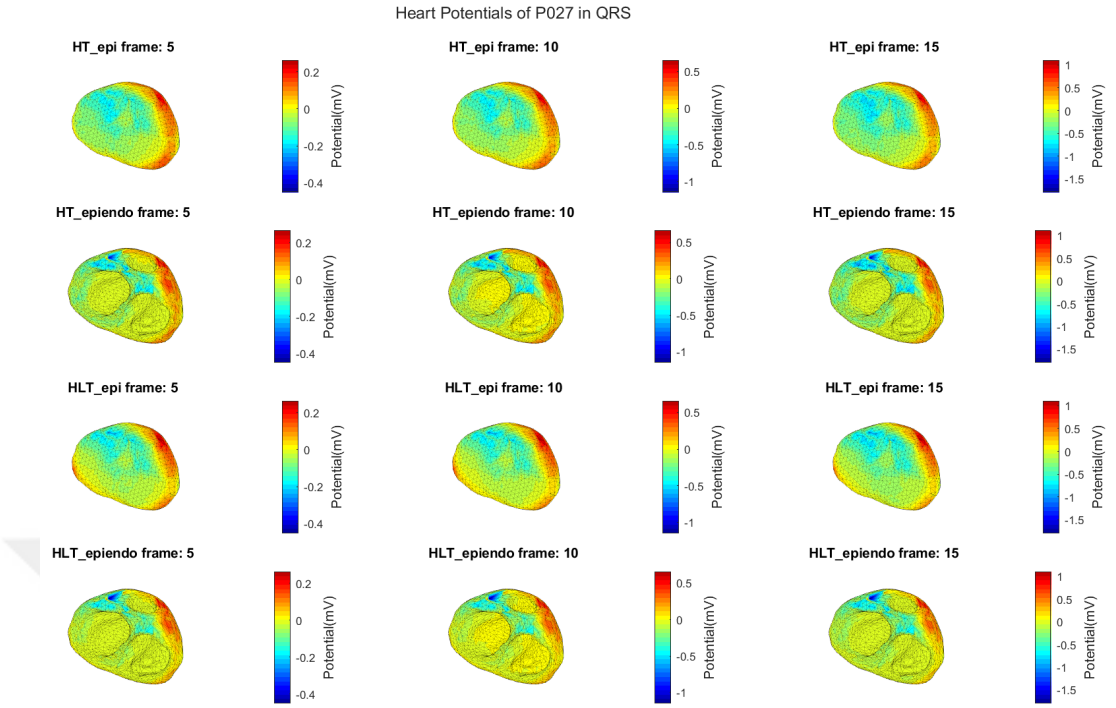


Figure B.8: Heart potential distribution of patient P027 during QRS

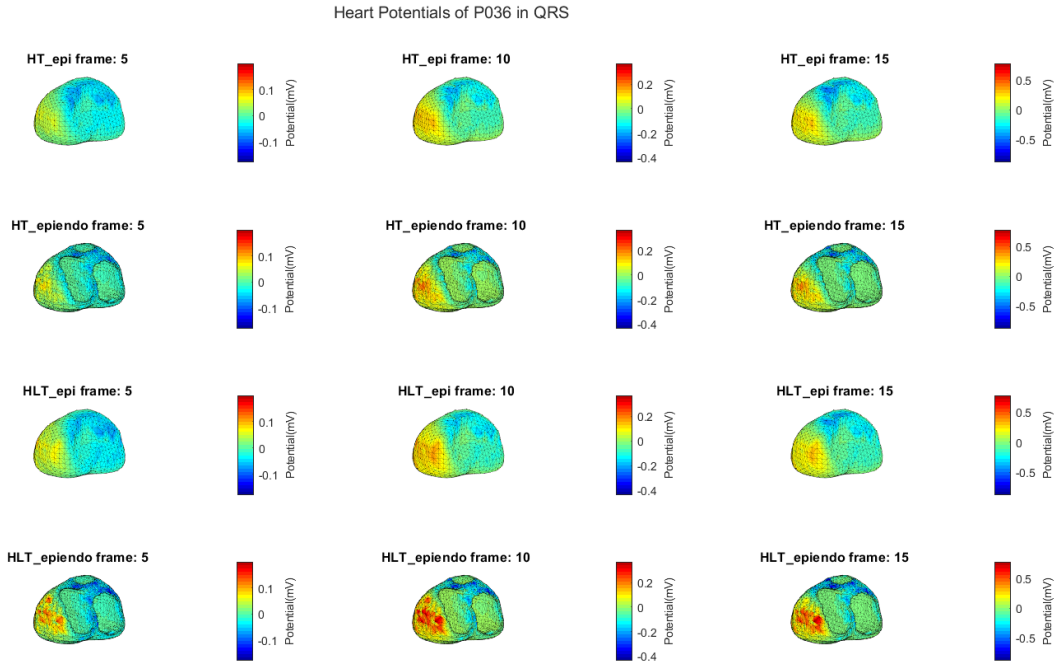


Figure B.9: Heart potential distribution of patient P036 during QRS

## B.2 Potential-Based AT Maps

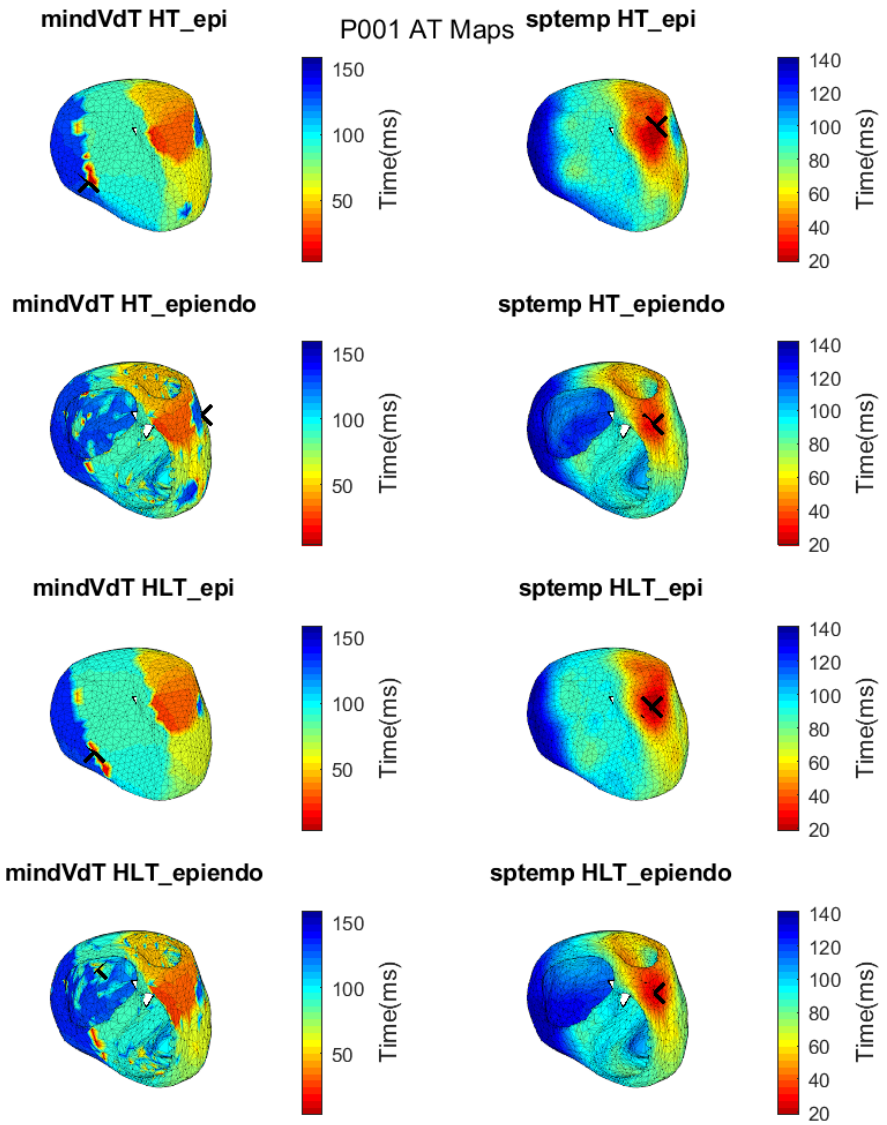


Figure B.10: Minimum derivative based vs spatiotemporal AT maps of P001 with the cross showing the estimated PVC origin and white triangle representing ablation point(s)

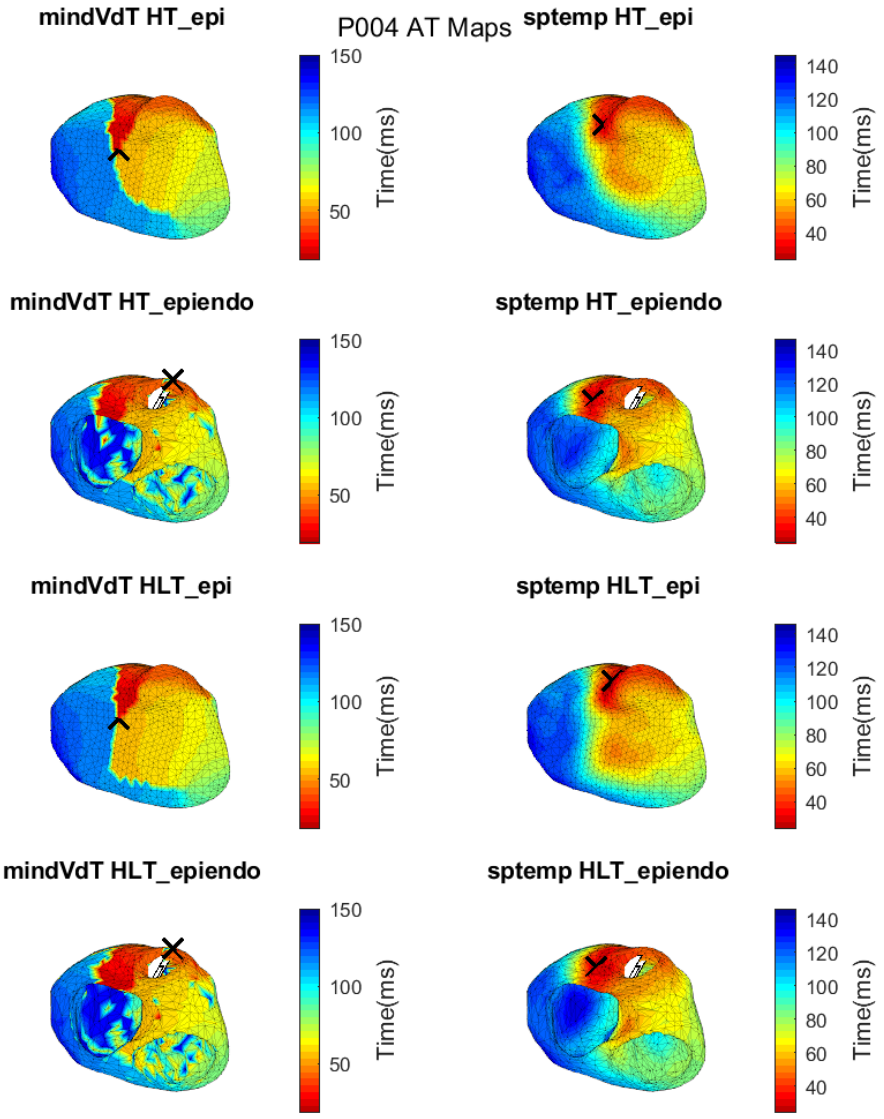


Figure B.11: Minimum derivative based vs spatiotemporal AT maps of P004 with the cross showing the estimated PVC origin and white triangle representing ablation point(s)

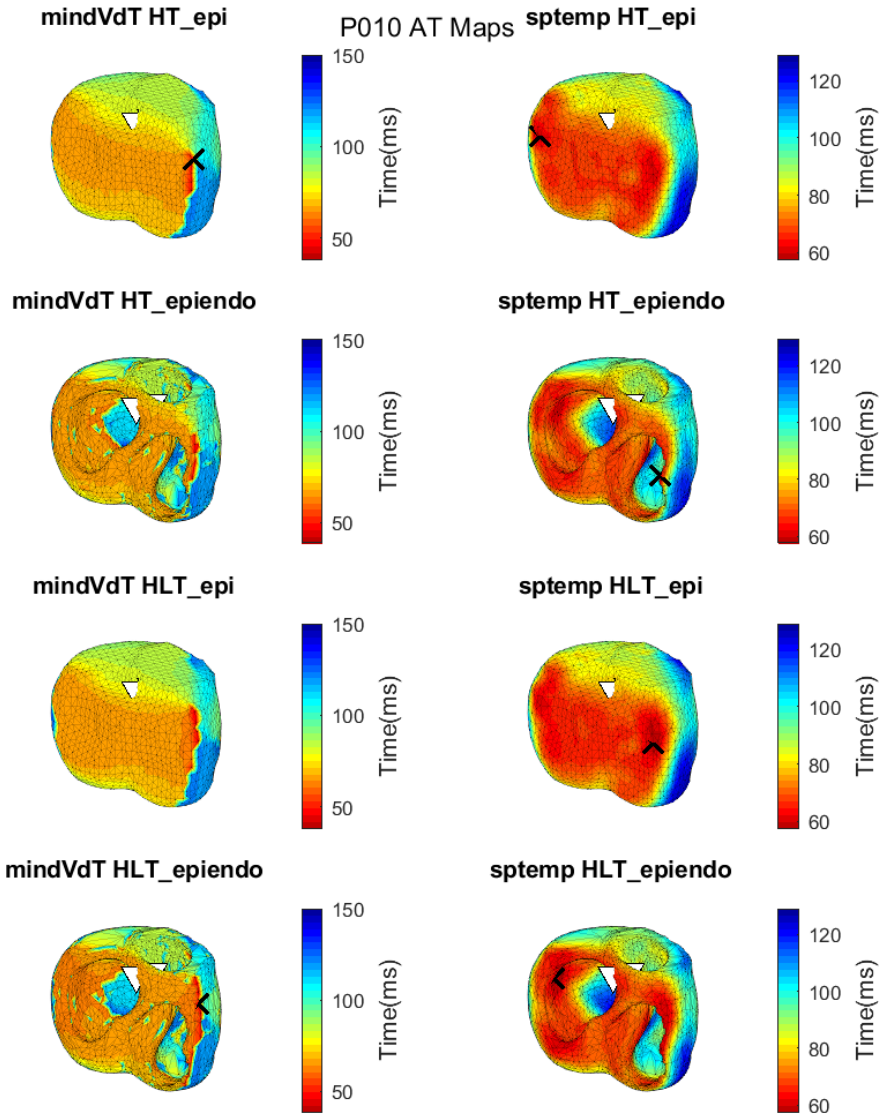


Figure B.12: Minimum derivative based vs spatiotemporal AT maps of P010 with the cross showing the estimated PVC origin and white triangle representing ablation point(s)

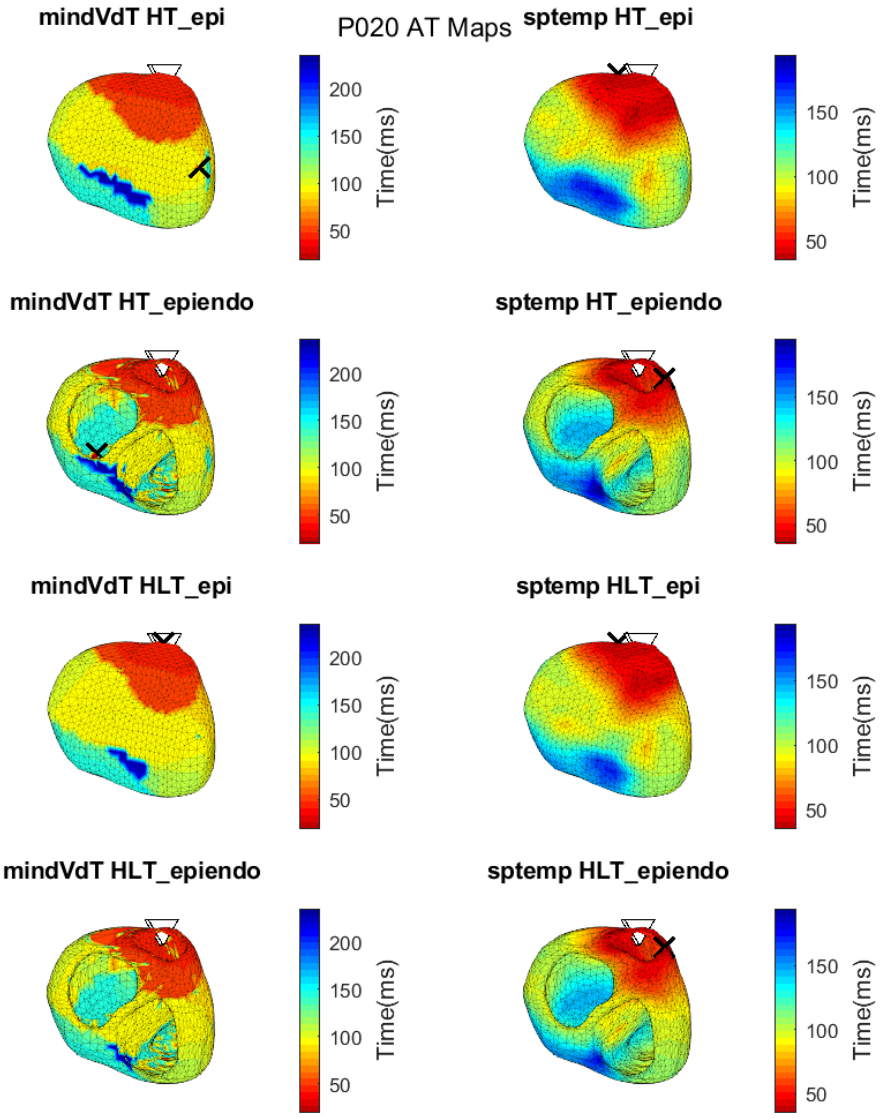


Figure B.13: Minimum derivative based vs spatiotemporal AT maps of P020 with the cross showing the estimated PVC origin and white triangle representing ablation point(s)

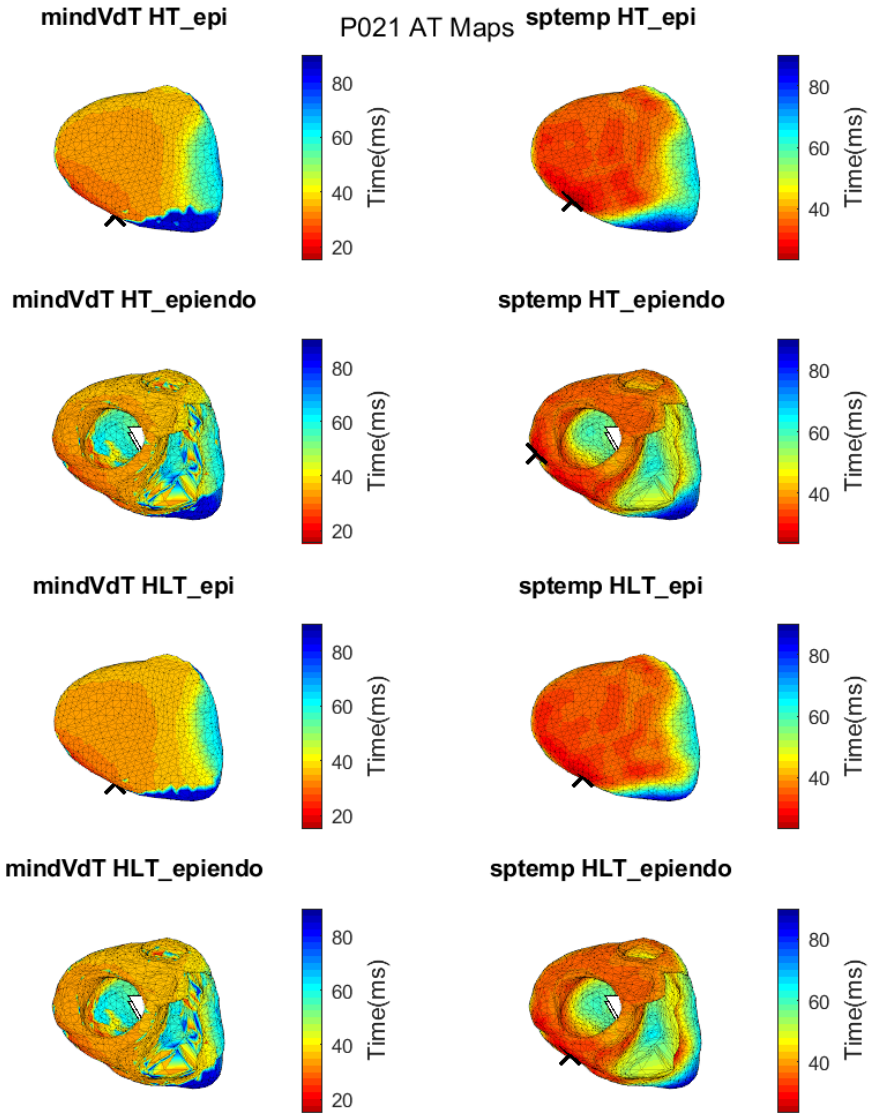


Figure B.14: Minimum derivative based vs spatiotemporal AT maps of P021 with the cross showing the estimated PVC origin and white triangle representing ablation point(s)

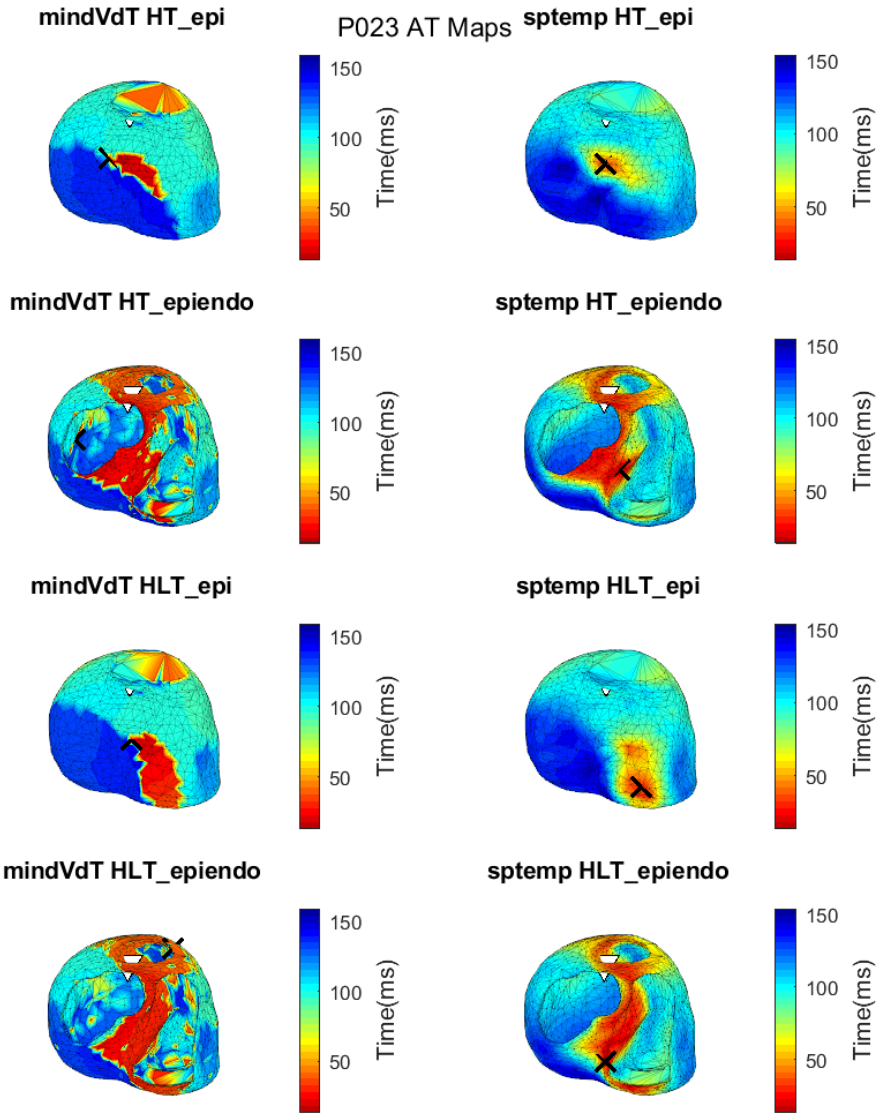


Figure B.15: Minimum derivative based vs spatiotemporal AT maps of P023 with the cross showing the estimated PVC origin and white triangle representing ablation point(s)

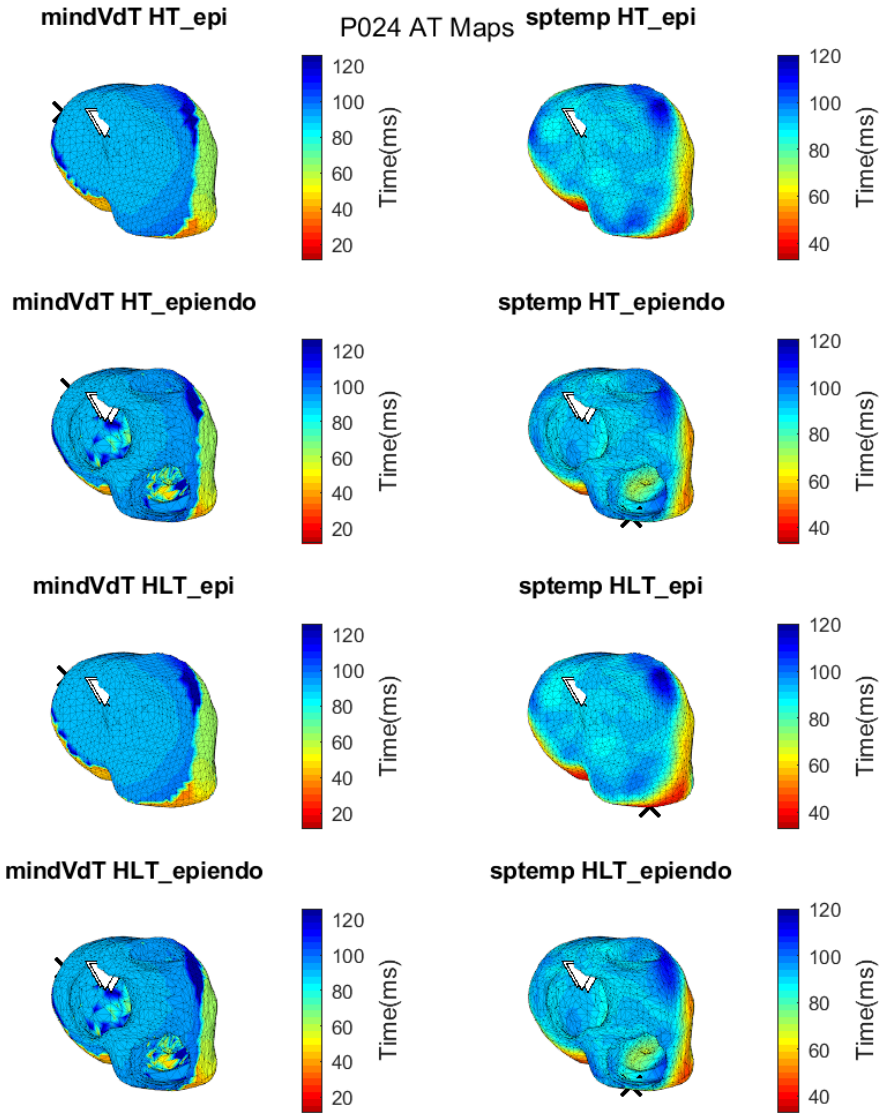


Figure B.16: Minimum derivative based vs spatiotemporal AT maps of P024 with the cross showing the estimated PVC origin and white triangle representing ablation point(s)

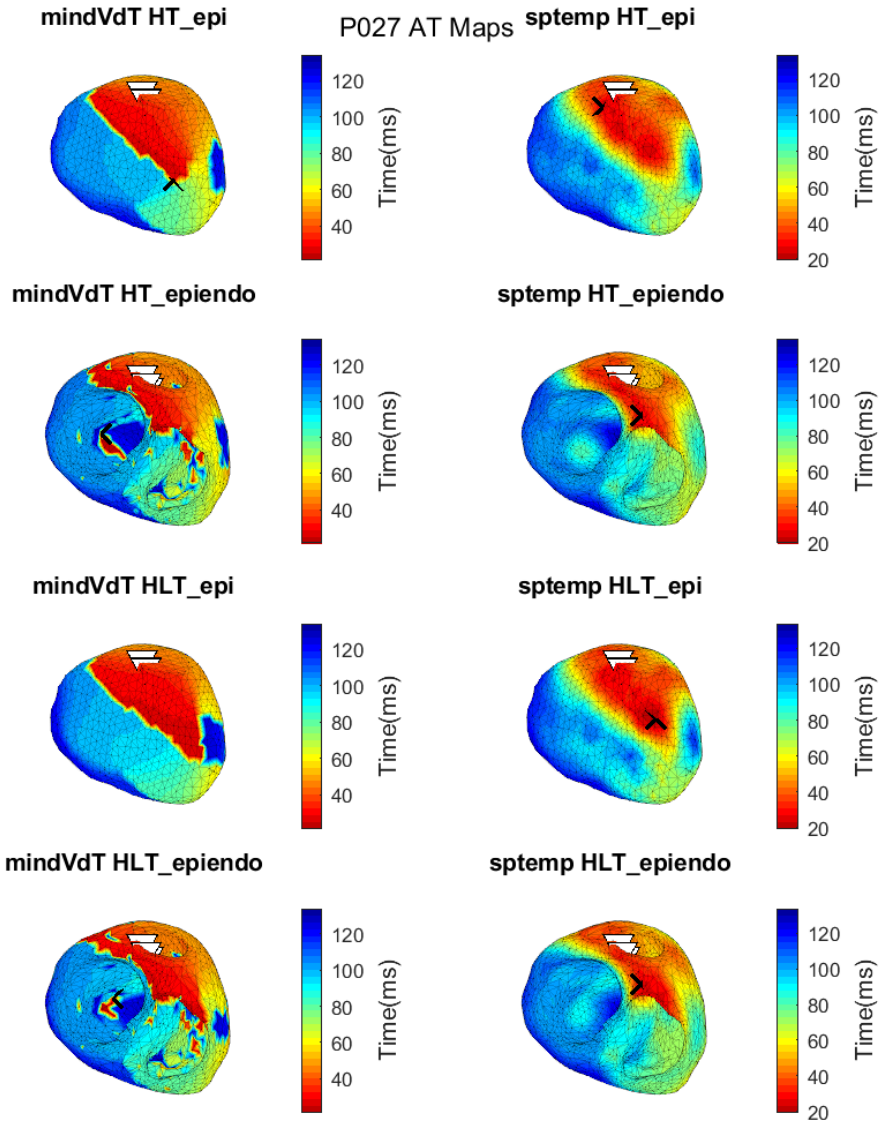


Figure B.17: Minimum derivative based vs spatiotemporal AT maps of P027 with the cross showing the estimated PVC origin and white triangle representing ablation point(s)

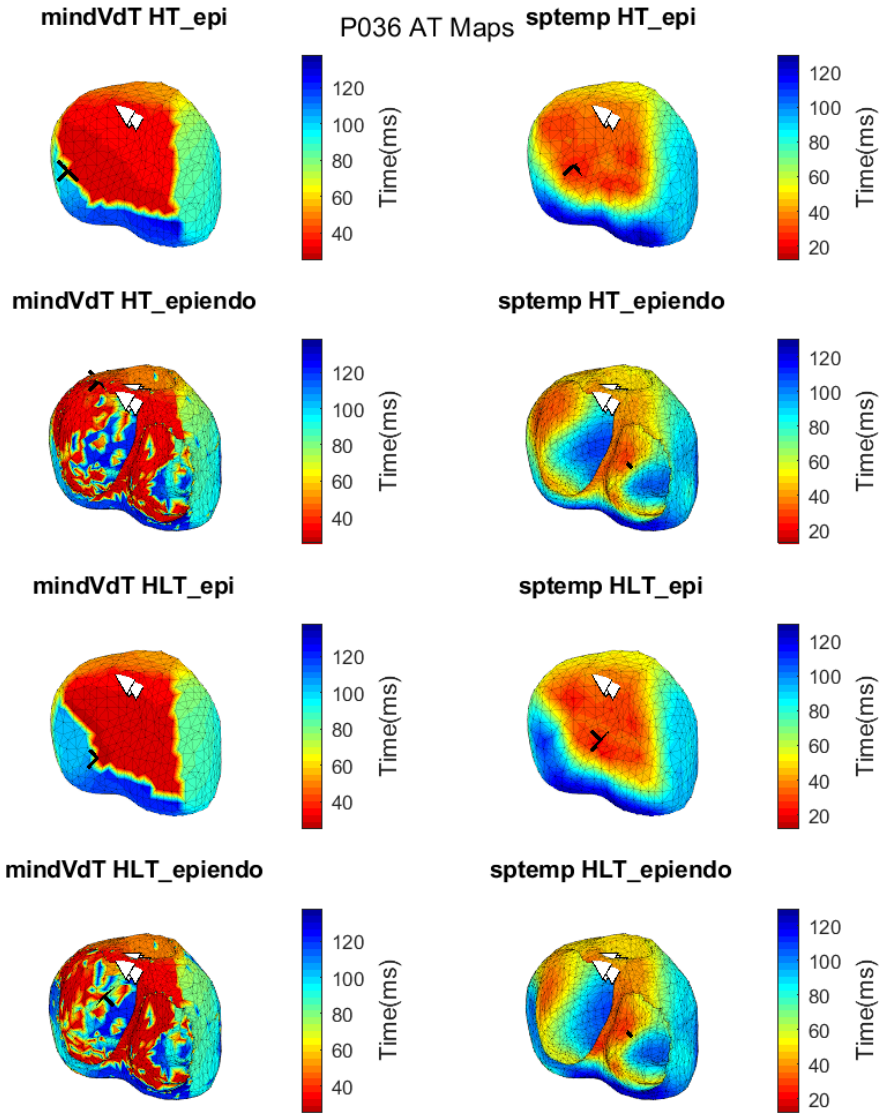


Figure B.18: Minimum derivative based vs spatiotemporal AT maps of P036 with the cross showing the estimated PVC origin and white triangle representing ablation point(s)

## B.3 Spatiotemporal AT Maps

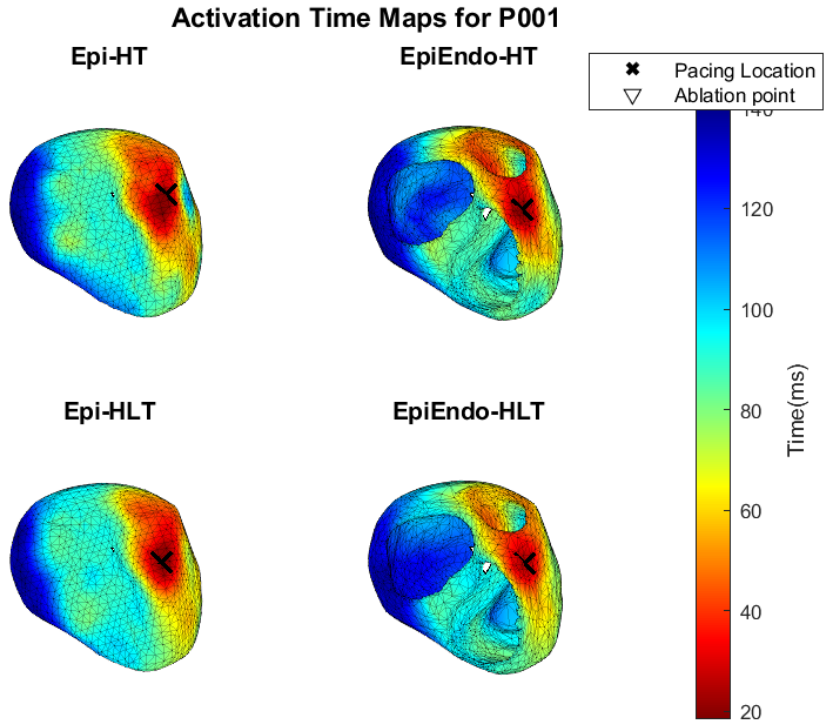


Figure B.19: Spatiotemporal AT maps of P001 with pacing locations

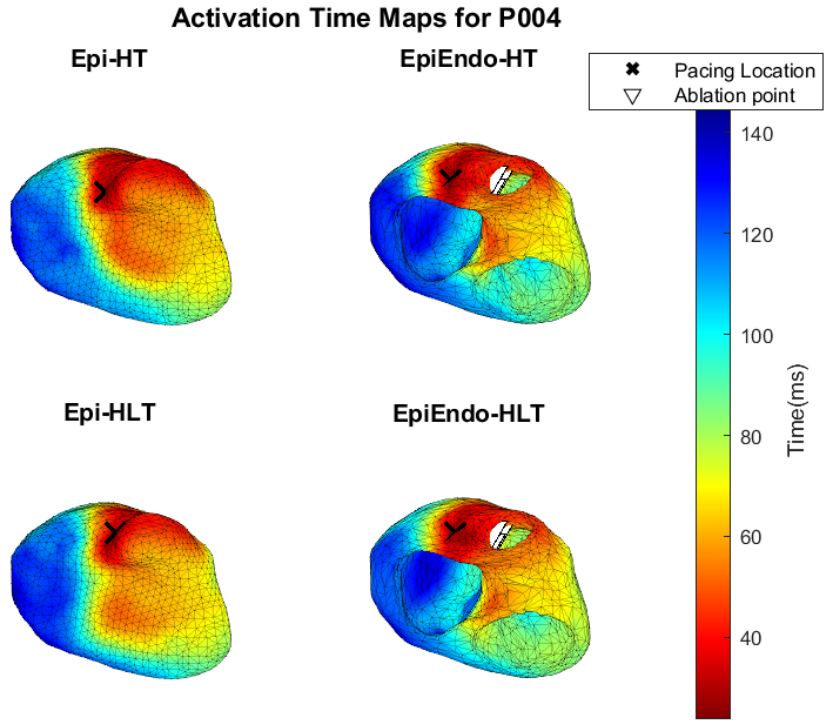


Figure B.20: Spatiotemporal AT maps of P004 with pacing locations

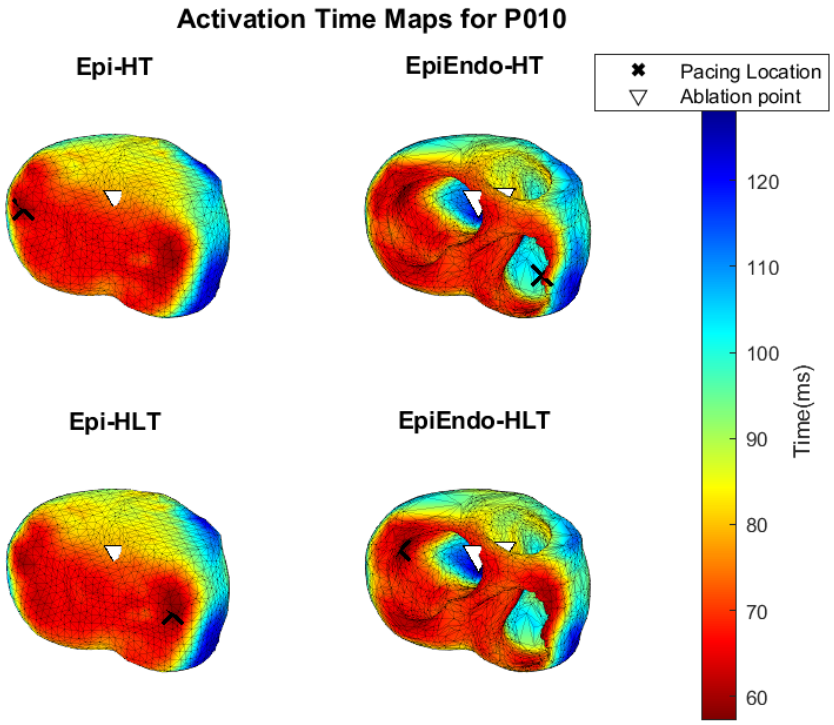


Figure B.21: Spatiotemporal AT maps of P010 with pacing locations

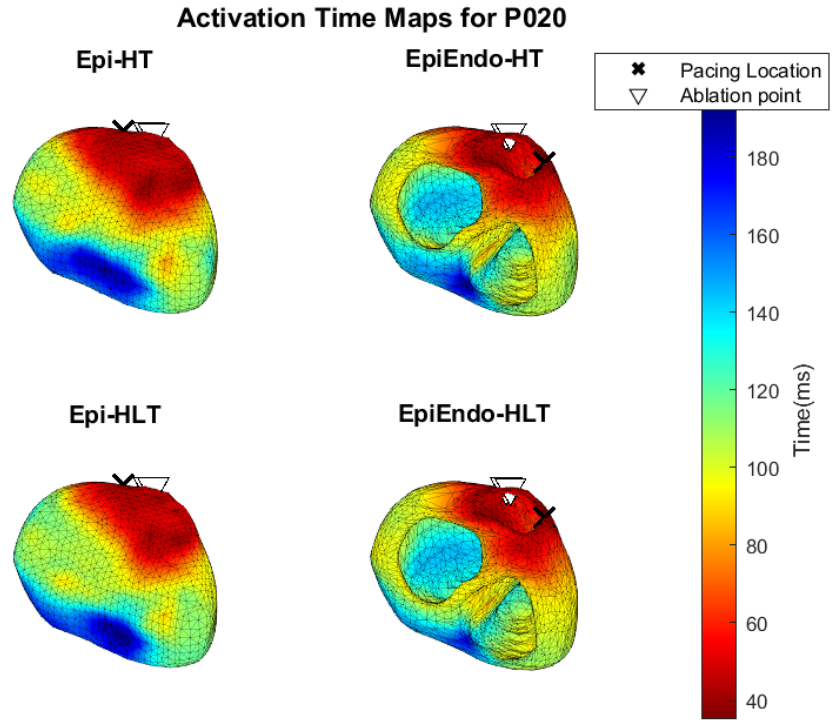


Figure B.22: Spatiotemporal AT maps of P020 with pacing locations

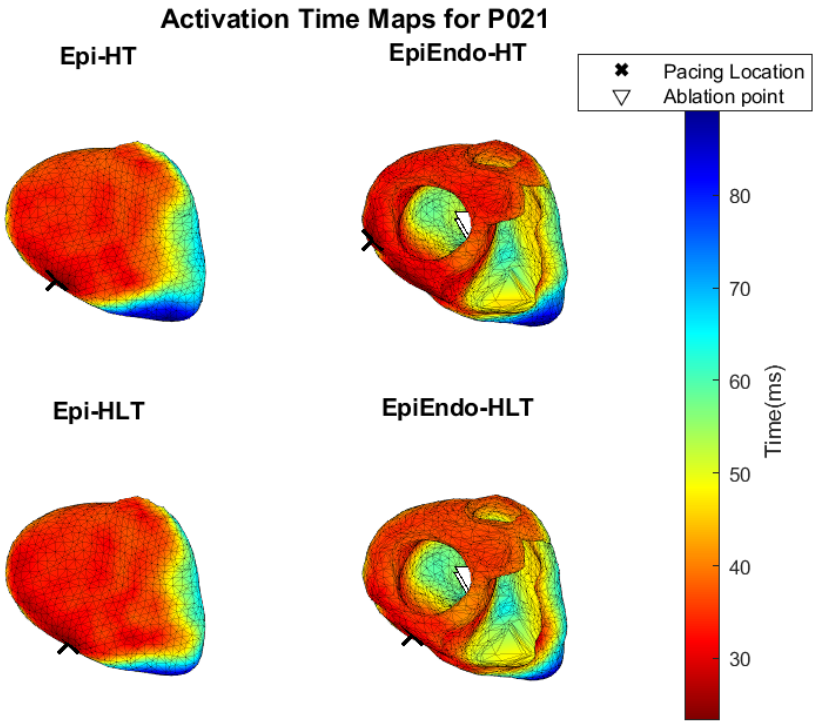


Figure B.23: Spatiotemporal AT maps of P021 with pacing locations

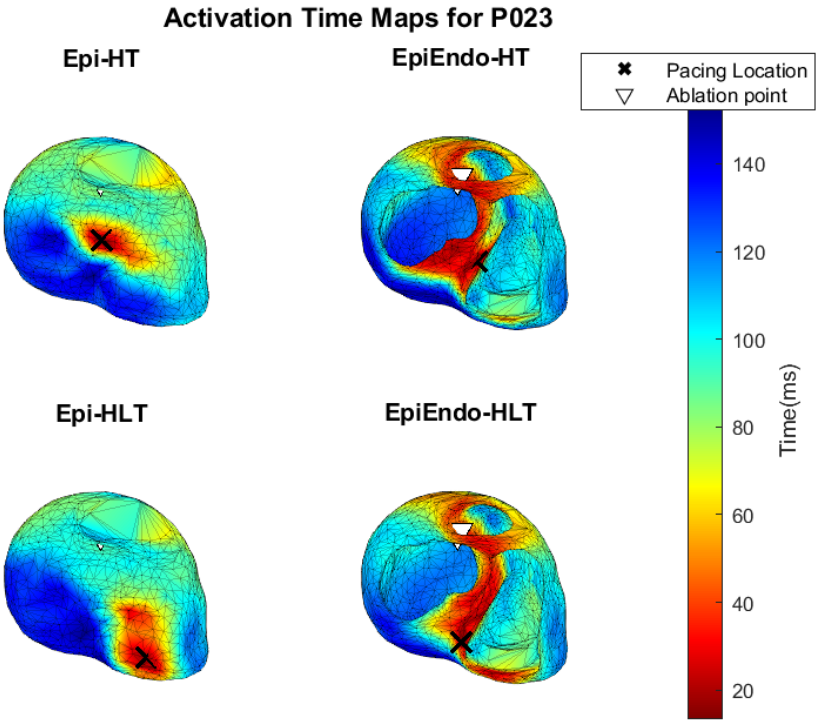


Figure B.24: Spatiotemporal AT maps of P023 with pacing locations

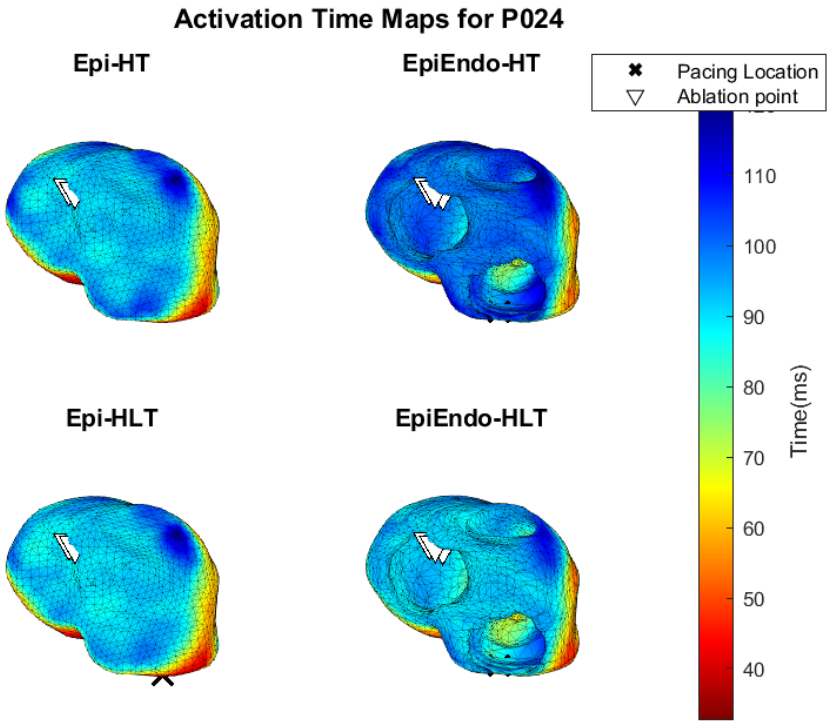


Figure B.25: Spatiotemporal AT maps of P024 with pacing locations

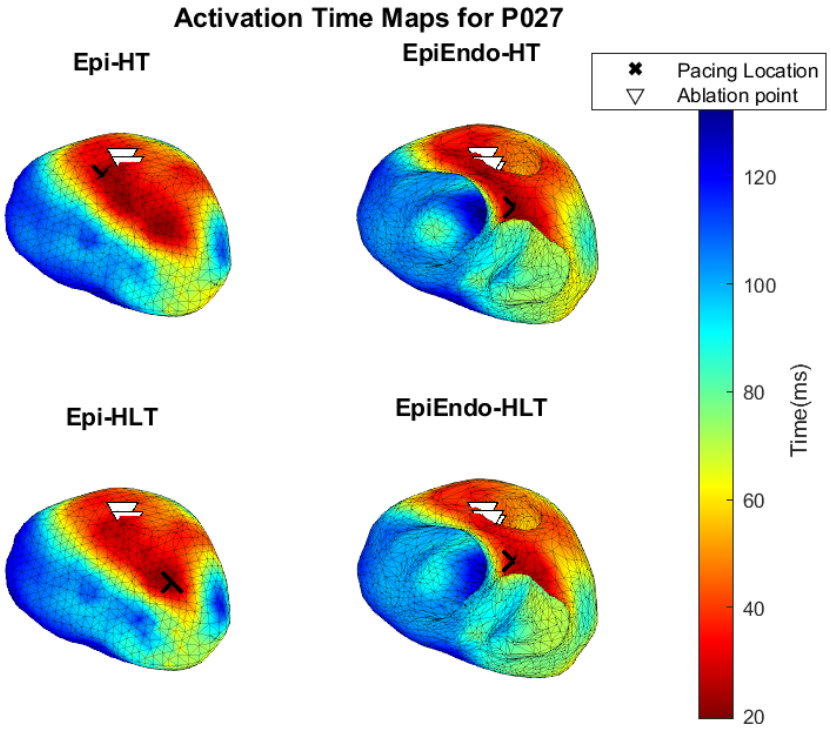


Figure B.26: Spatiotemporal AT maps of P027 with pacing locations

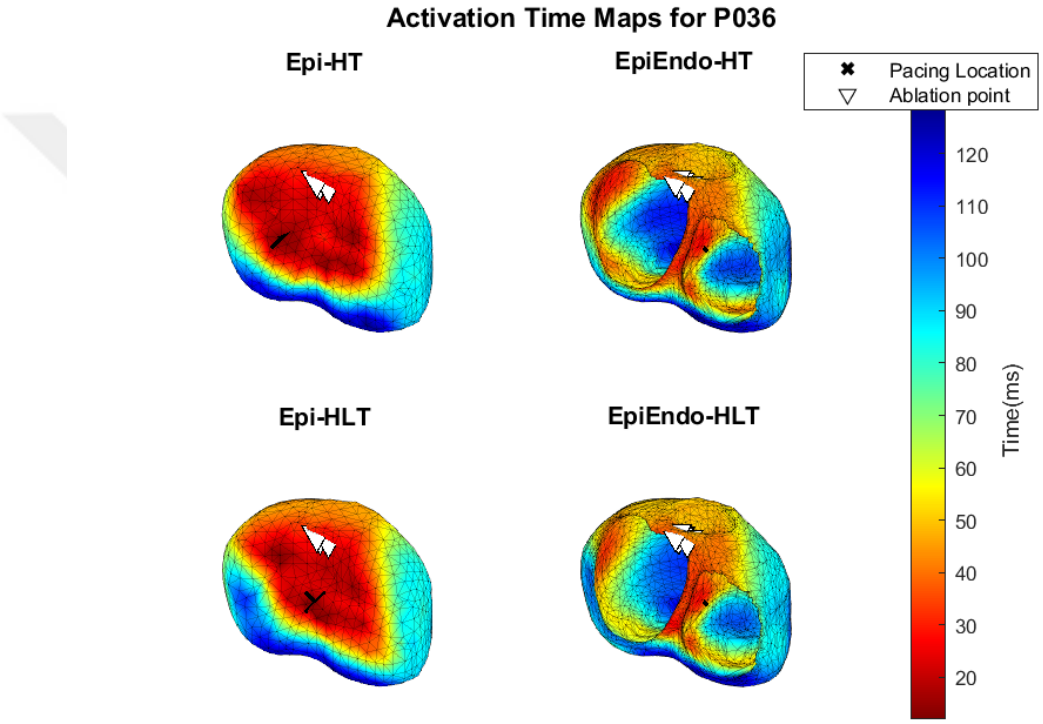


Figure B.27: Spatiotemporal AT maps of P036 with pacing locations

## B.4 Spatiotemporal AT Maps of HBLT Model

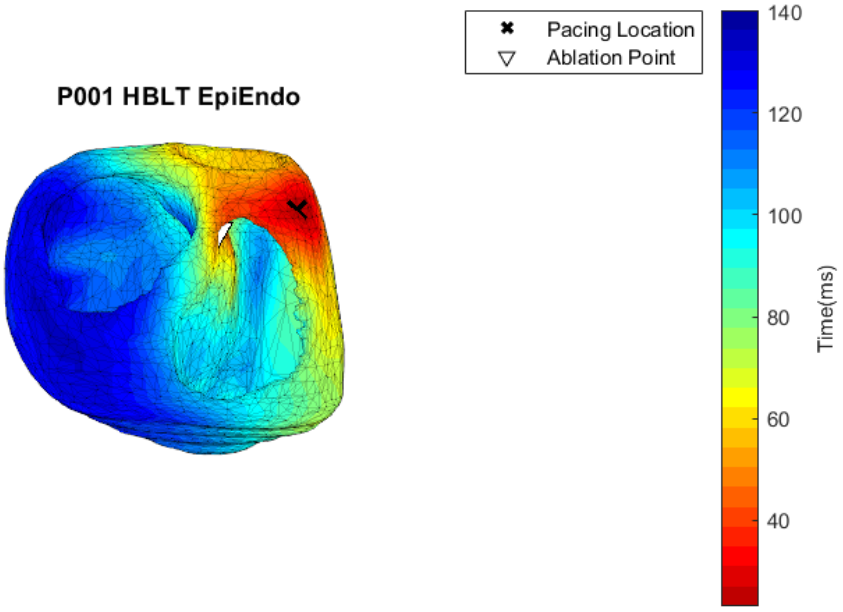


Figure B.28: Spatiotemporal AT maps of P001 for EpiEndo model with blood cavity inhomogeneity

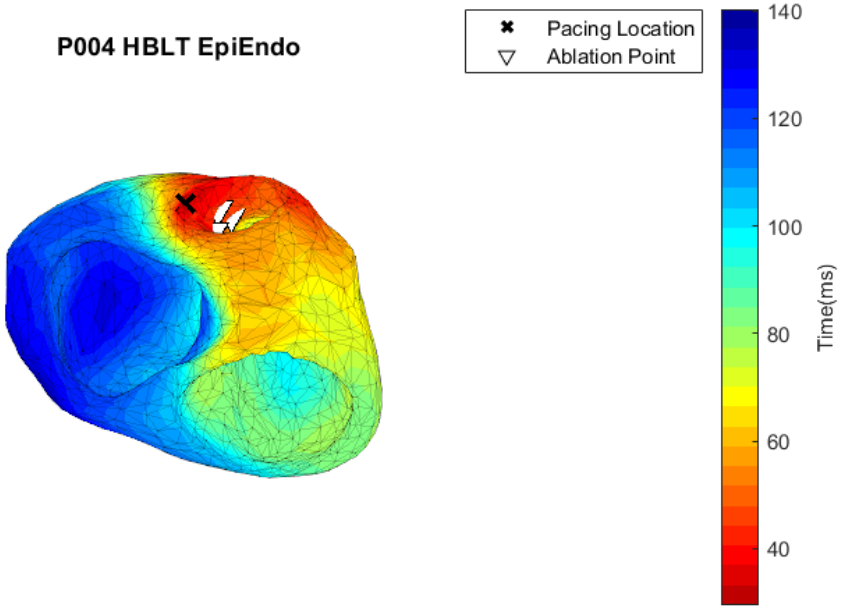


Figure B.29: Spatiotemporal AT maps of P004 for EpiEndo model with blood cavity inhomogeneity

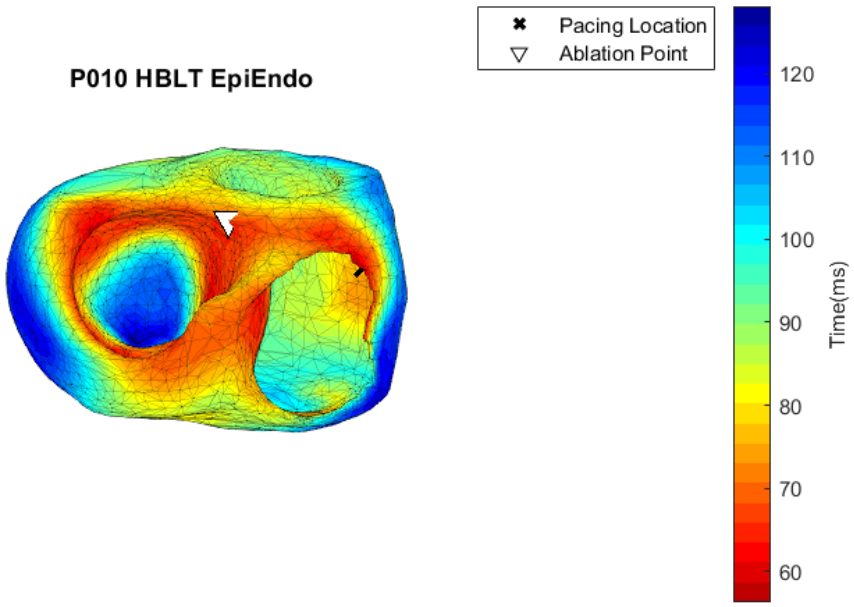


Figure B.30: Spatiotemporal AT maps of P010 for EpiEndo model with blood cavity inhomogeneity

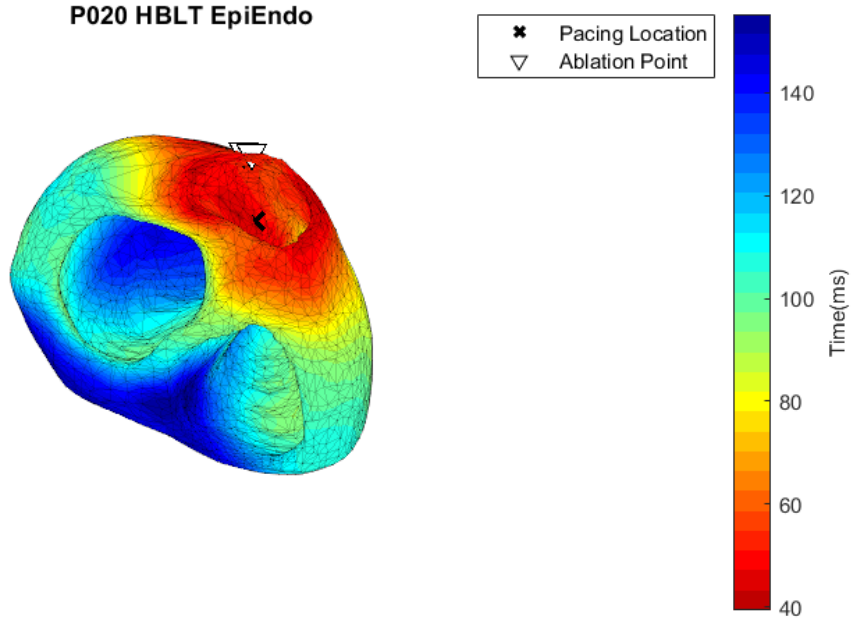


Figure B.31: Spatiotemporal AT maps of P020 for EpiEndo model with blood cavity inhomogeneity

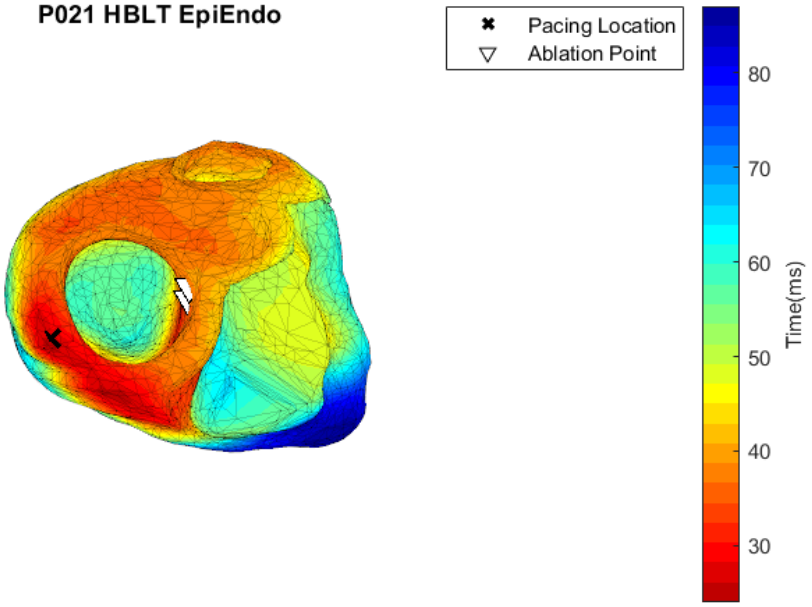


Figure B.32: Spatiotemporal AT maps of P021 for EpiEndo model with blood cavity inhomogeneity

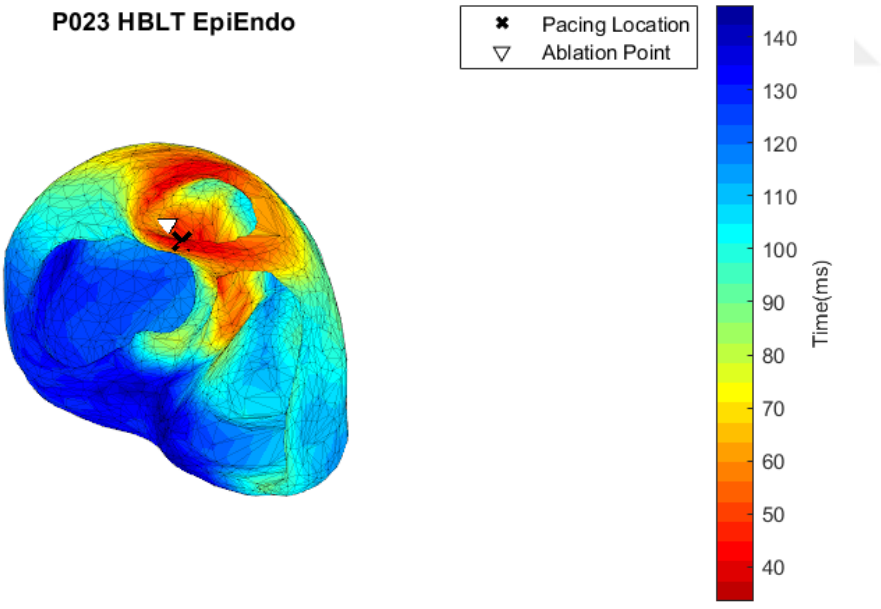


Figure B.33: Spatiotemporal AT maps of P023 for EpiEndo model with blood cavity inhomogeneity

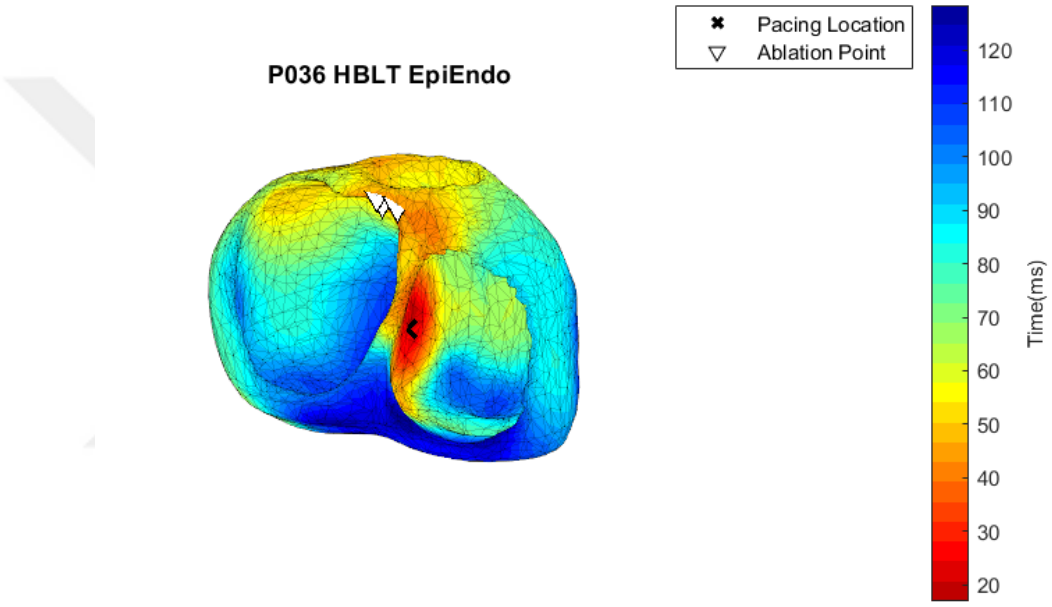


Figure B.34: Spatiotemporal AT maps of P036 for EpiEndo model with blood cavity inhomogeneity

## B.5 PVC Locations

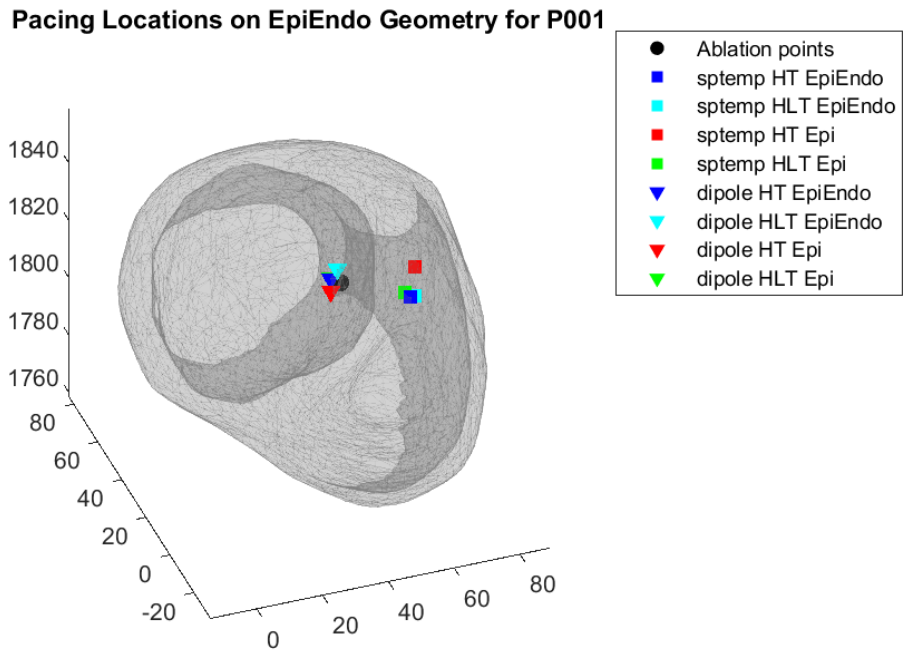


Figure B.35: PVC origin estimates by spatiotemporal method and dipole based method for P001 with the ablation points

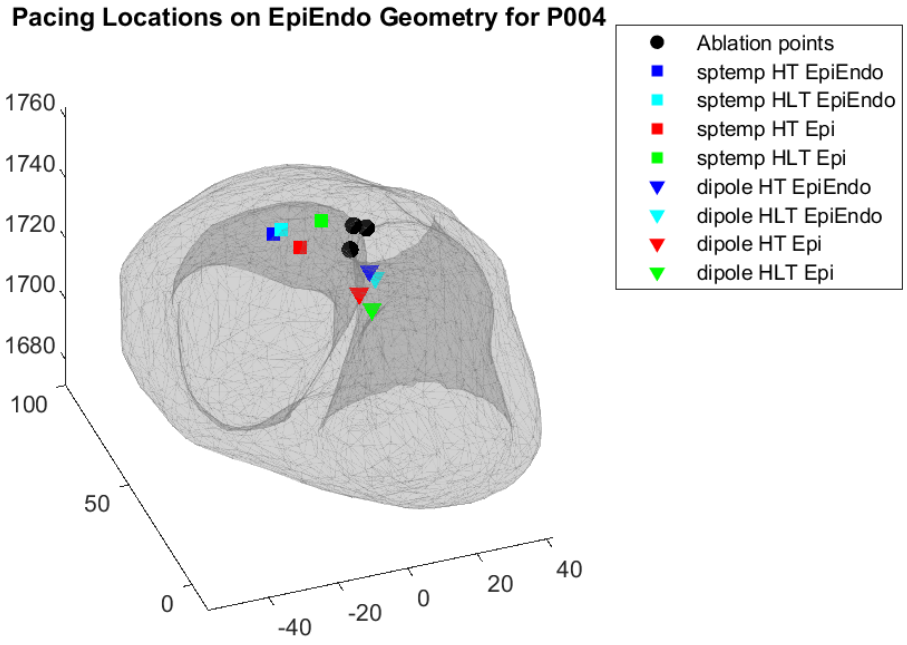


Figure B.36: PVC origin estimates by spatiotemporal method and dipole based method for P004 with the ablation points

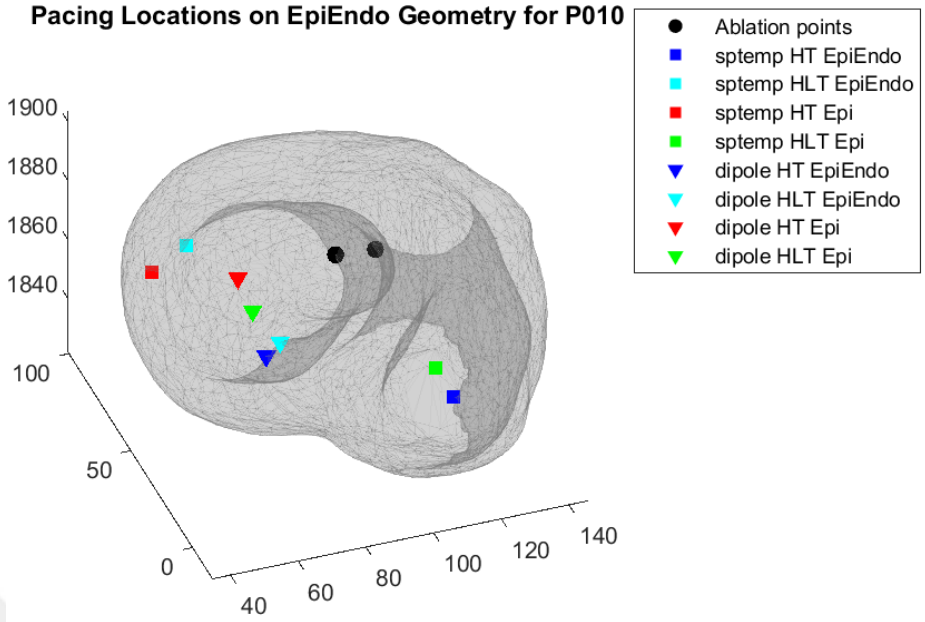


Figure B.37: PVC origin estimates by spatiotemporal method and dipole based method for P010 with the ablation points

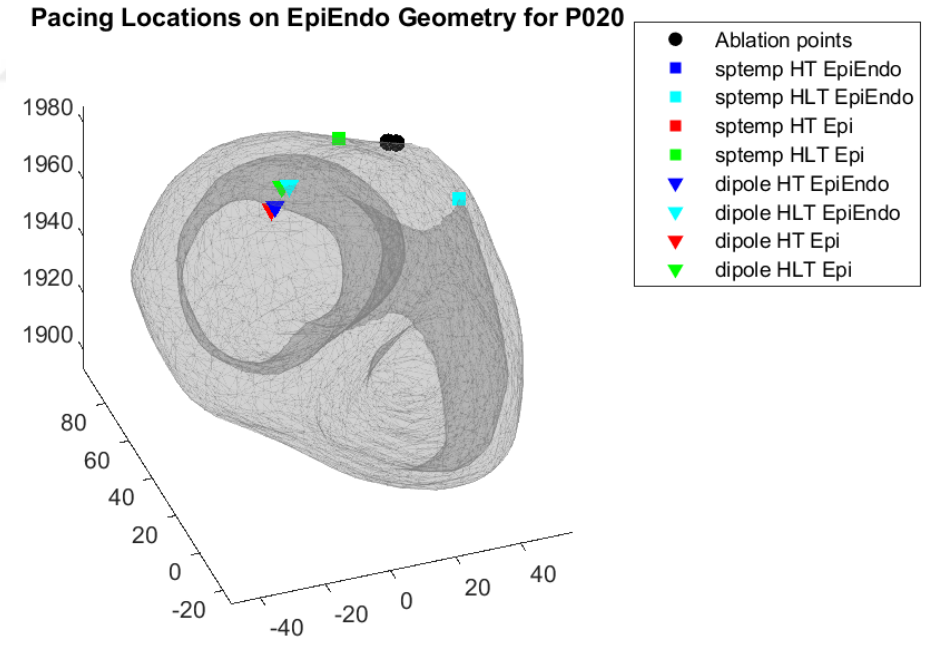


Figure B.38: PVC origin estimates by spatiotemporal method and dipole based method for P020 with the ablation points

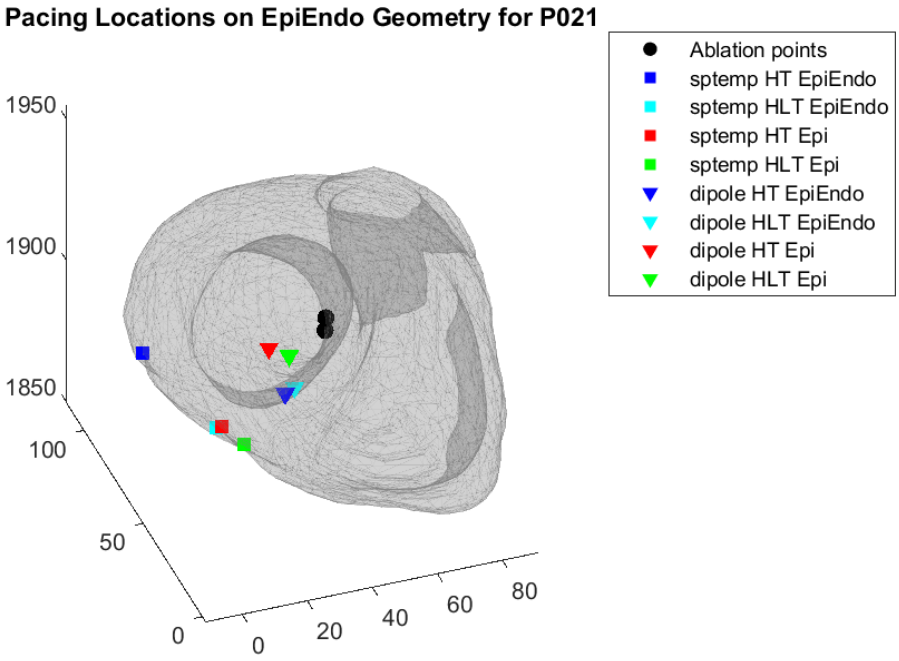


Figure B.39: PVC origin estimates by spatiotemporal method and dipole based method for P021 with the ablation points

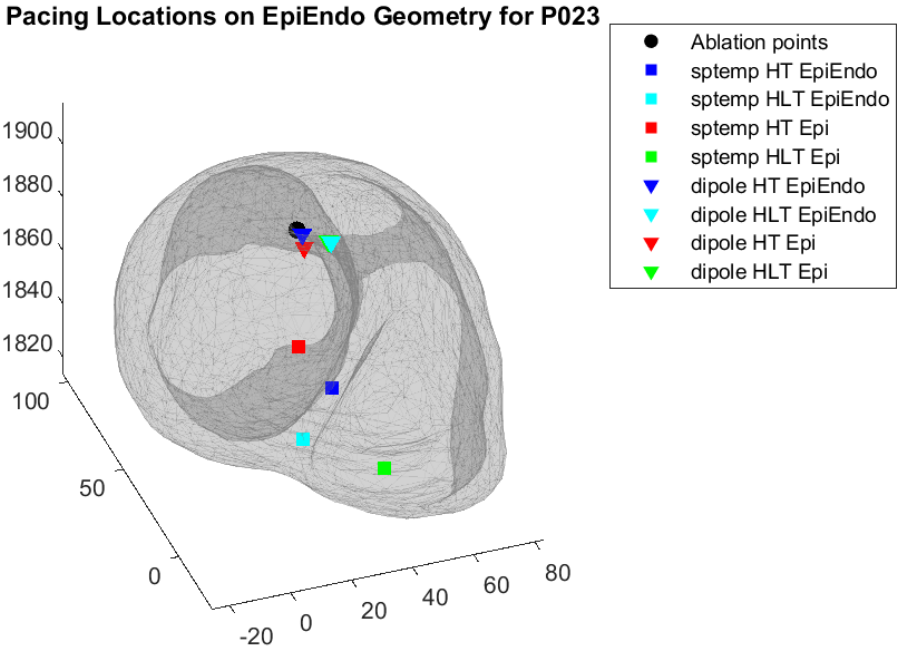


Figure B.40: PVC origin estimates by spatiotemporal method and dipole based method for P023 with the ablation points

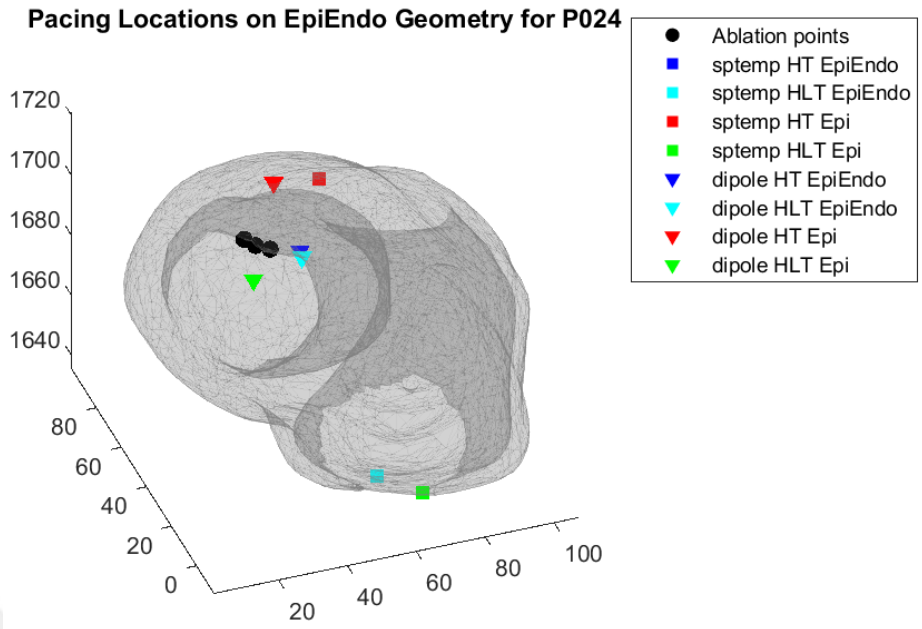


Figure B.41: PVC origin estimates by spatiotemporal method and dipole based method for P024 with the ablation points

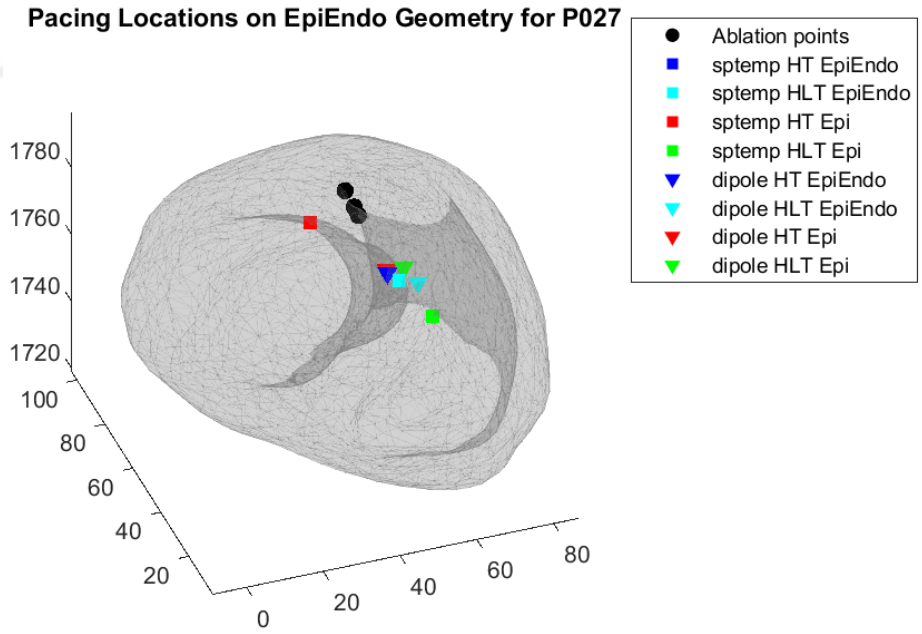


Figure B.42: PVC origin estimates by spatiotemporal method and dipole based method for P027 with the ablation points

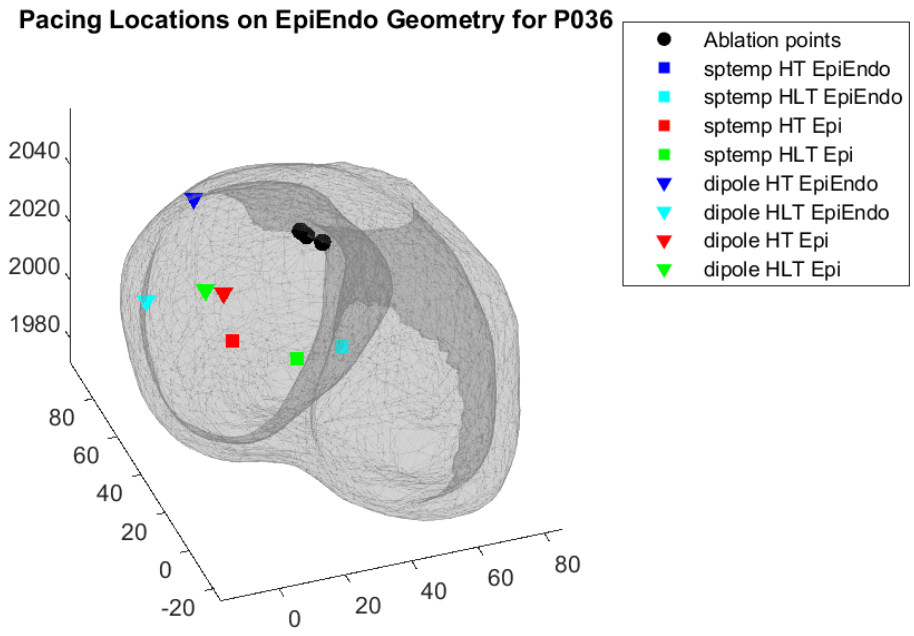


Figure B.43: PVC origin estimates by spatiotemporal method and dipole based method for P036 with the ablation points

# APPENDIX C

# QUANTITATIVE RESULTS

Table C.1: Localization errors(mm) of potential based models with their means and mean LE of dipole based models

| Patient # | Potential-based | | | | | | Dipole-based |
|---|---|---|---|---|---|---|---|
| | HT Epi | HLT Epi | HT EpiEndo | HLT EpiEndo | HBLT EpiEndo | mean | mean |
| P001 | 27.93 | 27.72 | 29.2 | 29.7 | 29.2 | 28.75 | 12.1 |
| P004 | 20.35 | 20.79 | 22.96 | 20.92 | 19.05 | 20.81 | 17.2 |
| P010 | 59.18 | 40.71 | 49.15 | 53.32 | 39.55 | 48.38 | 34.8 |
| P020 | 16.52 | 16.52 | 23.3 | 25.59 | 23.36 | 21.06 | 40.1 |
| P021 | 42.07 | 42.03 | 53.67 | 43.66 | 49.76 | 46.23 | 19.6 |
| P023 | 36.23 | 78.47 | 56.54 | 67.64 | 20.52 | 51.88 | 18.6 |
| P024 | 49.67 | 27.1 | 51.93 | 30.01 | - | 39.68 | 17.5 |
| P027 | 11.32 | 26.83 | 8.61 | 41.73 | - | 22.12 | 23.3 |
| P036 | 39.85 | 36.38 | 55.13 | 55.13 | 42.93 | 45.88 | 39.2 |